DYNAMICAL FOOTPRINTS OF AEROSOLS IN EXTRATROPICAL ATMOSPHERIC DISTURBANCES AND CIRCULATION: A MODELING ANALYSIS

A Dissertation
Presented to
The Academic Faculty

By

Yi Lu

In Partial Fulfillment
of the Requirements for the Degree
Doctor of Philosophy in the
School of Earth and Atmospheric Sciences

Georgia Institute of Technology

December 2017

DYNAMICAL FOOTPRINTS OF AEROSOLS IN EXTRATROPICAL ATMOSPHERIC DISTURBANCES AND CIRCULATION: A MODELING ANALYSIS

Approved by:

Dr. Yi Deng, Advisor
School of Earth and Atmospheric Sciences
Georgia Institute of Technology

Dr. Emanuele Di Lorenzo
School of Earth and Atmospheric Sciences
Georgia Institute of Technology

Dr. Robert X. Black
School of Earth and Atmospheric Sciences
Georgia Institute of Technology

Dr. Jingfeng Wang
School of Civil and Environmental Engineering
Georgia Institute of Technology

Dr. Yuhang Wang
School of Earth and Atmospheric Sciences
Georgia Institute of Technology

Date Approved: August 15, 2017

To my lovely family

ACKNOWLEDGEMENTS

All Ph.D. candidates can testify that dissertations do not occur in a vacuum, and this dissertation is no exception. Without the support and love of many people, this research project would not have been possible. Throughout my tenure at Georgia Tech, Dr. Yi Deng, my advisor, has been a proverbial "beacon of light" for me. Dr. Deng, with his great passion and research genius, allowed me the freedom to explore, yet gently nudging me when I lost focus. Also, thank you Dr. Chun-Chieh Wu, my former advisor in Taiwan, who encouraged me to study abroad. I would also like to thank my committee members, Dr. Robert Black, Dr. Yuhang Wang, Dr. Emanuele Di Lorenzo, and Dr. Jingfeng Wang for their efforts and input into this dissertation. I am grateful for the support of NASA and Taiwanese Ministry of Education, who provided funding, through a scholarship, for my doctoral studies in the United States. I am also grateful for having such great lab-mates at Georgia Tech. Special recognition and thanks goes to Bradley Hegyi and Jia He for their invaluable advice regarding research, and helping me think about future career prospects.

Finally, I would like to thank all my friends in Atlanta who made my journey through graduate school enjoyable and memorable. Shih-Yu Huang, you are a trusted and reliable friend. You have stood with me through this entire process. Hao-Lin Hu, Yu-Han Chu, Wei-Fang Sun, and I-Ting Chuang, I am grateful that I started my studies at Georgia Tech at the same time as you. Your support made the transition to American life bearable. I would like to thank my family for their unconditional support and love throughout my graduate education. And finally to my beloved wife Amy Huang; where would I be without you? Thank you for encouraging and comforting me for the past four years. This dissertation is our achievement.

TABLE OF CONTENTS

LIST OF TABLES

LIST OF FIGURES

LIST OF ABBREVIATIONS

AOD	Aerosol Optical Depth
CAM5	Community Atmosphere Model version 5
CAMS	Convection–Advection–Moisture Self-adjustment (mechanism)
CCN	Cloud Condensation Nuclei
CCSM	Community Climate System Model
CESM	Community Earth System Model
CRM	Cloud Resolving Model
CS	Clear-Sky (radiative heating)
EOF	Empirical Orthogonal Function
EAPE	Eddy Available Potential Energy
ECPP	Explicit Cloud-Parameterized-Pollutant (approach)
EKE	Eddy Kinetic Energy
ENSO	El Nino–Southern Oscillation
GCM	General Circulation Model
HF	High-Frequency
IN	Ice Nuclei
LF	Low-Frequency
LWP	Liquid Water Path
MMF	Multiscale Modeling Framework
NCEP	National Centers for Environmental Prediction
NCAR	National Center for Atmospheric Research
PCS	Pristine Clear Sky (radiative heating)

PNA	Pacific North America (pattern)
POM	Primary Organic Matter
PD	Present-day (experiment)
PI	Preindustrial (experiment)
PV	Potential Vorticity
QG	Quasi-Geostrophic
RHA	Radiative Heating due to Aerosols
RHC	Radiative Heating due to Clouds
RRTMG	Rapid Radiative Transfer Model for GCMs
SAM	System for Atmospheric Modeling
SOA	Secondary Organic Aerosol
SP-CAM	Superparameterized Community Atmosphere Model
SST	Sea Surface Temperature
TEM	Transformed Eulerian-Mean
WP	West Pacific (pattern)
WRF	Weather Research and Forecasting (model)
ZAPE	Zonal Available Potential Energy
ZKE	Zonal Kinetic Energy

SUMMARY

Atmospheric disturbances of various spatiotemporal scales occupy extratropical regions in winter. These disturbances not only influence day-to-day weather variability but also modulate regional climate through their transports of momentum, heat and moisture, maintaining the winter-mean atmospheric circulation. Among them, the synoptic-scale disturbances, with periods less than 10 days and surface manifestations as cyclones/anticyclones, form extratropical "storm tracks". The region of the North Pacific storm track is also known to be characterized by high concentrations of atmospheric aerosols of both natural and anthropogenic origins, making it an ideal location for investigating the interaction between aerosols and extratropical disturbances. This dissertation uses a regional and a global model to identify the dynamical footprint that atmospheric aerosols leave in the development and overall activity of both synoptic-scale (i.e., high-frequency or HF) and low-frequency (LF) atmospheric disturbances, and to document the collective effects of aerosols on the northern extratropical atmospheric circulation.

The first part of the study investigates the aerosol indirect effects on the development of idealized baroclinic (synoptic-scale) waves in the Weather Research and Forecasting (WRF) model. The cloud droplet number concentration (DNC) in WRF is doubled to mimic the aerosol indirect effects bypassing detailed aerosol activation processes. Statistically significant differences between experiments where the DNC is doubled and the control experiments are identified for an initial transient period before the surface feature of the baroclinic wave (cyclone) enters the stage of rapid intensification. Doubling of the DNC increases total cloud water in the model, lowers the cloud level, and

enhances latent heating to the east of the surface low, which strengthens the mid-tropospheric ridge. Subsequent changes in dry dynamical processes (e.g., advection of potential vorticity) as a result of the ridge strengthening lead to the deepening of the trough and ultimately produce a mild yet statistically significant strengthening of the baroclinic wave as a result of the DNC doubling. The results demonstrate the fundamental differences between aerosol effects on extratropical disturbances and those on tropical disturbances (e.g., tropical cyclones), where the role of dry dynamical processes in the latter is much less important compared to those in the former.

The second part of the study examines the impacts of aerosols on the development of realistic synoptic-scale disturbances in the Superparameterized Community Atmosphere Model (SP-CAM). The SP-CAM explicitly resolves the cloud-scale processes with a subgrid cloud resolving model (CRM) embedded in a general circulation model (GCM). It allows explicit representations of subgrid variability of cloud dynamics and microphysics and the full interaction between aerosols and deep convection, which is missing in the previous WRF modeling experiments. By examining the results from 13 ensemble pairs of 1X-EXP (control run) and 5X-EXP (increasing aerosol concentrations by 5 times), it suggests that the growth rate of a realistic cyclone sampled from the control run is temporarily reduced. A *convection–advection–moisture self-adjustment (CAMS)* mechanism of aerosol–cyclone interaction is proposed to explain this finding. Specifically, the weakened growth is unambiguously attributed to the weakening of the cold advection underneath the mid-tropospheric trough of the cyclone. The weakened cold advection is in turn driven by a decrease of the zonal temperature gradient that is tied to the reduced latent heating in the stratiform cloud region of the cyclone. Invigoration of convection ahead of

the cold front by aerosols is found to be directly responsible for a suppressed moisture supply into the stratiform cloud region and thus the reduced latent heating there. The discrepancy between the results in the first part (WRF model) and the second part (SP-CAM) highlights the importance of the coupling between aerosols and deep convection in the development of synoptic-scale disturbances.

The last part of the study explores the collective effects of aerosols on multiple aspects of the northern extratropical circulation utilizing long-term perpetual winter simulations conducted with the SP-CAM. The first focus is the change in the activities of both HF and LF eddies (disturbances) in response to aerosol change from the pre-industrial condition to the present-day condition. In general, the total energy of the HF eddies in the North Pacific and North Atlantic storm track regions increases while the total energy of LF eddies decreases as a result of increased aerosol emission. Analyses of the eddy local energetics suggest that changes in baroclinic (BC) energy conversion and diabatic processes are closely related to the enhanced HF eddy activity. Specifically, aerosol-induced solar heating change modulates the lower-level baroclinicity over East Asia, suggesting the potential linkage to the BC energy conversion in its downstream storm track. In contrast, the enhanced HF eddy activity over the North Atlantic is attributed to a stronger "downstream development" as result of the increased barotropic (BT) energy conversion over the North America that is partly linked to the intensified HF eddies exiting the Pacific storm track. Over the North Pacific, the increased HF BC conversion is accompanied with suppressed BC conversion for LF eddies. In association with reduced LF eddy activity over the Gulf of Alaska, the reduction of blocking events in this region leaves detectable changes in winter temperature along the west coast of the US. Results of the eddy E-vector analysis

suggest that both HF and LF eddies provide feedbacks to the winter-mean flow, supporting the changes in the latter. Also discussed are the implications of these findings for the short-term prediction of weather and long-term projection of climate change in the northern extratropics.

CHAPTER 1

INTRODUCTION

1.1 Extratropical Disturbances

1.1.1 High-Frequency Extratropical Disturbances and Storm Tracks

The variation of atmosphere is constituted of fluctuations across different temporal and spatial scales, driven by restoring forces on air parcels displaced from the equilibrium states (Holton 2014). The temporal and spatial scales of a system are usually constrained by one another (i.e., high-frequency variations usually accompany with smaller spatial scale, and vice versa). The fluctuations can be as small as acoustic waves occurring in seconds and few meters, or can be as large as decadal oscillations across the entire hemisphere. Due to the direct influence on day-to-day weather variations and human activities, the high-frequency (HF) synoptic-scale, typically referring to the timescale less than 10 days and spatial-scale about thousands of kilometers, atmospheric disturbances have drawn the attention of meteorologists for centuries. Especially in the wintertime, the region in the midlatitude is characterized by intense activity of these HF disturbances, also known as "storm tracks" (Blackmon 1976; Blackmon et al. 1977). Storm tracks were first characterized in the mid-nineteenth century (Hinman 1888). Studies have shown that these disturbances not only drive day-to-day weather variability, but also influence large-scale circulation and regional climate through the transports of momentum, heat, and moisture (Peixoto and Oort 1992; Trenberth and Stepaniak 2003; Schneider et al. 2006).

Because the storm tracks are constituted by intense HF synoptic-scale transient activities, studies have shown that it can be identified by transient quantities (e.g., bandpass standard deviation or covariance) in many different atmospheric variables (Blackmon et al. 1977; Lau 1978, 1979). For example, Figure 1.1 shows the bandpass statistics from the National Centers for Environmental Prediction National Center for Atmospheric Research (NCEP-NCAR) reanalysis in geopotential height, meridional wind, sea level pressure, poleward fluxes of heat and momentum. In general, the two most significant peaks over the two ocean basins can always be found, referring to as the Pacific storm track and Atlantic storm track. The Pacific storm track extends from East Asia across North Pacific, and shading into the western coast of North America. The Atlantic storm track shares a similar geographical distribution with the entrance region over the eastern slopes of

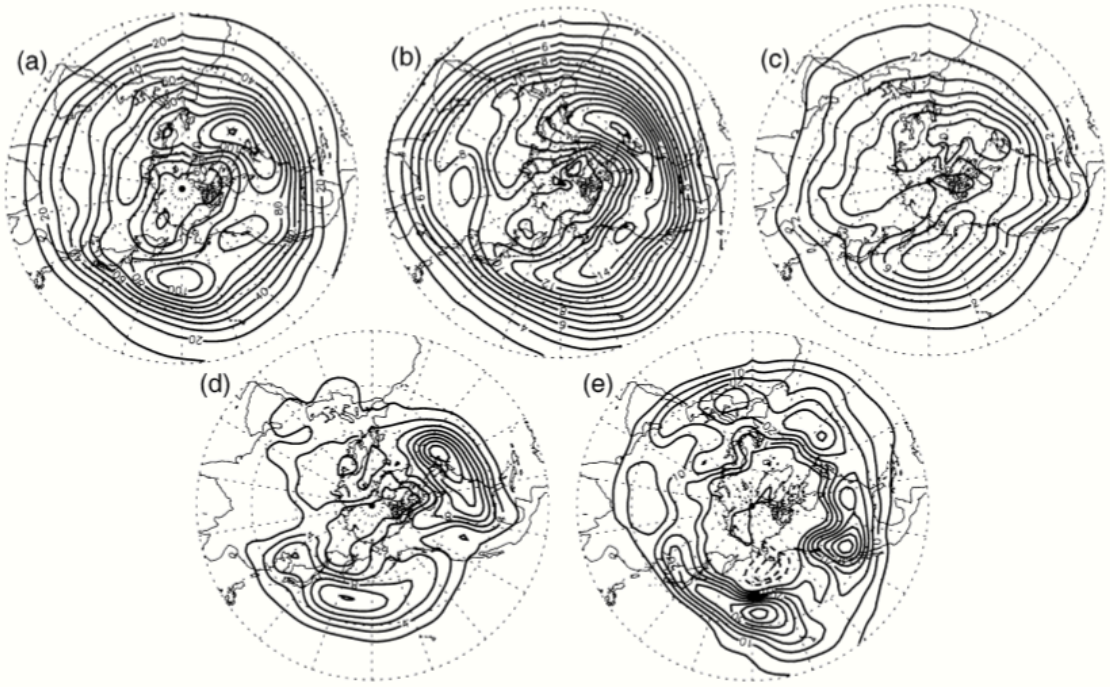

Figure 1.1 Bandpass statistics from the NCEP-NCAR reanalysis. Standard deviations of (a) 250 hPa Height, (b) 300 hPa meridional wind, (c) sea level pressure and poleward fluxes of (d) 850 hPa heat and (e) 250 hPa westerly momentum. Reproduced from Chang et al. 2002.

Rockies and the exit region in the northern Europe. The similarity of the two major storm tracks imply that the dominant driving force for the HF eddies comes from the baroclinic energy conversion, which is known as to extract the energy of the background baroclinicity established by the large-scale horizontal temperature gradient (Lindzen and Farrell 1980).

However, the relationship between the intensity of background baroclinicity and storm track activity is not so straightforward, leading to some distinct features between these two storm tracks. For instance, in the subseasonal timescale, the local background baroclinicity in both North Pacific and North Atlantic basins reaches the maximum in the midwinter (January to February). Nakamura (1992) points out that the activity of Pacific storm track exhibits a minimum while that of Atlantic shows a maximum in the midwinter. The mechanisms to cause this so-called midwinter suppression and the seasonal cycle of the Pacific storm track have been widely discussed in many studies. The key factors can be summarized as follows: downstream development (Chang and Orlanski 1993), upstream seeding (Robinson and Black 2006; Penny et al. 2010, 2011), diabatic heating (Chang 2001; Chang and Song 2006; Chang and Zurita-Gotor 2007), barotropic wind shear (Deng and Mak 2005), jet width (Harnik and Chang, 2004) and trapping by the mean flow (Nakamura 1992; Nakamura and Sampe, 2002). There is no single factor dominating the mechanism of midwinter suppression, implying the complexity of storm track dynamics that cannot be fully explained by only the normal mode baroclinic instability theory.

1.1.2 Low-Frequency Extratropical Disturbances

On the timescale around 10 to 30 days, the extratropical region is characterized by high-pressure, anticyclonic disturbances with retrograding (westward, against the mean

westerlies) movement, known as “blocking” (Dole and Gordon 1983; Trenberth 1986; Dole and Black 1990; Black 1997). The low-frequency (LF) disturbances interact with synoptic-scale disturbances, as well as back ground flow, driving atmospheric LF variabilities. Early studies show that a split of westerlies around a blocking system deflects the storm track (Berggren et al. 1949; Rex 1950a, 1950b; Petterssen 1956). In the manner of two-way interaction, Green (1977) suggests that the HF eddy forcing may reinforce the LF disturbances, which has been widely supported in many observational analysis (Mahlman 1979; Illari and Marshall 1983; Illari 1984; Mullen 1986, 1987). The mechanisms of scale-interaction have also examined in numerical experiments within a barotropic framework (Shutts 1983; Haines and Marshall 1987; Metz 1986) and a baroclinic framework (MacVean 1985; Vautard et al 1988; Vautard and Legras 1988). In particular, by analyzing an observation of eighteen winter seasons, Lau and Nath (1991) show that the positive contribution from HF eddy vorticity flux overcomes the damping effect from HF eddy heat flux, leading to a net positive geopotential height tendency to reinforce the LF height anomaly. An independent study by Dole (1986) reaches a similar conclusion. Lau (1988) points out some relations between storm track anomalies and teleconnection patterns (Wallace and Gutzler 1981), including the meridional displacement of storm track associated with Pacific/North American (PNA) pattern and the fluctuations in the intensity linked to the West Pacific (WP) pattern. Other studies also note a similar symbiotic link between storm track anomalies and planetary-scale flow anomalies (Cai and Mak 1990; Robinson 1991).

1.1.1 Dynamics of High-Frequency Extratropical Disturbances

The baroclinic instability theory, which uses linear analysis and was pioneered by Charney (1947) and Eady (1949), serves to depict the midlatitude cyclogenesis from an infinitesimal perturbation by a single normal mode with the largest instability (most unstable mode), thus releasing the background available potential energy by poleward and upward motion of warm air, as well as equatorward and downward motion of cold air (Browning and Roberts 1994). However, the growth rate of cyclogenesis in the observation can sometimes exceed the theoretical expectation. Farrell (1982, 1984) demonstrates the importance of nonlinear effect that transient nonmodal growth can dominate a single normal mode, particularly in a short period of time in the early developing stage. A nonmodal disturbance, as defined by Ferrell (1984), refers to any disturbance that comprises more than one single mode, and the nonmodal growth is the amplification due to the composition of two or more neutral (or even decaying) modes (Hakim 2000). It implies that cyclogenesis (baroclinic energy conversion) does not necessarily require the existence of baroclinic instability; rather the stochastic dynamics of stable baroclinic system may be sufficient (Farrell and Ioannou 1995; Whitaker and Sardeshmukh 1998).

It is interesting to note the mechanisms that sustaining such strong background baroclinicity (mostly the meridional temperature gradient) and further localizing the storm tracks in the midlatitude during the wintertime besides the solar forcing since: (1) the solar energy cannot explain the zonal asymmetry of storm track and (2) the transient eddies tend to repeatedly mix the air destroying the horizontal gradient of temperature. Hoskins and Valdes (1990) used a linear stationary model to demonstrate that the storm track can be partially self-sustained by eddy driven diabatic heating, including the latent heat over the

entrance region and the sensible heat flux from the warm western boundary current. Some studies show that, even without diabatic heating in the entrance region, the orographically induced planetary waves can still maintain the structure of storm track (Broccoli and Manabe 1992; Lee and Mak 1996). Although much debate exists on whether the diabatic heating or orography is the primary factor, these studies imply the strong modulation of storm track by the stationary waves.

In the linear baroclinic instability theory, a fixed normal mode extracts energy from background potential available energy (baroclinic energy conversion) and dissipates energy to the mean flow kinetic energy (barotropic energy conversion). However, the baroclinic wavetrains (Lee and Held 1993) discovered in the observation indicate the barotropic conversion in one eddy's dissipation stage transfers its energy to eddies that are downstream (Orlanski and Katzfey 1991; Chang 1993; Orlanski and Chang 1993). The phenomenon is known as the downstream development (Namias and Clapp 1944; Cressman 1948; Yeh 1949; Simmons and Hoskins 1979). Downstream development can extend the storm track into regions without strong baroclinicity. Swanson et al. (1997) shows that, in a barotropic framework, the nonlinearity of Rossby wave propagation will lead to an irreversible loss of wave energy if the local minimum of background zonal wind is sufficiently weak. Studies also show that the barotropic shear can limit the baroclinic growth (known as barotropic governor, James 1987) and determine the maximum of the storm track (Whitaker and Dole 1995). When taking both the nonlinearity and barotropic effects into consideration, one can have a more comprehensive explanation of the geographical distribution and variation of the storm track.

Besides the baroclinic and barotropic effects, diabatic heating also contributes to the storm track dynamics in a few different ways. Black (1998) uses a diagnostic study showing that, due to the zonally asymmetric distribution of condensational heating, the eddy available potential energy (EAPE) is increased in the exit region of storm track, thus enhancing the eddy activities. While many theoretical (Mak 1982; Emmanual et al. 1987; Fantini 1995) and numerical (Gutowski et al. 1992; Davis et al. 1993; Reed et al. 1992) studies indicate the similar results, some studies argue other opposing mechanisms which leads to the weakening of eddy activity by condensational heating. The opposing mechanisms include the reduction of meridional temperature gradient (Manabe et al. 1965) and the increasing efficiency of eddy energy transportation (Held 1993) due to the incorporation of moisture processes. The surface sensible heat flux has the maximum effect over the upstream (west part of) oceans where the cold continental air meets the warm ocean water. In general, the ocean acts as an energy sink by discharging the air temperature contract (Branscome et al. 1989; Swanson and Pierrehumbert 1997; Hall and Sardeshmukh 1998). However, in certain circumstances the surface sensible heat flux can also induce strongly unstable, shallow short waves (Mak 1998). Although the diabatic heating usually contributes a relatively small amount to the energy cycle of baroclinic waves, the contribution can, in some situations, locally reach the same order as the conversion from the mean flow (Black 1998).

1.1.3 Dynamics of Low-Frequency Extratropical Disturbances

More complexity comes from the interaction among the HF and LF disturbances as well as the surroundings in longer timescales. Lau (1988) used the empirical orthogonal

function (EOF) analysis to demonstrate a correlation between the monthly mean flow and the storm track's intensity and meridional shift. The idea was further extended by follow-up studies that demonstrate the linkage between the storm track anomalies and low-frequency disturbances, including the change of Pacific blocking and Atlantic jet stream (Metz 1989) and the planetary-scale waves (Cai and Mak 1990). In the tropics, the anomaly of sea surface temperature on the interannual timescale, usually referred as the El Nino–Southern Oscillation (ENSO), also has a strong modulation on the Pacific storm track (Trenberth and Hurrell 1994; Straus and Shukla 1997; Zhang and Held 1999). The shift of the Pacific storm track equatorward and downstream during El Nino years appears to be a response to the change of Hadley circulation (Bjerknes 1966, 1969), but the direct response on the extratropical stationary waves to ENSO is actually weak (Held et al. 1989). Previous studies show the important role of the forcing by transient eddies to be the bridge that connects the tropical heating anomalies and extratropical stationary waves (Branstator 1995; Yang and Hoskins 1996). Research has consistently shown the existence of the interdecadal modulations on the Pacific storm track (Nakamura and Izumi 1999) and the Atlantic storm track (Ebisuzaki and Chelliah 1998), as well as the intensity and frequency of transient eddies (Geng and Sugi 2001; Graham and Diaz 2001). Even by removing the influence from ENSO-like forcing (Zhang et al. 1997) and Artic Oscillation (AO, Thompson and Wallace 1998, 2000; Thompson et al. 2000), the residual part of the storm track activity still demonstrates a significant variability on the interdecadal timescale (Chang and Fu 2002). The mechanisms behind the cross-frequency interactions remain unsolved.

1.1.4 Local Energetics of Extratropical Disturbances

A pioneering study by Lorenz (1955) reveals the midlatitude dynamics in the energetics perspective, by separating the circulation into the zonal mean and the departures. Circulation is characterized by the energy conversion from zonal available potential energy (ZAPE) to eddy available potential energy (EAPE), to eddy kinetic energy (EKE) and then to zonal kinetic energy (ZKE). In general, the magnitude of available potential energy is ten times larger than kinetic energy, but less than one percent of the total potential energy. The total eddy energy budget can be written into five terms (Orlanski and Katzfey 1991): the total energy flux, baroclinic energy conversion, barotropic energy conversion, mechanical dissipation and diabatic contribution. The climatological distributions of each term are summarized in a review paper by Chang et al. (2002). The total energy flux term includes advective energy flux and ageostrophic geopotential flux, indicating the eddy energy propagation and redistribution. The baroclinic conversion locates upstream of peak eddy energy and maximizes in the entrance region of storm track. The barotropic conversion has positive contribution in the entrance region but negative in the exit region. The mechanical dissipation has negative effects and maximizes over the continents. The diabatic contribution is the additional energy source that can increase about 20% to the baroclinic conversion by the condensation.

By pointing out these inseparable eddy effects in the flux terms of mean flow, Plumb (1983) criticizes the applicability of the traditional energy diagnoses in spite of the mathematical correctness. Plumb proposes using the transformed Eulerian-mean (TEM) approach as a way to eliminate the eddy forcing from the residual mean flow. Despite its potential misleading interpretation, the local energetics analysis is widely used in studies,

because the local energetics have the advantage of free from the quasi-geostrophic (QG) framework and avoidable misleading with care (Chang 2002). For instance, by using energetics analysis tools, numerous studies examine the life cycle of baroclinic waves (Smith 1969; Kung 1977), eddy energy propagation (Chang and Orlanski 1993), modal and nonmodal instability (Mak and Cai 1989), Southern Hemisphere cyclone activities (Orlanski and Katzfey 1991) and interaction between tropical Intraseasonal Oscillation and Pacific storm track (Hsu et al. 2010). To examine the cross-frequency eddy-eddy and eddy-mean flow interactions, the energetics analysis is further extended to different spectrums in the spatial domain (Saltsman 1957; Hayashi 1980; Sheng and Hayashi1990a, b; Sheng and Derome 1991) and in the temporal domain (Jiang et al. 2013; Zhou and Deng 2013).

1.2 **Atmospheric Aerosols**

Atmospheric aerosols alter the radiative processes by directly absorption and scattering, and modify the cloud properties by acting as cloud condensation nuclei (CCN) or ice nuclei (IN). Therefore, the aerosols can modulate the atmospheric energy budget and hydrological cycle. Numerical and observational studies to investigate the aerosol effects are complicated due to the fact that radiative, microphysical, thermodynamical and dynamic processes interact across a tremendous range of spatial scales from an aerosol particle ($<10^{-7}$ m) to a cloud system ($\sim10^{5}$ m). As a result, the aerosol forcing is probably the greatest uncertainty of all the uncertainties regarding global climate forcing with openly debated.

1.2.1 Aerosol-Cloud Interaction

Figure 1.2 summarizes the various mechanisms proposed to explain the aerosol effects on radiation, clouds and precipitation in the warm-rain processes. Aerosol direct effects refer to the direct impacts on radiative transfer by aerosol particles through absorption and scattering, varying by the aerosol species with different radiative properties. By interacting with clouds, an increase in aerosol concentration with the same liquid water content will generally increase the concentration of droplets, leading to smaller droplet sizes and an increase of the cloud albedo, known as the first indirect effect (Twomey 1977). The smaller droplet size and narrower size distribution delays warm-rain processes by inhibiting collision and coalescence processes. Therefore, the clouds' lifetime is extended (Albrecht 1989) which cause a suppression of rainfall (Rosenfeld 1999). Consequently, liquid water is retained in the cloud. The accumulated liquid water then ascends to the higher altitudes reaching above the freezing level. As a result, more latent heating is released to invigorate deep convection (Andreae et al. 2004; Rosenfeld et al. 2008), and

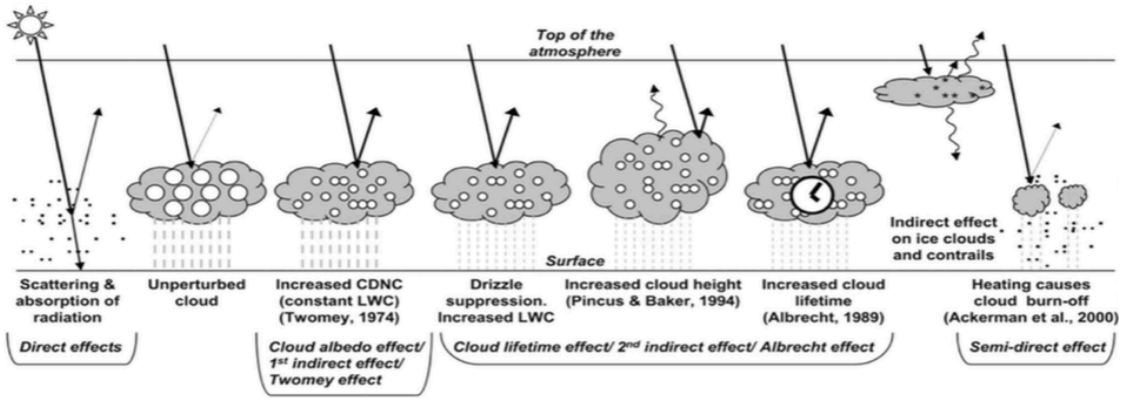

Figure 1.2 Schematic diagram showing the various radiative mechanisms associated with cloud effects that have been identified as significant in relation to aerosols. Reproduced from IPCC AR4 (2007).

ultimately raise the cloud top and sometimes increase the liquid water path (LWP). These aerosol effects on precipitation and cloud properties generally refer to the second indirect effects (Albrecht 1989) that are much more complex than the first indirect effects. Some atmospheric aerosols (e.g., dust) have been linked to exacerbating drought conditions (Huang et al. 2006a, b, 2010) via a semi-direct effect. These atmospheric aerosols, during the semi-direct effect, absorb solar radiation and raise the air temperature (Ackerman et al. 2000) that burn out cloud droplets.

In the mixed-phase clouds, the aerosol effects become more complicated because the atmospheric aerosols can also act as IN to alter cloud properties, especially for mineral dust, soot, biological, organic and ammonium sulfate particles. Without the existence of IN, the homogeneous freezing has to overcome a strict energy barrier, which usually occurs at about -38 ℃ (Pruppacher and Klett 1997). However, the observation shows half of the clouds at temperature as high as about -15 to -20 ℃ (compared to -38 ℃ for homogeneous freezing) can contain ice (Korolev et al., 2003; Field et al., 2004; Kanitz et al., 2011), indicating the important role of the heterogeneous freezing processes. Research shows that there are four major heterogeneous processes dominating ice nucleation: (1) the deposition mode in which water vapor directly deposits onto IN as ice, (2) the condensation-freezing mode in which similar to the deposition mode but deposits onto IN as liquid and then freezes, (3) the immersion mode in which an IN enters a cloud drop and keep unfrozen for some time, later initiating freezing when the temperature drops enough, and (4) the contact mode in which an IN collides a super-cooled drop and freezes immediately (Durant and Shaw 2005; Kulkarni et al. 2012; Murray et al. 2012). Further research indicates that the existence of dust can modulate the occurrences and ice water

path of the super-cooled stratiform clouds (Zhang et al. 2012), thus enhancing deep convections ultimately leading to an increase of anvil cloud coverage and precipitation (Ekman et al. 2007), as well as a change in the intensity of tropical cyclones (H. Zhang et al. 2007, 2009). However, due to the limited knowledge in the ice formation, the ice nucleation parameterizations still have great uncertainties (DeMott et al. 2010), causing the simulation results to vary in diverse degrees across different parameterization schemes (van den Heever et al. 2006; Connolly et al. 2006; Fan et al. 2010).

1.2.2 Impacts on Radiation

Direct aerosol effects are the absorption and scattering of solar radiation (shortwave). Previous studies show that direct effects can change environmental stability and modulate the cloud formation, convection intensity, and even general circulations (Lau et al. 2006; Bollasina et al. 2011; Nabat et al. 2015). In particular, while scattering usually cools the surface, the present of strong absorbing particles (e.g., black carbon) will heat the atmosphere depending on the vertical and horizontal distributions, altering the atmospheric stability and leading to the complicated nonlinear responses (Yang et al. 2013a, b; Fan et al. 2015; Yang et al. 2016).

Atmospheric aerosols can also alter the radiative budget indirectly through the impacts on clouds because clouds serve as atmospheric radiation modulators in both shortwave and longwave portions of the spectrum (Baker and Peter 2008; Trenberth et al. 2009). Clouds cool the atmosphere by reflecting solar radiation to the space, and warm the atmosphere by acting like greenhouse gases to absorb infrared radiation (longwave). Therefore, the net radiative effects depend on cloud properties such as altitude, thickness

and transparency. For instance, low-level stratiform clouds generally cool the Earth-atmosphere system by reflecting the sunlight but not significantly changing in outgoing longwave radiation (Hartmann and Doelling 1991; Wood 2012). By contrast, high-level cirrus clouds cause warming by trapping the outgoing longwave radiation in cold temperature but transparent in visible with small reflection (Stephens and Webster 1981; Fusina et al. 2007). The indirect radiative response to aerosols involves aerosol-cloud interactions, making the results more complicated than the direct effects and vary depending on the cloud types, aerosol types, locations and time scales.

According to IPCC AR5 (2013), the aerosol-induced total radiative forcing is estimated to be between -1.33 and $-0.6\ Wm^{-2}$ with low confidence level. For the direct aerosol forcing in shortwave, an observational study based on satellite and ground-based measurement by Quass et al. (2009) estimates that the annual global average is $-1.5 \pm 0.5\ Wm^{-2}$, while a general circulation model (GCM) study by Wang et al. (2011b) in the multiscale modeling framework (MMF, replacing cumulus parameterization by cloud resolving model) estimates the forcing to be $-0.77\ Wm^{-2}$, which is only a half of the estimation ($-1.79\ Wm^{-2}$) from the other modeling studies with the GCMs adopting cumulus parameterization. In particular, Bond et al. (2013) point out that black carbon, a strong absorbing aerosol, has potential contributions to the radiative forcing ranging between -0.47 and $1.0\ Wm^{-2}$, where such wide variabilities result from the complicated responses in environmental stability, cloud coverage and large-scale circulation. As for the indirect aerosol forcing, some species (e.g., dust and soot) act as IN, thus modulating cold cloud processes (e.g., cirrus clouds), and ultimately altering the radiative budgets. Total aerosol forcing on cirrus clouds is estimated to be $0.27 \pm 0.10\ Wm^{-2}$ (Boucher et al.

2013), where the dust contributes $-0.4 \pm 0.20\ Wm^{-2}$ in net radiative forcing (Liu et al. 2012b) and the anthropogenic soot contributes $-1.14 \pm 0.39\ Wm^{-2}$ and $1.67 \pm 0.11\ Wm^{-2}$ in shortwave and longwave, respectively (Liu et al. 2009).

1.2.3 Impacts on Precipitation

Atmospheric aerosols decrease the warm-rain precipitation efficiency by acting as CCN, thus increasing droplet concentrations, narrowing droplet size distributions, and ultimately inhibiting the collision-coalescence processes (Squires and Twomey 1966; Warner and Twomey 1967; Warner 1968; Rosenfeld 1999). In the mixed-phase clouds, such as deep convections, the previous research results showing the aerosol effects are more controversial. Some studies suggest the precipitation been suppressed (Phillips et al. 2002; Khain et al. 2004; Khain and Pokrovsky 2004; Teller and Levin 2006), while other studies suggest an increase in precipitation (Wang 2005; Khain et al. 2005; Lee et al. 2009; and Fan et al. 2007). Tao et al. (2012) summarize three physical mechanisms to explain the increase of precipitation induced by aerosols suggested by earlier numerical studies: (1) the latent-heat-dynamic effect in which the aerosol invigoration effect enhances latent heating leading to stronger, (2) the cool pool effect in which higher concentration of CCN reduces droplet size and increases evaporation, leading to stronger downdraft to trigger neighbor convections, and (3) the cold-microphysics effect, in which higher CCN concentration increases the total water content consisting of numerous small liquid particles, enhances deep convections and cold-rain processes.

However, the controversy of how precipitation is affected by atmospheric aerosols results from the complexity of aerosol-cloud-circulation interactions especially in a larger

scale (e.g., climate impacts). The buffering effects have been proposed in many studies to explain the negative feedbacks or other coherent processes may partially compensate or reverse the aerosol-induced impacts from the cloud microphysics (Li et al. 2008b; Fan et al. 2013), cloud dynamics (Stevens and Feingold 2009) and convective-radiative quasi-equilibrium relationship (Grabowski and Morrison 2011). For instance, the invigoration effect may increase the net precipitation in which the enhanced convective rainfall overcomes the initial suppression of the warm-rain processes. Another example is that the increase of cloud-activate aerosol may lead to fewer droplets (warm-rain inhibition) but also higher supersaturation, which may potentially activate more smaller condensation nuclei resulting in the sublinear relation between the concentrations of cloud droplets and aerosols (Martin et al. 1994; O'Dowd et al. 1999; Ramanathan et al. 2001).

1.2.4 Aerosol Effects in Extratropics

The North Pacific storm track is uniquely characterized by high concentrations of atmospheric aerosols of both natural and anthropogenic origins (Huebert et al. 2003; Chin et al. 2004; Li et al. 2011). In recent years, the interaction between the environmental aerosols and synoptic-scale disturbances, which constitutes the storm track in this region, is drawing attention from the research community (R. Zhang et al. 2007; Zhou and Deng 2013; Wang et al. 2014). For extratropical cyclones, a modeling analysis by Thompson and Eidhammer (2014) shows that aerosols generally hinder warm-rain processes and shift precipitation northward. Observational studies suggest that, in response to increased aerosols, the Pacific storm track intensifies (R. Zhang et al. 2007) and the wintertime precipitation increases over the North Pacific region (Li et al. 2008a). By using a global

model, Zhou and Deng (2013) proved that the presence of East Asian anthropogenic aerosols enhances the activity of synoptic-scale disturbances from the central North Pacific to the Gulf of Alaska, leaving a distinct signature in surface precipitation along the west coast of the United States in boreal winter. The changes in eddy heat flux and the associated baroclinic energy conversion are found to be critical in leading to these changes, confirmed later by a separate model study (Wang et al. 2014). Affected by the long-term transport of dust from Asia, some studies suggest that California may experience stronger winter storms with severe snow events (Creamean et al. 2013).

1.3 **Summary of Research Objectives**

The majority of previous studies regarding the interactions between atmospheric aerosols and extratropical cyclones (and storm tracks) focus on the response of precipitation (latent heating) and radiative forcing. However, unlike tropical cyclones gaining energy from latent heating, the main energy source of extratropical disturbances like cyclones is the potential energy from the background atmospheric state. The change of diabatic heating resulting from aerosols is not tied to an explicit and straightforward way of the overall strength of an extratropical cyclone, which is typically measured in terms of the minimum surface pressure and/or the intensity of the mid-tropospheric trough. Therefore, it is crucial to gain a process-level understanding of the aerosol effects on the development of these cyclones by investigating how diabatic heating changes in relation with the direct and indirect effects of aerosols. Aerosol effects emerging in different parts of a cyclone (i.e., regions of deep convection versus regions of large-scale ascent) are coupled to dry baroclinic processes that dictate the growth of the cyclone and ultimately

impact the Northern Hemisphere energy and water cycle. The following list highlights the research questions that will be explored in this dissertation, and the steps that will be adopted to achieve the goals:

- How can researchers detect a robust signal of atmospheric aerosol effects from a developing cyclone given that the aerosol-induced diabatic heating and its impacts are relatively small in the dry dynamical processes? An idealized simulation with a simplest-possible approach to introduce the aerosol indirect effects is conducted to understand the dominant processes in a growth of baroclinic wave. (Chapter 2)
- How do the aerosol effects dictate the cyclone dynamics in a more realistic flow environment with a more comprehensive aerosol-circulation interaction? A general circulation model with a cloud resolving technique is adopted to fully simulate the aerosol direct and indirect effects in *both* stratiform and cumulus clouds in a developing cyclone. (Chapter 3)
- What are the collective impacts on extratropical disturbances and time-mean circulation by aerosol forcing ultimately dictating the storm track characteristics? A pair of long-term simulations is designed with pre-industrial and present aerosol emissions to identify how the aerosol forcing changes the hydrological cycle and energy budget in the Northern Hemisphere wintertime. (Chapter 4)

CHAPTER 2

FIRST-ORDER AEROSOL INDIRECT EFFECT ON THE DEVELOPMENT OF IDEALIZED BAROCLINIC WAVES

2.1 Motivation

Despite these previous efforts, it still lacks in the literature a fundamental understanding of the processes that connect the thermodynamic (heating) effects of aerosols with large-scale baroclinic processes dictating the life cycle characteristics of extratropical cyclones. Since the development of an extratropical cyclone in the real environment is a rather complicated process involving a constant exchange of energy between the cyclone and background circulation as well as nearby large-scale disturbances of different frequencies, these so-called dry dynamical processes (such as baroclinic and barotropic energy conversion) tend to be of much greater magnitude compared to energy production driven by changing cloud microphysical properties, hence the aerosol indirect effect. To be able to obtain a robust signal of aerosol impact on a disturbance largely dictated by ‘‘dry’’ dynamical processes, an ‘‘idealized’’ situation is considered first, in which we 1) minimize the interaction of growing cyclones with nearby large-scale disturbances through the use of the baroclinic wave test case of the WRF Model, 2) mimic the first-order effect of changing aerosols through changing the cloud droplet number directly and bypassing detailed aerosol activation processes in the model, and 3) restrict our analysis to the initial transient response of this idealized baroclinic wave to increased concentration of environmental aerosols to minimize the contamination of cloud microphysical effects by larger-amplitude dry dynamical processes. Section 2.2 provides a

brief description of the numerical model used, our experiment design, and analysis approaches. The main results are discussed in section 2.3, and concluding remarks are made in section 2.4.

2.2 Model and Methods

2.2.1 WRF Model for Idealized Baroclinic Waves

The simulations in this study are conducted by the Advanced Research version of Weather Research and Forecasting (WRF) Model, version 3.5. The dynamical core is based on fully-compressible, nonhydrostatic Eulerian equations. The horizontal grids use the Arakawa C-grid staggering, and the vertical coordinate is terrain-following, hydrostatic-pressure levels with a constant pressure on the top of model absorbing gravity waves. The prognostic variables include horizontal velocity, vertical velocity as well as perturbations of potential temperature, geopotential height and surface pressure with the options of turbulent kinetic energy and other scalars (e.g., mixing ratios of hydrometers, chemical species and tracers). Nonconserved variables (e.g., temperature, pressure, and density) are diagnosed from the conserved prognostic variables. The spatial discretization is 5^{th} and 3^{rd} order advection operators for horizontal and vertical, separately, in the fully conservative flux divergence scheme to conserve the fundamental properties (e.g., mass and potential vorticity). And the time-split integration is 3^{rd} order Runge-Kutta scheme with smaller timestep (4 sound step per timestep) for acoustic and gravity waves. The model in this study is configured specifically for idealized moist baroclinic waves, where the initial condition is a zonally symmetric westerly jet satisfying the geostrophic and hydrostatic

balance. The domain is periodic on the west and east boundaries and symmetric on the north and south boundaries.

2.2.2 Experiment Design and Model Setup

The simulations were initialized with a zonally symmetric and baroclinically unstable jet on an f-plane over a water surface. The model has 64 σ levels in the vertical, and the horizontal resolution is 15 km with 266 x 534 grid points. A periodic boundary condition is adopted for the x direction. The model physics was configured with the Morrison double-moment microphysics, simplified Arakawa–Schubert cumulus parameterization, Monin–Obukhov boundary layer scheme, and the radiation scheme from the Rapid Radiative Transfer Model for GCMs (RRTMG). It has been suggested that the double-moment scheme, which can predict both mixing ratios and number concentrations, would be necessary to deal with the aerosol indirect effect (Li et al. 2008b). The Morrison scheme applies the Kohler theory to calculate the nucleation of droplets given the environmental supersaturation and the distribution of aerosols, which is determined by the distribution parameters (e.g., total number concentration, slope of the dry aerosol size distribution, and radius of the smallest dry aerosol particle). However, as discussed toward the end of the introduction, here we chose not to modify the concentration of aerosols but instead to directly change the concentration of cloud droplet number in an attempt to introduce in the simplest possible way the first-order indirect effect associated with changing aerosol concentrations.

To eliminate gravity wave contamination created by imbalance in the prescribed initial jet profile, the model was first integrated for two inertial periods (i.e., 37 h), and all

fields were time averaged over this period to generate an adjusted initial condition. This eliminating procedure was done twice to create the final initial condition used in all model experiments (Plougonven and Snyder 2007).

Two groups of experiments were conducted using the same initial condition. One is the control group where the default cloud droplet number concentration (DNC) of $250\ cm^{-3}$ was used. The other is the double-DNC group where we increase the DNC to $500\ cm^{-3}$. Within each group, we perturbed the magnitude of the initial zonal wind on a randomly selected 5% of the model grid points by 0.1% to create 10 ensemble members in each group. The ensemble-mean results from the two groups were then compared to identify the initial transient response of the idealized baroclinic wave (cyclone) to changes in environmental aerosol concentration in an approximate way since we did not explicitly treat the emission, activation, and scavenging processes of aerosols.

The effective radius of the cloud droplet used by the model radiation scheme in our configuration is not related to the DNC. We modified the radiation code to calculate the effective radius of the cloud droplet as a function of mixing ratio and droplet number concentration but left the effective radius of ice particles unchanged (as a function of only temperature) because of the large uncertainty on the relation between the aerosol properties and the effective radius of ice.

2.2.3 Potential Vorticity Inversion

In the model results diagnosis, we calculated the net generation of potential vorticity (PV) from diabatic heating processes in the quasi-geostrophic (QG) framework (e.g., Kuo 1972). The diabatic heating profile changes the static stability and thus

redistributes the PV patterns. The local change rate of PV due to the diabatic heating is given by

$$\frac{\partial q}{\partial t} = \frac{f}{c_p}\frac{\partial}{\partial p}\left[\frac{\theta h}{T}\left(\frac{\partial \theta_s}{\partial p}\right)^{-1}\right], \tag{2-1}$$

where q is the PV (s^{-1}), f the Coriolis parameter (s^{-1}), c_p the heat capacity at constant pressure $(J\ kg^{-1}\ K^{-1})$, T the air temperature (K), θ the potential temperature (K), h the diabatic heating rate $(J\ kg^{-1}\ s^{-1})$, and θ_s the horizontally averaged potential temperature (K). The PV generation is calculated separately from each diabatic heating (e.g., latent or radiative heating) difference between the double-DNC and control groups. We then applied a PV inversion tool (Black and Dole 1993) to attribute the simulated circulation response to changes in various PV anomalies as a result of the doubling of the DNC. The relation between a PV anomaly q' and the corresponding geopotential height anomaly $\Phi'\ (m)$ can be written as follows:

$$\mathrm{q}' = \frac{\nabla^2 \Phi'}{\mathrm{f}_0} + \mathrm{f}_0 \frac{\partial}{\partial \mathrm{p}}\left(\frac{1}{\sigma}\frac{\partial \Phi'}{\partial \mathrm{p}}\right), \tag{2-2}$$

where $\sigma = \sigma(p)$ is a static stability parameter $(m^4\ s^2\ kg^{-2})$. A relaxation technique is employed to invert (2-2) for a given PV anomaly generated from a source of heating to obtain the corresponding response of circulation Φ'.

2.3 Initial Response to Doubling of Droplet Number Concentration

The black line in Figure 2.1 shows the evolution of the minimum surface pressure (a measure of the intensity of the baroclinic wave) for the ensemble mean of the control group. The surface low undergoes some initial oscillations, drops slowly, and then rapidly intensifies starting from the end of day 3. The baroclinic wave reaches its peak intensity on

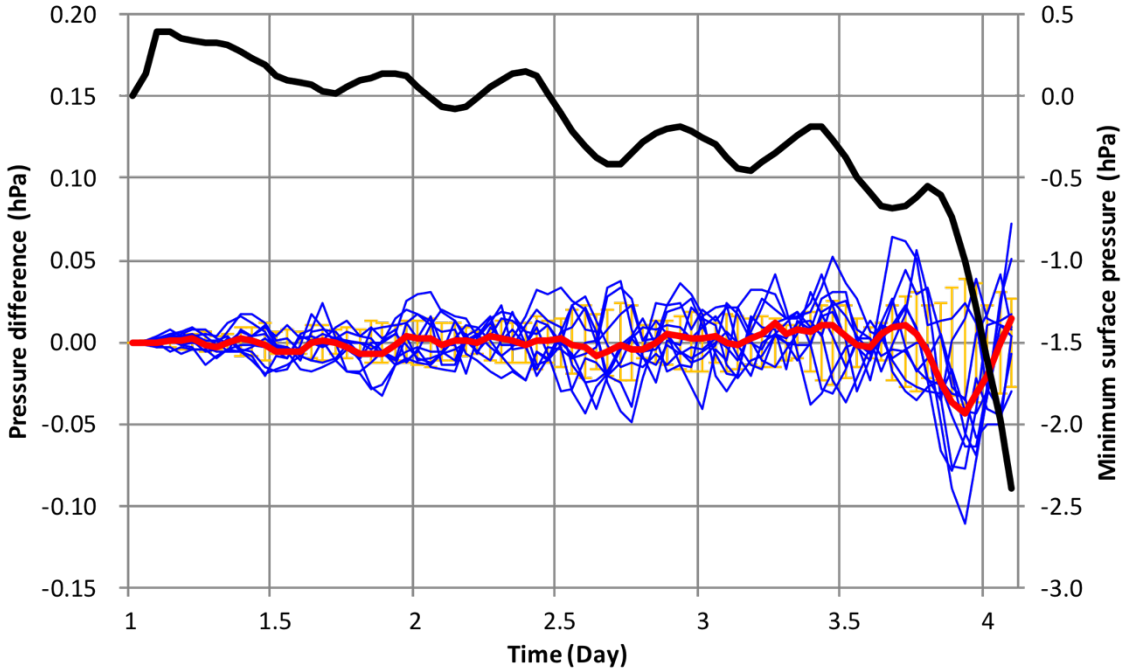

Figure 2.1 Minimum surface pressure from 0000 UTC on day 1 to 0200 UTC on day 4. The black line is the ensemble mean of surface pressure drop for the control group. The blue lines are the differences of minimum surface pressure between the control and double-DNC groups, and the mean is shown as a red line. The orange bars are the standard deviations among the ensembles for the control group.

day 6 with an approximate 60-hPa drop in the surface pressure compared to the initial state (not shown). Blue lines in Figure 2.1 indicate the differences of the minimum surface pressure between the double-DNC group and the control group for individual ensemble members, and the orange bars show the standard deviation among the 10 ensembles. During the first 3 days, the difference of the ensemble mean between the double DNC and control (red line) is in general smaller than the standard deviation. Between 1900 UTC on day 3 and 0000 UTC on day 4, the ensemble mean of the double-DNC and control difference exceeds the orange bars for the first time, marking the detection of statistically significant effects of doubling the DNC on the development of the wave. We therefore

focus our analysis on this initial transient stage. After this transient stage, the ensemble spread amplifies rapidly as a result of strong nonlinearity in the system, making it difficult to identify statistically significant responses. For the initial transient stage, the minimum surface pressure in the double-DNC group is on average 0.05hPa lower than that in the control group. This amounts to an approximate 5% increase in the initial wave intensity (measured in terms of the minimum surface pressure of the corresponding cyclone) as a result of the DNC doubling.

Figure 2.2a shows the ensemble-mean total cloud water of the control group averaged over the initial transient stage (contours). The system is clearly characterized by large-scale stratiform clouds located on the east side of the surface low (green contours) over the warm front region. Convective activity and ice clouds are rare during this period, suggesting that the main effects of doubling the DNC are captured by changes in stratiform clouds resulting from large-scale ascent ahead of the surface warm front. Color shading in Figure 2.2a is the difference of total cloud water between the double-DNC and control groups. Summed over the entire model domain, the total cloud water mixing ratio in the double-DNC experiments increases about 15% compared to the control, and the change mostly comes from the liquid water in a cloud layer located vertically at about 800 hPa (not shown). The three-dimensional (3D) diabatic heating anomaly as a result of the cloud change leads to changes in the lower- to mid-tropospheric geopotential height. Figure 2.2b plots the difference of the 650-hPa geopotential height between the double-DNC and control experiments (color shading). It is clear that DNC doubling causes strengthening of both the trough (negative height anomaly in the control; dashed contours in Figure 2.2b) and ridge (positive height anomaly in the control; solid contours in Figure 2.2b). In other

words, the amplitude of the idealized baroclinic wave strengthens as a result of the doubling of the DNC. This intensity change is consistent with the strengthening of the surface low discussed previously (Figure 2.1).

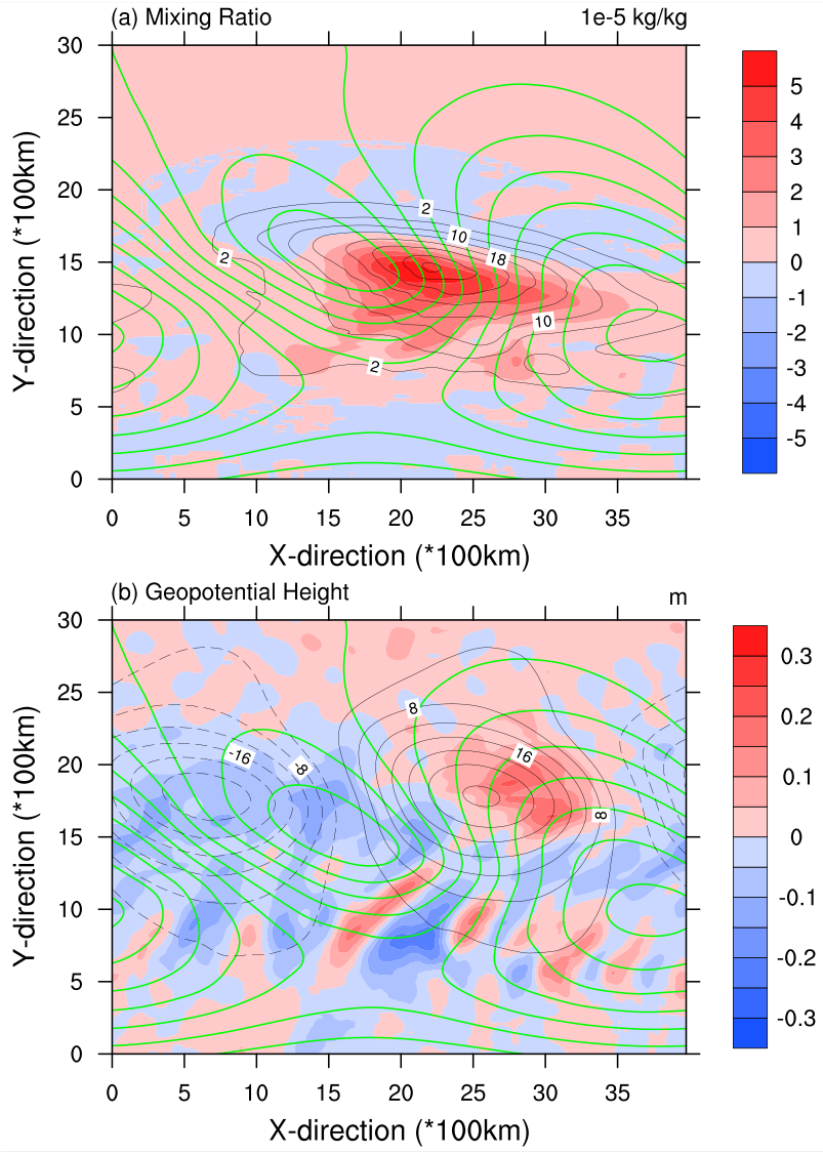

Figure 2.2 (a) Vertically averaged mixing ratio of total cloud water and (b) geopotential height perturbation (subtracting the zonal mean) at 650 hPa in the 6-h initial transient stage. The mixing ratio was averaged between the surface and 650 hPa, and the total cloud water includes liquid cloud water, rainwater, ice, snow, and graupel. The black contour is the ensemble mean of the control group, and the color shading shows the difference between the double-DNC and control groups. The green contour is the surface pressure of the control group with a low center in the middle of the domain and a high center on the right boundary.

2.4 Aerosol-Induced Changes in Diabatic Heating

The vertically averaged total diabatic heating below 650hPa for the control group is shown in Figure 2.3a (contours) together with the difference between the double-DNC and control groups (color shading). The main area of heating (positive values; solid contours) collocates with the cloudy region (see Figure 2.2a for reference) and is largely contributed by latent heating (Figure 2.3b). Cooling (negative values; dashed contours) on the other hand largely stems from radiative processes (Figure 2.3c). The magnitude of diabatic heating due to boundary layer mixing (Figure 2.3d) is more than one order of magnitude smaller compared to those of latent and radiative heating.

Doubling of the DNC induces significant changes in diabatic heating, mainly found in the latent heating field (Figure 2.3b). The change in latent heating is characterized by a dipole anomaly with positive values to the north and negative values to the south near the center of the system (1200–1800 km in the y direction and 1200–2700 km in the x direction). The positive values of this dipole anomaly tend to reinforce the total diabatic heating maximum found in the control, and the negative values also slightly enhance the total diabatic cooling (mainly from radiative processes; see Figure 2.3c) found south of the total heating maximum (Figure 2.3a; contours). Thus, the overall effect of latent heating change near the center of the system is to strengthen the diabatic heating structure in the control. Since it is known that diabatic effects tend to play a secondary but positive role in cyclone intensification, the heating change due to the doubling of the DNC seen here is consistent with the strengthening of the baroclinic wave found previously (e.g., R. Zhang et al. 2007). The changes in radiative heating and heating due to boundary layer mixing are much weaker and less organized compared to the changes in latent heating (Figures 3c,d).

Note that large values of heating change are also found in the emerging convective-scale waves located near the south of the cyclone system. These waves mainly consist of convection that developed ahead of a weak surface cold front, and at this stage, they are too far away from the center of the system to make significant contributions to the development of the cyclone. This further highlights the difference between an extratropical cyclone dominated by dry dynamics and a tropical cyclone dominated by moist dynamics where convective heating is always critical for storm intensification.

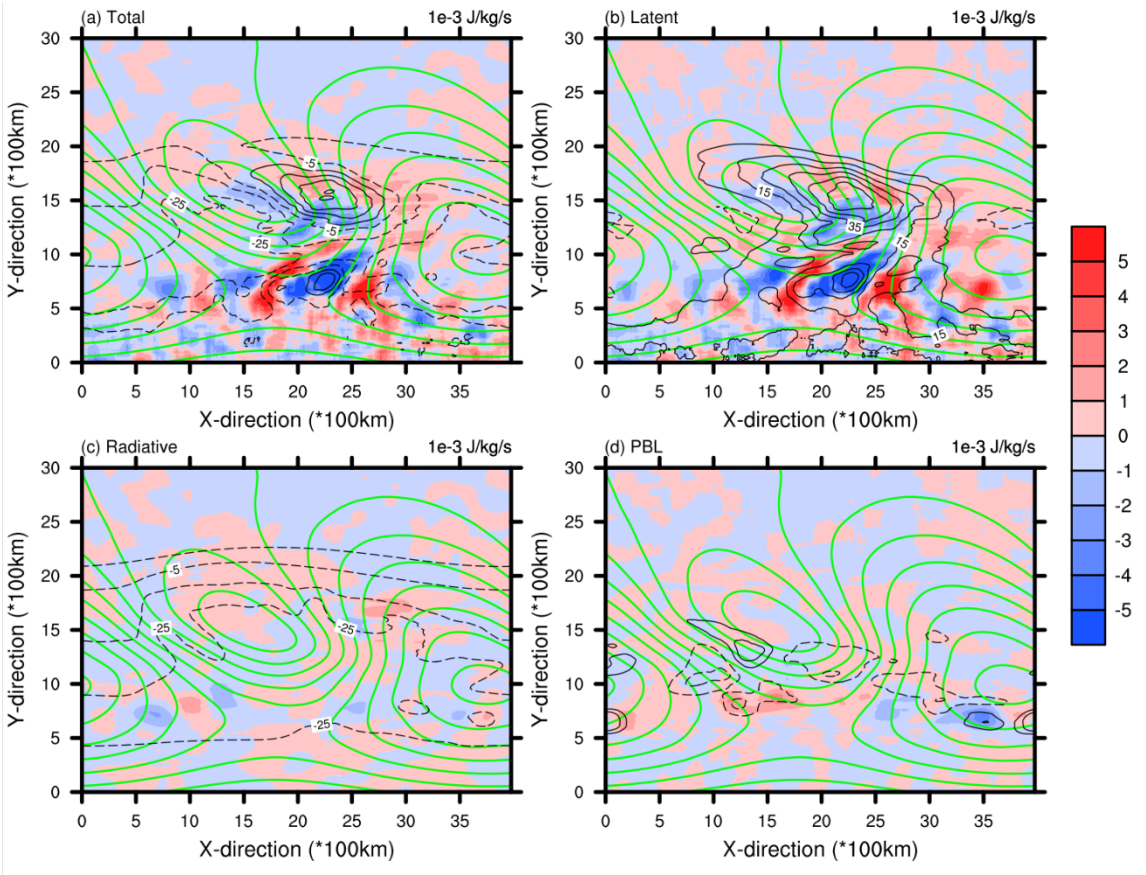

Figure 2.3 The heating patterns of (a) total diabatic heating, (b) latent heating, (c) radiative heating, and (d) heating due to the boundary layer scheme in the 6-h initial transient stage vertically averaged from the surface to 650 hPa. The control group (black contour) and difference (color shading) are shown as in Figure 2.2. The green contour shows the ensemble mean of the surface pressure for the control group.

2.5 Aerosol-Induced Changes in Potential Vorticity Generation

Piecewise PV inversion provides a powerful tool for examining the response of the circulation of a disturbance/wave (e.g., in terms of geopotential height) to diabatic heating changes associated with multiple processes. Since the net PV generation by diabatic processes is proportional to the vertical gradient of the diabatic heating rate, we plot first in Figure 2.4a the vertical profile of the diabatic heating-rate change from the control to the double-DNC experiments averaged over the cloudy region east of the surface low where the total diabatic heating rate in the control exceeds $5\times10^{-3}\ J\ kg^{-1}\ s^{-1}$ in Figure 2.3a. Note that in all the WRF experiments we conducted, the total diabatic heating is dominated by longwave radiative cooling above and by latent heating/cooling from moist processes below the level of 750 hPa, where the cooling peaks at 700 hPa and warming peaks at 850 hPa (not shown).

In the double-DNC experiments, the cloud water mixing ratio increases by 10%–25% in the lower troposphere, and the peak of the mixing ratio difference is found at levels below the peak of the mixing ratio in control runs. Therefore, the layer of stratiform clouds shifts downward slightly as a result of doubling the DNC. Consequently, the latent heating difference in Figure 2.4a shows a reduction of about 2% at 750 hPa and an enhancement underneath this level. Since doubling the DNC makes cloud droplets smaller, raindrop amounts decrease and slow down the terminal velocity. This leads to enhanced cooling due to re-evaporation below 850 hPa. Changes in the vertical profiles of atmospheric temperature, clouds, and cloud optical properties modify the vertical profile of radiative

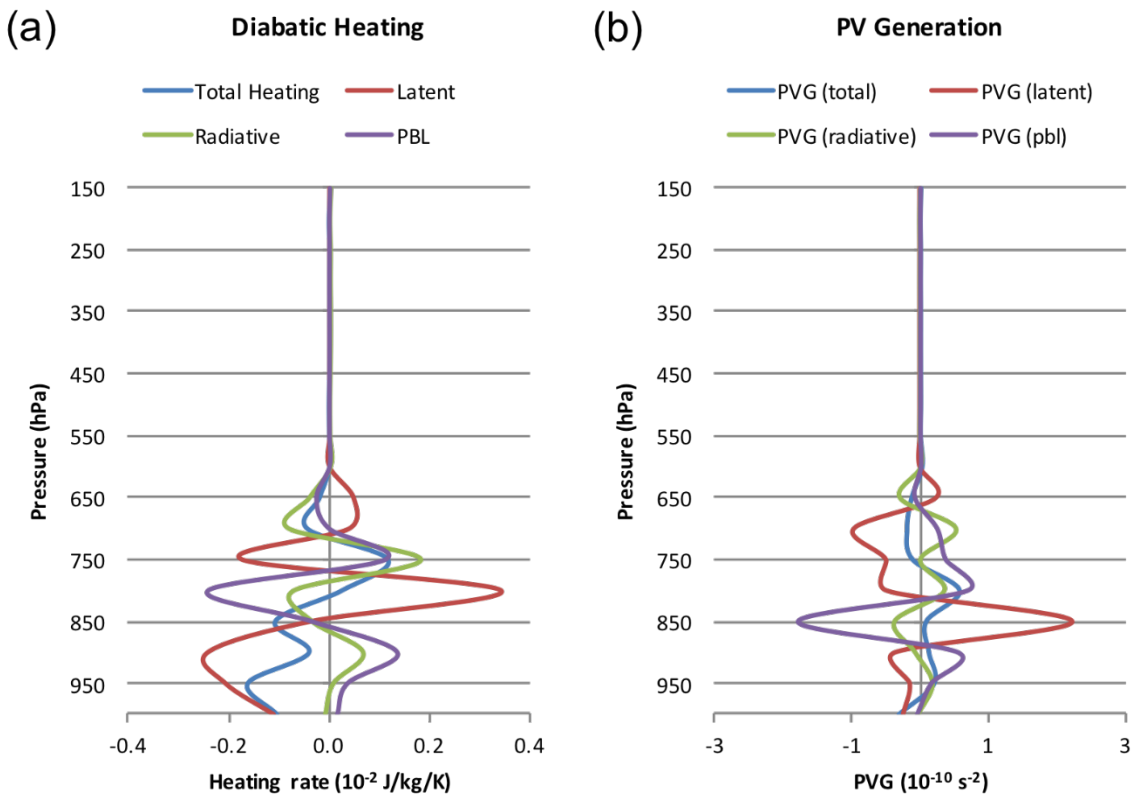

Figure 2.4 (a) Vertical profiles of diabatic heating and (b) generation of PV in the 6-h transient stage. The profiles were averaged over the region where the heating exceeds $5\times10^{-3}\ J\ kg^{-1}\ s^{-1}$ in Figure 2.3a.

heating rate. For example, the reduced longwave radiative cooling at 750 hPa in the double-DNC experiments is likely a result of decreased cloud amount at this level.

Dynamically, the changes in the vertical profile of the diabatic heating rate translate into changes in PV generation. Figure 2.4b shows the difference in diabatic PV generation between the double-DNC group and the control group as a function of height. The overall difference is characterized by net PV destruction above and net positive PV generation below the 750-hPa layer. This structure is consistent with the vertical gradient of the change in total diabatic heating (Figure 2.4a). Since the areal average is done to the east of the surface low—a region marked by a mid-tropospheric ridge (see Figure 2.2b)—the negative

PV generation enhances anticyclonic flow above 750hPa and strengthens the mid-tropospheric (650 hPa) ridge. In a similar manner, the positive PV generation below 750 hPa weakly enhances cyclonic flow in the lower troposphere. As viewed from the perspective of PV generation, the net effect of the diabatic heating change thus leads to strengthening of the baroclinic wave, consistent with the previous discussion.

To gain a more direct view of this strengthening effect, we invert the difference of the diabatic PV generation between the double-DNC and control groups to derive the corresponding difference in 650-hPa geopotential height. The PV inversion results are shown in Figure 2.5, with black contours indicating the geopotential height distribution in the control and color shading indicating geopotential height differences related to changes in total diabatic heating (Figure 2.5a), latent heating (Figure 2.5b), radiative heating (Figure 2.5c), and heating due to boundary layer mixing (Figure 2.5d).

Comparing Figure 2.5a to Figure 2.2b, the geopotential height differences obtained through inverting diabatic PV generation capture the enhancement of the ridge. The inversion results over the trough region show less consistency, suggesting that the deepening of the trough seen in Figure 2.2b is probably more related to a horizontal redistribution of PV instead of direct diabatic PV generation. In other words, the deepening of the trough during this initial transient stage is likely connected to the doubling of the DNC and diabatic heating change only indirectly via changes in dry dynamics (e.g., PV

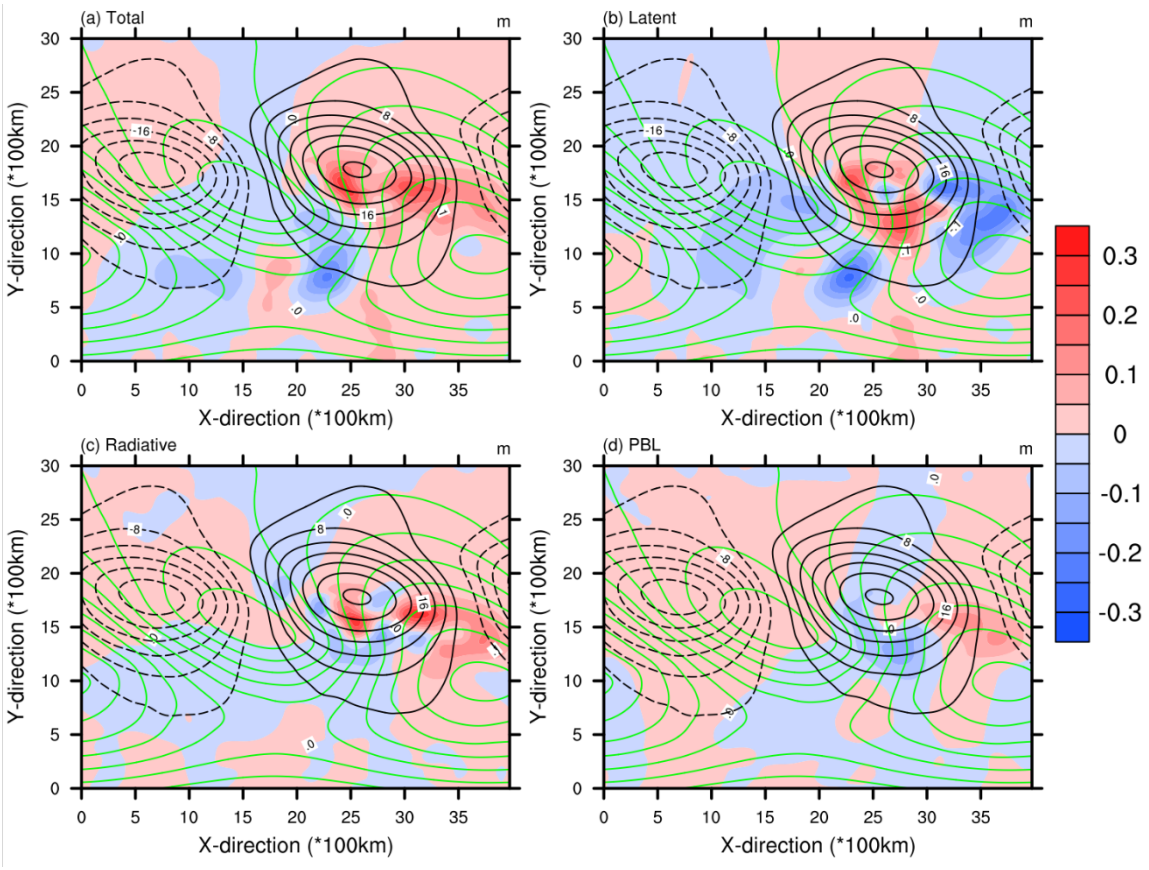

Figure 2.5 The inversion results of anomalous geopotential height at 650 hPa from the PV generated by (a) total diabatic heating, (b) latent heating, (c) radiative heating, and (d) heating due to the boundary layer scheme shown as color shading. The black and green contours show the model output of the control run as in Figure 2.2b.

advection) that are initiated by a strengthened ridge. This distinction between trough and ridge strengthening also partly explains why the positive values of the dipole structure of the diabatic heating change project more efficiently onto the latent heating maxima found in the control experiments (Figure 2.3a). Further partitioning of the PV generation shows that latent heating indeed plays the most important role, as the strengthening of the system in terms of geopotential height differences associated with latent heating change capture the main structure of the total height differences, especially at the location of the 650-hPa

ridge. The effects of radiative heating and boundary layer heating change tend to weaken the trough in general, but they show positive effects near the ridge center. The radiative heating change in particular has positive contributions to the strengthening of the ridge, while the boundary layer heating, which is related to turbulent mixing, tends to be out of phase with the latent heating change. Note that toward the east of the ridge center where clouds are absent, the effects of radiative and latent heating are the main contributors to the total heating change (i.e., the mismatch found between Figures 2.5a and 2.5b over the region 3000–3500 km in the y direction and 1500 km in the x direction).

2.6 Section Summary

In Chapter 2, ensemble simulations of an idealized baroclinic wave were conducted with the WRF Model to investigate the effects of increasing environmental aerosol concentrations on the development of the wave and its surface manifestation—an extratropical cyclone. The aerosol effect was introduced into the model through the simplest possible way (i.e., a doubling of the DNC in the model). Statistically significant differences between the double-DNC and the control experiment groups were identified for an initial transient stage (roughly 3 days after the integration) before the cyclone enters the stage of rapid intensification. The lack of substantial convective activity near the cyclone center during this stage allows us to examine the microphysical (indirect) effect of aerosols exerted through changes in large-scale ascent and stratiform clouds even though the model cumulus schemes are not coupled with microphysics.

Doubling of the DNC increases total cloud water in the model, lowers the cloud level, and enhances latent heating to the east of the surface low ahead of the surface warm

front. This heating change strengthens the mid-tropospheric ridge. The changes in dry dynamical processes (e.g., advection of PV) as a result of the ridge strengthening further lead to the deepening of the trough and ultimately produce a weak yet statistically significant strengthening of the baroclinic wave as a result of the DNC doubling. The relative contributions of latent, radiative, and boundary layer heating to the strengthening of the system were quantified through piecewise PV inversion. An examination of the mid-tropospheric geopotential height differences related to various PV generation processes confirms the critical role of latent heating change in strengthening the mid-tropospheric ridge. In general, the change of diabatic heating due to the DNC doubling produces negative (positive) PV in the mid-troposphere (lower troposphere) to the east of the surface low and enhances the anticyclonic (cyclonic) flow there.

The results reported here serve to provide a preliminary look at processes that translate the thermodynamic effects of aerosols into dynamical changes in an extratropical synoptic-scale disturbance whose life cycle is known to be dominated by dry dynamical processes (e.g., baroclinic and barotropic energy conversion). Our results highlight the distinction in how tropical cyclones and extratropical cyclones are influenced by environmental aerosols. Aerosol effects on deep convective clouds (e.g., convection invigoration) are clearly crucial for understanding interactions between tropical cyclones and aerosols. However, convective clouds play only a secondary role in the overall life cycle of an extratropical cyclone, and the intensity of local convection does not positively correlate with the overall strength of an extratropical cyclone. As a result of the dominant role of dry dynamical processes in such a storm, the detection of aerosol effects becomes very challenging, and statistically robust signals might emerge for only a brief and transient

period as we found here. Finally, we recognize that a more comprehensive treatment of aerosols and a global domain allowing full interactions between a baroclinic wave and its background state are needed to complete the picture of the aerosol–extratropical cyclone interaction, which will be addressed in the next chapter.

The work presented in this chapter is published in Journal of Climate (Lu and Deng 2015).

CHAPTER 3

AEROSOL EFFECTS ON THE DEVELOPMENT OF REALISTIC EXTRATROPICAL SYNOPTIC-SCALE DISTURBANCES

3.1 Motivation

In Chapter 2, we use the idealized baroclinic wave simulations made with the Weather Research and Forecasting (WRF) Model to examine the response of a cyclone to the increased cloud droplet number concentration. In response to such increases, the cyclone in the model strengthens during the stage of its initial transient growth as indicated by an intensified mid-tropospheric trough and ridge. The ridge intensification turns out to be a direct response to diabatic heating change caused by increased droplet number concentration, while subsequent dry dynamical processes lead to the deepening of the trough. Despite these findings, we recognize that directly increasing the cloud droplet number concentration is one of the crudest ways of representing aerosol microphysical effect. The study in Chapter 2 does not consider the explicit process of droplet activation and most importantly the impact of aerosols on deep convection. Moreover, the baroclinic wave was originated from a zonally symmetric initial condition and evolved in a zonally periodic domain. It is worth knowing what the response will be if the cyclone is developing in a more realistic flow environment where interactions between the cyclone and surrounding (weather) systems are possible.

In this chapter, we resort to a global model with ‘‘superparameterization’’ to further investigate the aerosol effects on the development of extratropical cyclones. With superparameterization, the conventional cumulus scheme is replaced with a cloud-

resolving model at each grid point of the global model. This allows explicit representations of subgrid variability of cloud dynamics and microphysics and the full interaction between aerosols and deep convection. The use of a global domain also provides a more realistic environment for cyclones under consideration to have dry energy exchanges (in which moisture processes and latent heating may only play secondary roles) with the background state and surrounding systems. Section 3.2 is a brief description of the model used and the experiment design. The main results are documented and discussed in section 3.3. Section 3.4 provides some concluding remarks and additional discussion of the broader implications of the findings.

3.2 **Data and Methods**

3.2.1 Superparameterized Community Atmosphere Model

The superparameterized Community Atmosphere Model (SP-CAM) is used in this study for investigating the aerosol effects on the development of extratropical cyclones. Detail descriptions of the SP-CAM can be found in Wang et al. (2011a). The SP-CAM is a multiscale modeling framework (MMF) model that combines a general circulation model (GCM) with a cloud-resolving model (CRM) and uses an explicit cloud-parameterized-pollutant (ECPP) approach (Gustafson et al. 2008) to handle the interaction between clouds and aerosols. By replacing the conventional cumulus parameterization with a CRM, the SP-CAM has a better representation of aerosol effects in global models by allowing a more physical treatment of aerosol–cloud interactions in both stratiform and convective clouds.

The host GCM is the Community Atmosphere Model, version 5.2 (CAM5). A two-dimensional (x–z plane) CRM named the System for Atmospheric Modeling (SAM;

Khairoutdinov and Randall 2003) is embedded in each GCM grid column to replace the conventional moist physics, convective cloud, turbulence, and boundary layer parameterizations in CAM5. In every GCM time step (10 min), the CRM resolves the cloud-scale physical processes with a 20-s time step and returns the tendencies of temperature and moisture back to the GCM scale.

This CRM uses a double-moment cloud microphysics scheme (Morrison et al. 2005) to predict the number concentration and mass mixing ratio of five hydrometeors (cloud droplet, ice crystal, rain droplet, snow particle, and graupel particle). It has been suggested that a double-moment scheme, which can predict both mixing ratio and number concentration, is necessary to represent the aerosol indirect effect (Li et al. 2008). The scheme of Morrison et al. (2005) applies Kohler theory to calculate the nucleation of droplets given the environmental supersaturation and the distribution of aerosols. The ice nucleation (IN) mechanisms are also considered, but the treatment does not directly link heterogeneous IN to aerosols.

The GCM uses a modal approach to treat aerosols (Liu et al. 2012a) in three lognormal modes: Aitken mode, accumulation mode, and coarse mode. The modal approach predicts both the species mass and number mixing ratios with prescribed mode widths. The species include sulfate, secondary organic aerosol (SOA), and sea salt in the Aitken mode; sulfate, SOA, black carbon, primary organic matter (POM), sea salt, and dust in the accumulation mode; and sulfate, sea salt, and dust in the coarse mode. The emission of aerosols for each species and mode is prescribed in external files with an annual cycle at the year-2000 values. The interstitial aerosols (suspended in air) are transported three

dimensionally in the GCM scale, while the cloudborne aerosols (i.e., in cloud droplets) are not transported except for vertical turbulent mixing.

The ECPP approach replaces the conventional treatment (in CAM5) of cloud-related aerosols and trace gas processes in a more physical manner. The statistics of the cloud properties derived from the CRM simulations are used to drive the aerosol and chemical processes on the GCM scale. With this approach, the SP-CAM can predict the evolution of both the interstitial aerosols and cloudborne aerosols in all cloud types, including convective clouds, while the conventional CAM5 deals with the cloudborne aerosols only in stratiform clouds.

The Rapid Radiative Transfer Model for GCMs (RRTMG) radiation scheme (Mlawer et al. 1997) is applied on the CRM grid on every GCM time step (10 min). The aerosol optical properties are retrieved on the CRM scale by calculating the water uptake from Kohler theory with the relative humidity on the CRM scale and the dry aerosol properties on the GCM scale.

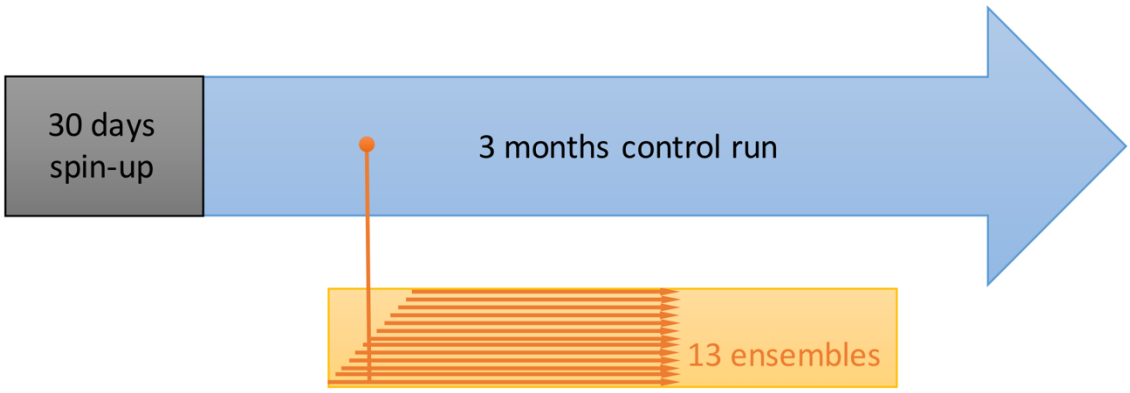

Figure 3.1 Schematic plot for the experiment design. The SP-CAM was first integrated for 30 days and then run for 90 days (3 months) in a winter season, referred to as the control run. The analyzed case in this study was selected from the control run, targeting a pre-developing stage of a cyclone. A total of 13 ensembles of 1X-EXP and 5X-EXP pairs were conducted by starting the simulations at a 30-min interval between.

3.2.2 Experiment Design and Model Setup

The resolution of the GCM used in this study is $1.9^o \times 2.5^o$ with 30 levels in a hybrid sigma–pressure coordinate, and the time step is 10 min. The climatological, seasonally varying sea surface temperature and sea ice provide boundary conditions for the GCM over oceans (Hurrell et al. 2008). Embedded in each GCM column, the two-dimensional CRM has 32 grid points in the x direction with a 4-km resolution and 28 levels coinciding with the lowest 28 levels of the GCM. The time step of the CRM is 20 s. A schematic diagram for how we designed the experiments is shown in Figure 3.1. The SP-CAM was first integrated for 30 days to spin up and then run for another 90 days to get outputs of a full winter season, referred to as the control run.

In the control run, there are multiple cases of baroclinic waves (extratropical cyclones) developing and dissipating along the North Pacific storm track. We selected a growing baroclinic wave with classic features (i.e., closed contours of a surface low, distinct surface cold and warm fronts, and well-defined upstream mid-tropospheric trough) in the North Pacific basin as the target event. To investigate the aerosol effects on its development, we conducted simulations with and without increased aerosol concentration. Since the three-dimensional distributions of aerosols vary with time in the model as a result of transport processes and various sources and sinks, it is challenging to extract their net effects on the life cycle of an individual weather disturbance. To come up with a control and perturbed case with minimum ambiguity, we chose the atmospheric state of the predeveloping (right before the rapid intensification) stage of the target cyclone as the initial condition, fixed the spatial distributions of the aerosols to their states in this initial condition, and integrated the model forward for an additional seven days to document the

evolution of the cyclone. This experiment is referred as 1X-EXP. In a similar way, 5X-EXP was conducted with the initial mass and number mixing ratios of all aerosol species increased by 4 times and held constant throughout the seven days of model integration. Furthermore, designating the original model time of the initial condition as "0 hour", we generated 13 ensemble members separately for 1X-EXP and 5X-EXP by sampling the initial condition at a 30-min intervals from the period between -3 and +3 hours. Since both the aerosol distributions and the atmospheric state vary slightly during this 6-h period, we effectively introduced small perturbations to the system, and the 13 ensembles thus provided us measures of the robustness of the detected aerosol effects on cyclone development. These effects are quantified in our study as the difference between 5X-EXP and 1X-EXP (5X-EXP minus 1X-EXP).

3.2.3 Separation of Aerosol Direct and Indirect Effects in Radiation

To further separate the aerosol direct and indirect effect in radiative processes, we calculated three radiative heating rates by modifying optical depth in the model. The total optical depth for radiation transfer calculations is the sum of air and cloud optical depths as well as the aerosol optical depth (AOD). The clear-sky (CS) radiative heating is obtained by neglecting the optical depth of clouds. The pristine-clear-sky (PCS) radiative heating is obtained by using only the optical depth of air. Therefore, the radiative heating due to clouds (RHC) can be defined as the difference between total radiative heating rate and CS, and the radiative heating resulting from direct aerosol effects (RHA) can be defined as the difference between CS and PCS. In this study, we approximate the aerosol direct effect by subtracting the RHA in 1X-EXP from that in 5X-EXP and the aerosol (first) indirect effect

by subtracting the RHC in 1X-EXP from that in 5X-EXP. In other words, the aerosol direct effect is defined as the change of aerosol absorption/scattering in response to increased aerosols, and the aerosol indirect effect is defined as the change of cloud radiative heating in response to increased aerosols. Note that the latter actually includes the change of cloud radiative heating resulting from dynamically driven changes in cloud properties also, which nevertheless ultimately stems from aerosol change according to our experiment design.

3.3 Structure and Intensity Changes of the Disturbances in Response to Aerosol Increase

Figure 3.2 shows the evolutions of minimum surface pressure during the first five days. The maximum ensemble spread of 1X-EXP is around 2 mb with an average around 1 mb during this period (1 mb = 1 hPa). Since the ensemble spread is small, only the ensemble mean of 1X-EXP is shown as the black curve. Note that the time axis in Figure 3.2 is a reference time frame; because the initial time of each ensemble differs by a 30-min interval, the time axis is cropped and the 0 hour in Figure 3.2 is not the actual initial time for each ensemble member.

The intensity of the target cyclone undergoes some initial oscillations and then rapidly increases starting from day 2. Its central pressure drops by about 45 mb and reaches its maximum intensity on day 4. The red curve is the ensemble mean of the difference between 5X-EXP and 1X-EXP, and the blue curves correspond to the differences from each ensemble member. The differences are generally positive during the rapid intensification stage of the cyclone, indicating a consistent, weakened growth of the cyclone in the response to increased aerosol concentrations. It amounts to an approximate

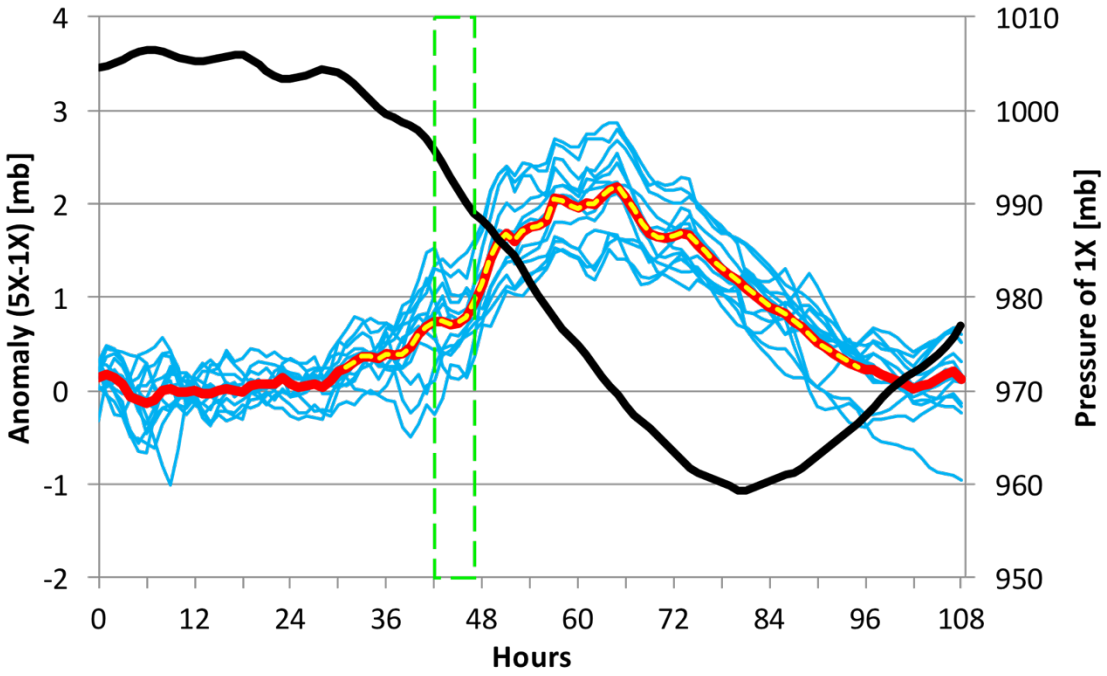

Figure 3.2 Evolution of the minimum surface pressure (black curve) for the ensemble mean of 1X-EXP. The blue curves are the differences between 5X-EXP and 1X-EXP (5X-EXP minus 1X-EXP) for the 13 ensembles, and the red curve indicates their mean. The mean highlighted with the yellow dash indicates a statistical significance of 99% with Welch's t test.

5% (2.2 out of 45 mb) drop in the growth rate. The maximum difference (5X-EXP minus 1X-EXP) occurs toward the end of day 3—about 12 h before the cyclone reaches its maximum intensity. To reveal the structural changes in the cyclone as a result of increased aerosol concentrations, we next focus our analysis on the 6-h window during the rapid intensification stage marked by the green box in Figure 3.2. Various dynamical and thermodynamical fields as well as distributions of hydrometeors will be examined to identify and understand processes that are responsible for the weakened growth of the cyclone in 5X-EXP.

Figure 3.3a shows the structure of the cyclone in 1X-EXP ensemble mean averaged over the 6-h window. The green contours are the perturbation surface pressure associated with the cyclone, which is obtained as the difference between the total surface pressure and the winter-mean surface pressure in the model (i.e., the 90-day average of the control run). The blue contours in Figure 3.3a indicate the geopotential height anomaly at 500 mb (zonal mean removed), and color shading shows the total cloud water path, which is the sum of water mixing ratios of the five hydrometeors (cloud droplets, rain, ice, snow, and graupel). During this intensification stage, the 500-mb trough is located upstream near the storm center (minimum surface pressure), while the ridge is displaced downstream to the northeast. The westward tilt with height seen here guarantees a positive feedback of lower-tropospheric thermal advection to the strength of the mid-tropospheric trough and ridge (i.e., cold advection underneath the trough and warm advection underneath the ridge)—

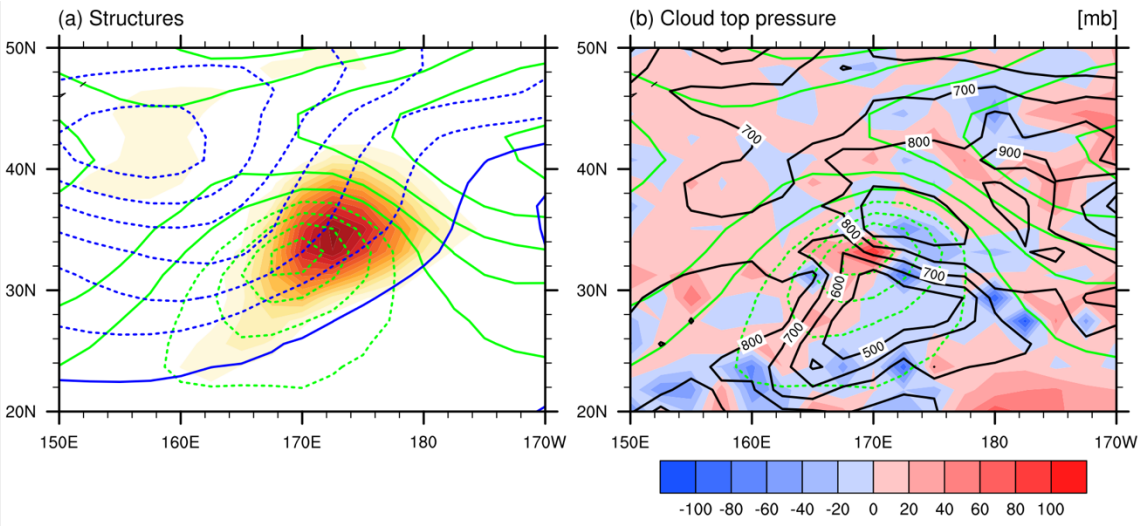

Figure 3.3 (a) Structures of the 1X-EXP in the developing stage averaged over the 6-h period indicated by the green box in Figure 3.2. The blue contours are the geopotential height anomaly at 500 mb (m). The shading shows the vertically averaged total cloud water path. (b) Cloud-top pressure of 1X-EXP (black contours) and the difference between 5X- EXP and 1X-EXP (shading). The green contours in (a) and (b) are the perturbation surface pressure (mb).

hence the further deepening of the surface low and the growth of the cyclone. The local maximum of the total cloud water path is found to the northeast of the storm center where the warm moist air rises ahead of the surface warm front forming stratiform clouds. This local maximum also extends southwestward forming a northeast–southwest–oriented line that corresponds to convective clouds ahead of the surface cold front.

Figure 3.3b plots the cloud-top pressure, a conventional measure of the strength of convection. Black contours are for 1X-EXP, and the color shading is the difference between 5X-EXP and 1X-EXP. The local minimum of this field in the 1X-EXP is located southeast of the surface low, indicating convective clouds ahead of the surface cold front. Despite the weakened growth of the cyclone as a result of increased aerosol concentrations (Figure 3.2), negative anomalies dominate the region of convective clouds in Figure 3.3b, suggesting enhanced convection ahead of the cold front. This is consistent with the "convection invigoration" effect of aerosols discussed in earlier studies where it has been argued that more aerosols in convection increase the cloud droplet number concentration, reduce the precipitation efficiency, cause more droplets to rise above the freezing level, and form more ice, thus releasing more latent heat that enhances the convection (Andreae et al. 2004; Rosenfeld et al. 2008).

The contrast seen here between the enhanced convection and the weakened growth of the cyclone further highlights the differences between a tropical and an extratropical cyclone. While the strength of the eyewall convection in a tropical cyclone is likely positively correlated with the strength of the cyclone (measured in terms of its minimum surface pressure and/or sustained surface wind speed), the overall strength of an extratropical cyclone (measured in terms of its minimum surface pressure or mid-

tropospheric height anomaly) does not necessarily have a direct link with the intensity of localized convection within the cyclone. To understand how increased aerosol concentrations led to stronger convection yet weakened the growth of the cyclone, we next examine changes in both the diabatic heating and the dry dynamical processes (thermal advection) as a result of increased aerosol concentrations from 1X-EXP to 5X-EXP.

3.4 **Change of Lower-Tropospheric Temperature Tendency**

Cold and warm temperature advections in a cyclone are directly tied to the conversion of the background available potential energy to the disturbance potential energy and therefore the intensification of the cyclone. Examining the change of temperature tendency from 1X-EXP to 5X-EXP and the distribution of these changes with respect to the trough–ridge pattern helps to explain the change of the intensity of the cyclone in terms of the magnitude of its associated geopotential height anomalies in the lower-to-middle troposphere. Figure 3.4 shows the vertically averaged temperature tendency in the unit of kelvin per day for three atmospheric layers each bounded by two isobaric surfaces—namely, 1000–700, 1000–500, and 1000–300 mb. The black contours are the total temperature tendency for 1X-EXP, and color shading shows the difference between 5X-EXP and 1X-EXP. The yellow contours are the corresponding differences of the geopotential height at the top of each atmospheric layer (i.e., 700, 500, and 300mb). In 1X-EXP, the dipole pattern of cooling–warming (black contours) is clearly visible in all three atmospheric layers. The cooling is located roughly underneath the trough of the top isobaric level of each layer, indicating further deepening of the trough and thus the strengthening of the cyclone during the period under consideration. The warming is located ahead of the

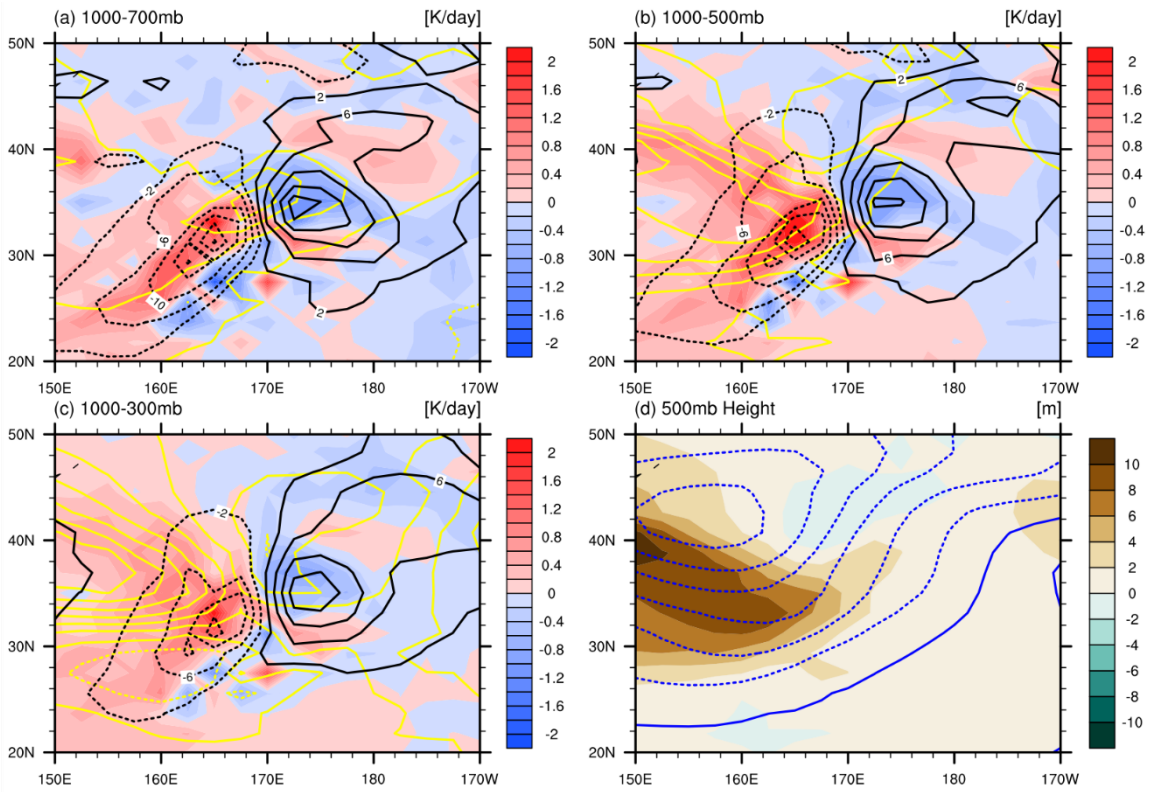

Figure 3.4 Total tendency of temperature averaged vertically from 1000 to (a) 700, (b) 500, and (c) 300 mb for 1X-EXP (black contours) and the differences between 5X-EXP and 1X-EXP (shading). The yellow contours show the differences of geopotential height (m; 5X-EXP minus 1X-EXP) at the level of (a) 700, (b) 500, and (c) 300 mb, separately. (d) The 500-mb height for 1X-EXP (blue contours) and the difference (shading).

trough, contributing to a weak ridge buildup there. Increasing aerosol concentrations lead to a dipole of temperature tendency anomaly (color shading) with signs opposite to the total temperature tendency seen in 1X-EXP for all three atmospheric layers (Figures 3.4a–c).

This opposing effect on the original temperature tendency directly explains why the cyclone shows weakened growth when the level of aerosol concentration is raised. Focusing on the 500-mb level, we see that the reduced cooling tendency underneath the

trough (color shading in Figure 3.4b) is responsible for the generation of the significant positive height anomalies (color shading in Figure 3.4d) near the base of the trough and therefore reduces the rate of trough deepening and cyclone intensification.

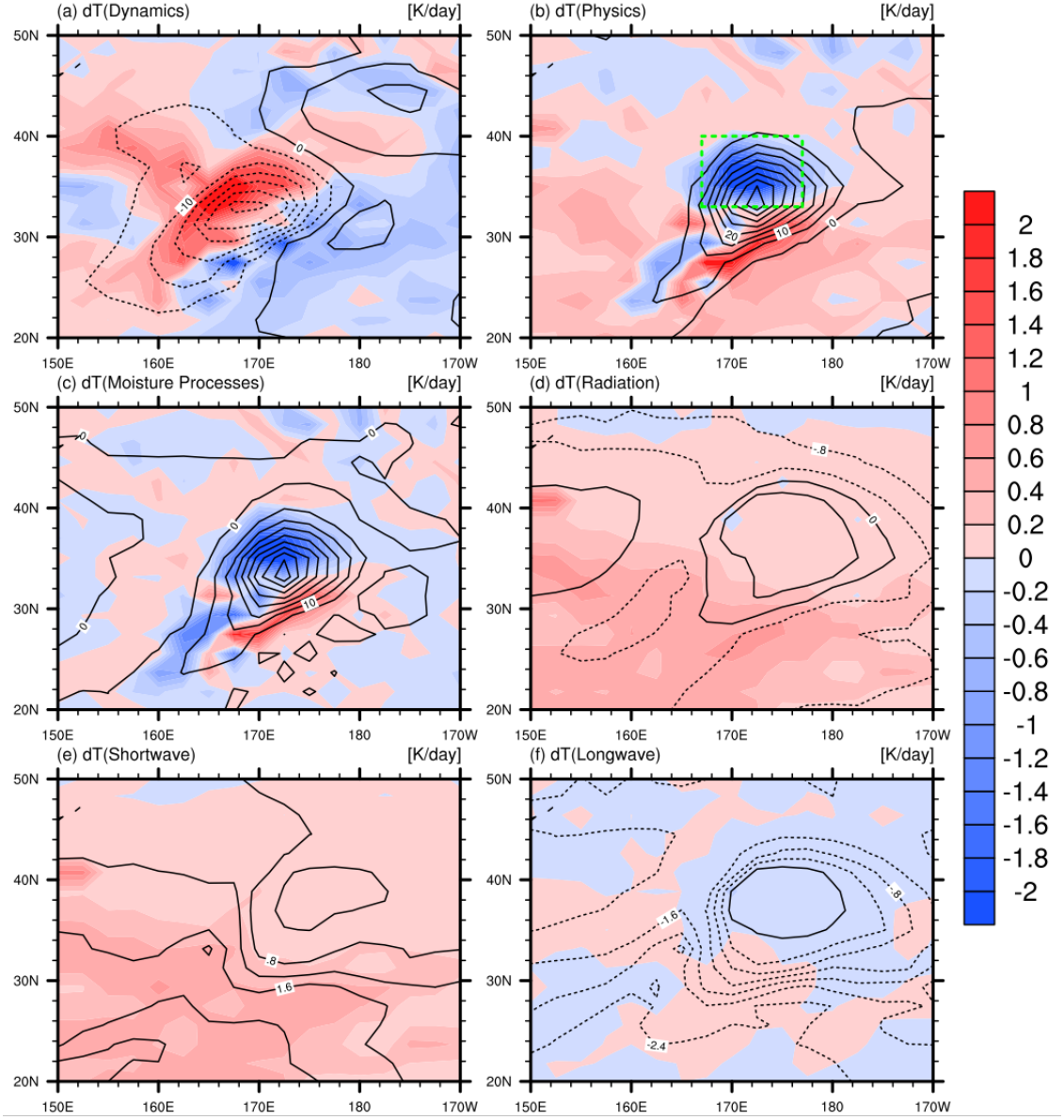

Figure 3.5 Temperature tendency of 1X-EXP (black contours) and the differences between 5X-EXP and 1X-EXP (shading) averaged from 1000 to 500 mb resulting from (a) dynamical processes, (b) physical processes, (c) moist processes, (d) radiative processes, (e) shortwave radiation, and (f) longwave radiation. The green box in (b) will be used to calculate the vertical profiles shown in Figures 3.7, 3.8, and 3.9.

The two major contributors of the total temperature tendency in the model are dynamical and physical processes, and the latter can be further divided into moist and radiative processes (including shortwave and longwave radiative heating). Figure 3.5 shows the decomposition of the total temperature tendency into these components for the 1000–500-mb layer. Again, contours are for 1X-EXP, and color shading indicates the difference between 5X-EXP and 1X-EXP. From Figure 3.5a, it is clear that dynamical processes (thermal advection) serve as the main contributor to the cooling tendency under the trough while physical processes play a key role in generating the warming tendency ahead of the trough (Figure 3.5b). The heating due to physical processes is dominated by moist processes (Figure 3.5c), in particular condensational heating ahead of the surface warm front in the stratiform cloud region. Contributions from radiative heating (Figure 3.5d) are relatively weak yet consistently positive with respect to the dipole of the total temperature tendency (i.e., radiative cooling under the trough and heating ahead of the trough). Radiative cooling is mainly attributed to the longwave radiative effect while heating is collectively contributed by shortwave and longwave radiative effects (Figures 3.5e,f).

In response to increased aerosol concentrations, the ‘‘dynamical cooling’’ and ‘‘physical warming’’ constituting the dipole of the temperature tendency are both weakened (color shading in Figure 3.5a,b). In other words, the dynamical processes (thermal advection) produces less cooling under the trough while physical (moist) processes release less amount of latent heat over the stratiform cloud region (Figure 3.5c). It is interesting to note that latent heating is enhanced instead of weakened in the southwest–northeast-oriented convection zone ahead of the surface cold front, consistent

with the intensified convection found earlier (Figure 3.3b). The shortwave radiative heating is enhanced throughout the model domain (Figure 3.5e) and dictates the overall response of the radiative heating to aerosol changes (Figure 3.5d).

Figure 3.6 presents a schematic diagram that summarizes aerosol-induced changes in these key heating components with respect to the location of a mid-tropospheric (i.e., 500mb) trough (green dashed line) and ridge (green solid line). The solid (dashed) ellipses indicate the aerosol-induced positive (negative) anomalies of temperature tendency.

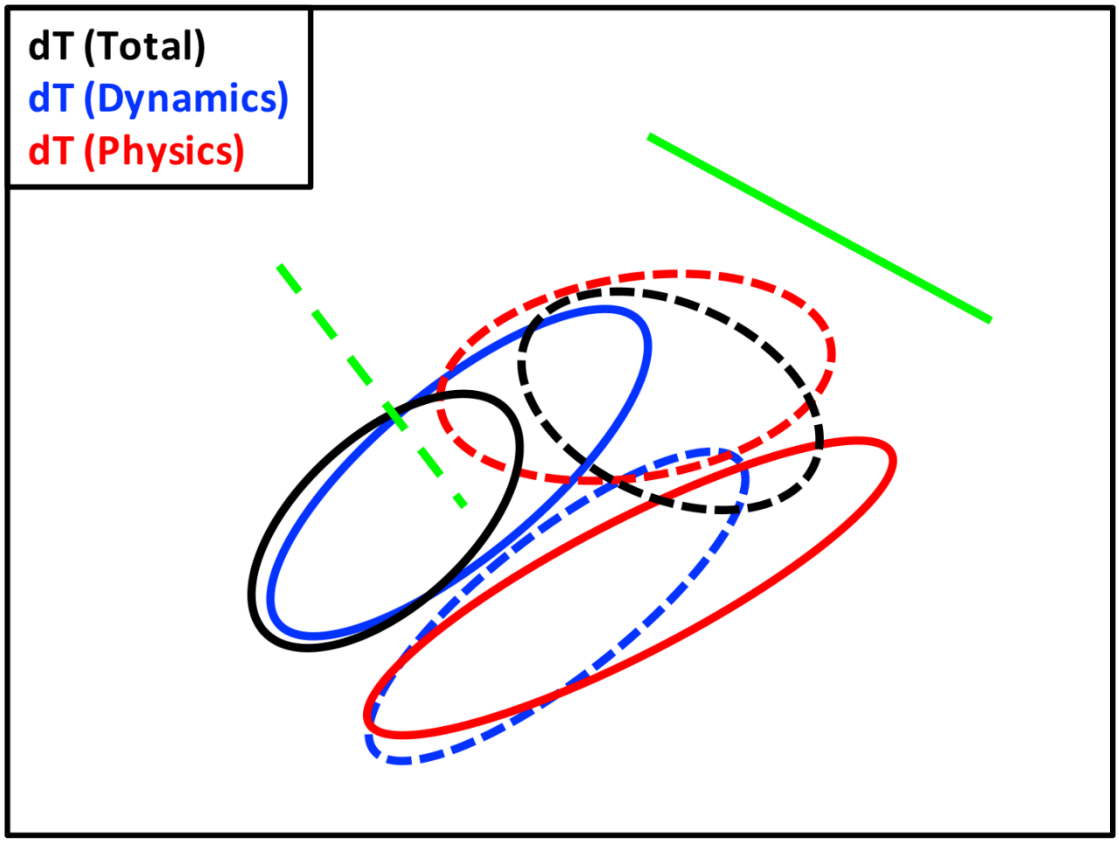

Figure 3.6 Schematic plot of the horizontal temperature tendency differences resulting from total processes (black), dynamical processes (blue), and physical processes (red). Solid (dashed) ellipses indicate aerosol-induced positive (negative) temperature tendency anomalies. The positions of mid-tropospheric (i.e., 500 mb) trough and ridge are indicated by the green dashed and solid lines, respectively.

Contributions from dynamical processes, physical processes, and their sum are plotted in blue, red, and black, respectively. As an idealized version of Figures 3.5a and 3.5b, Figure 3.6 shows that the positive node in the dipole structure of the aerosol-induced heating anomaly is mainly related to dynamical processes (thermal advection) while the negative node is directly tied to physical (moist) processes. In the southeast quadrant of the cyclone (ahead of the surface cold front), enhanced convection is reflected by positive latent heating anomalies, which are largely canceled out by negative heating anomalies driven by dynamical processes. The dynamically driven positive heating anomaly underneath the trough (solid blue ellipse) is the essential component that causes weakened growth of the cyclone when aerosol concentrations are increased. The physically driven cooling anomalies ahead of the trough (dashed red ellipse) also contribute mildly to the weakened growth of the cyclone by suppressing ridge building ahead of the trough. Next we will focus our analysis on this dipole of heating anomalies and find out the exact processes responsible for its formation.

3.4.1 Cooling Anomaly Associated Physical Processes

We first plot in Figures 3.7 and 3.8 the vertical profiles of wind and physically driven temperature tendencies, respectively, averaged over the stratiform cloud region (green box in Figure 3.5b) where the aerosol-induced negative heating (temperature tendency) anomaly is most pronounced. In Figure 3.7, black solid curves are for the zonal U, meridional V, and vertical ω component of the wind in 1X-EXP, and red dashed curves correspond to the differences between 5X-EXP and 1X-EXP. The change of zonal wind is very small (Figure 3.7a), while the meridional wind anomaly is generally negative with the

maximum decrease of about 7% found at 850 mb. The vertical velocity peaks at 550mb in 1X-EXP and weakens about 5% in 5X-EXP.

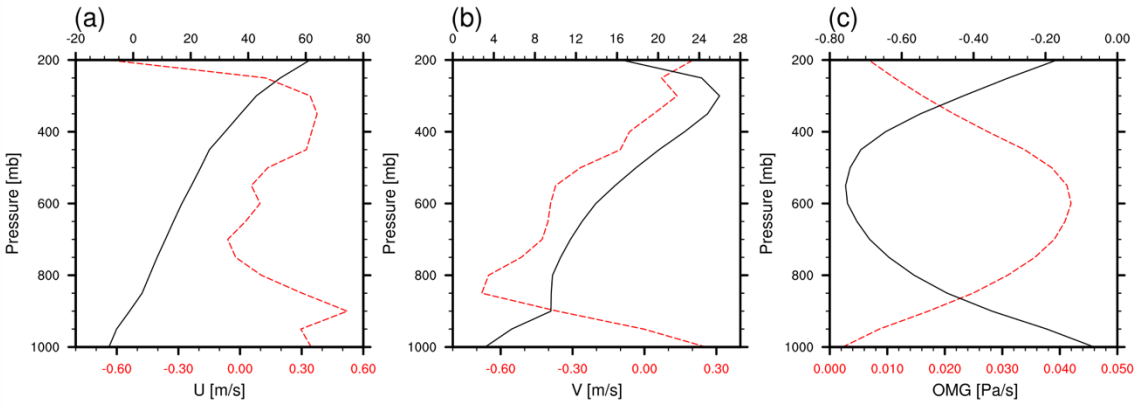

Figure 3.8 Vertical wind profiles of (a) U, (b) V, and (c) ω averaged over the area indicated by the green rectangle in Figure 3.5b. The black solid curves are for 1X-EXP, and the red dashed curves are the differences (5X-EXP minus 1X-EXP).

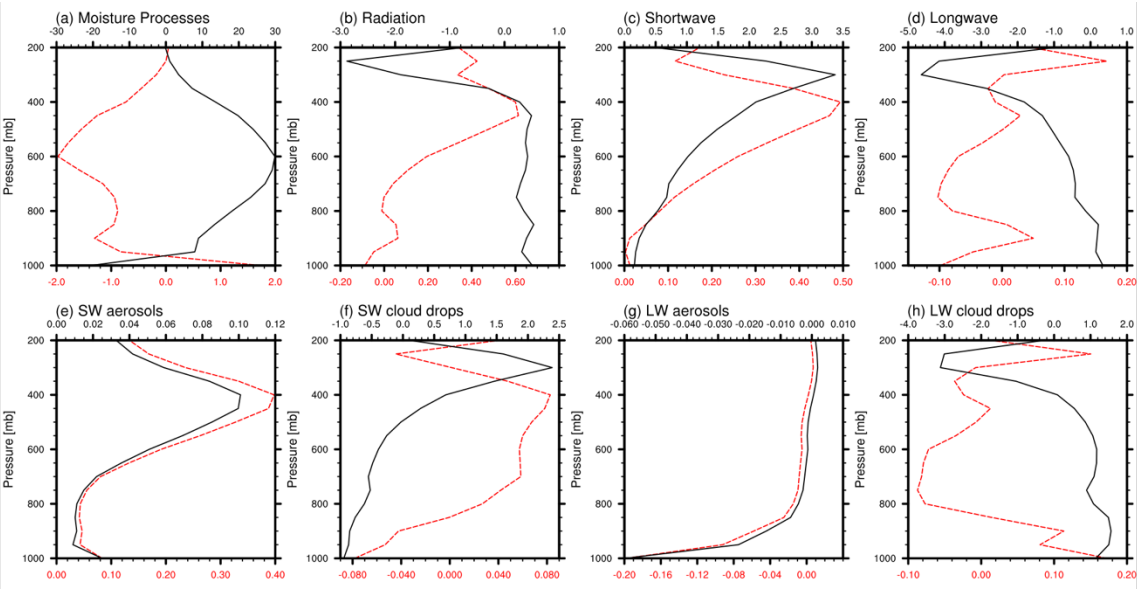

Figure 3.7 As in Figure 3.7, but for the temperature tendency ($K\ day^{-1}$) resulting from (a) moist processes, (b) radiative processes, (c) shortwave radiation, (d) longwave radiation, (e) shortwave radiation due to aerosols (direct effect), (f) shortwave radiation due to cloud drops (indirect effect), (g) longwave radiation due to aerosols (direct effect), and (h) longwave radiation due to cloud drops (indirect effect).

Figure 3.8 shows the vertical profiles of temperature tendencies (heating rates) associated with various physical processes (black solid curves are for 1X-EXP and red dashed curves correspond to differences between 5X-EXP and 1X-EXP). Consistent with the findings summarized in Figure 3.6, the negative temperature tendency anomaly ahead of the trough is largely contributed by changes in moisture processes. Suppressed latent heating is clearly seen throughout the large part of the atmosphere with the maximum reduction (~7%) occurring around 600mb (Figure 3.8a). This result also agrees well with the weakening of the large-scale ascent ahead of the warm front (Figure 3.7c).

Changes in radiative heating generally oppose the effect of changes in the latent heating with weak positive anomalies peaking around 400mb (Figure 3.8b), and these positive anomalies mainly stem from the shortwave radiation (Figures 3.8c,d). Figures 3.8e and 3.8f display the direct and indirect effects of aerosols on the temperature tendency with the indirect effects here approximated by changes in cloud radiative heating (see section 2 for details). Specifically, Figures 3.8e and 3.8g show the direct shortwave and longwave radiative effects of aerosols, respectively, and Figures 3.8f and 3.8h show the first indirect shortwave and longwave radiative effects of aerosols, respectively. For the shortwave radiative heating, although the contribution of clouds is more substantial than that of aerosols in 1X-EXP (black curve), the heating anomaly (red curve) is actually dominated by the aerosol direct effect (Figure 3.8c vs 3.8e vs 3.8f). This means that increasing aerosol concentrations in the model greatly enhances the shortwave absorption by aerosols. The change of the longwave radiative heating is largely determined by the indirect effect of aerosols that reduces longwave radiative cooling around 250 mb and enhances longwave radiative cooling in the lower troposphere between 800 and 600 mb in 5X-EXP.

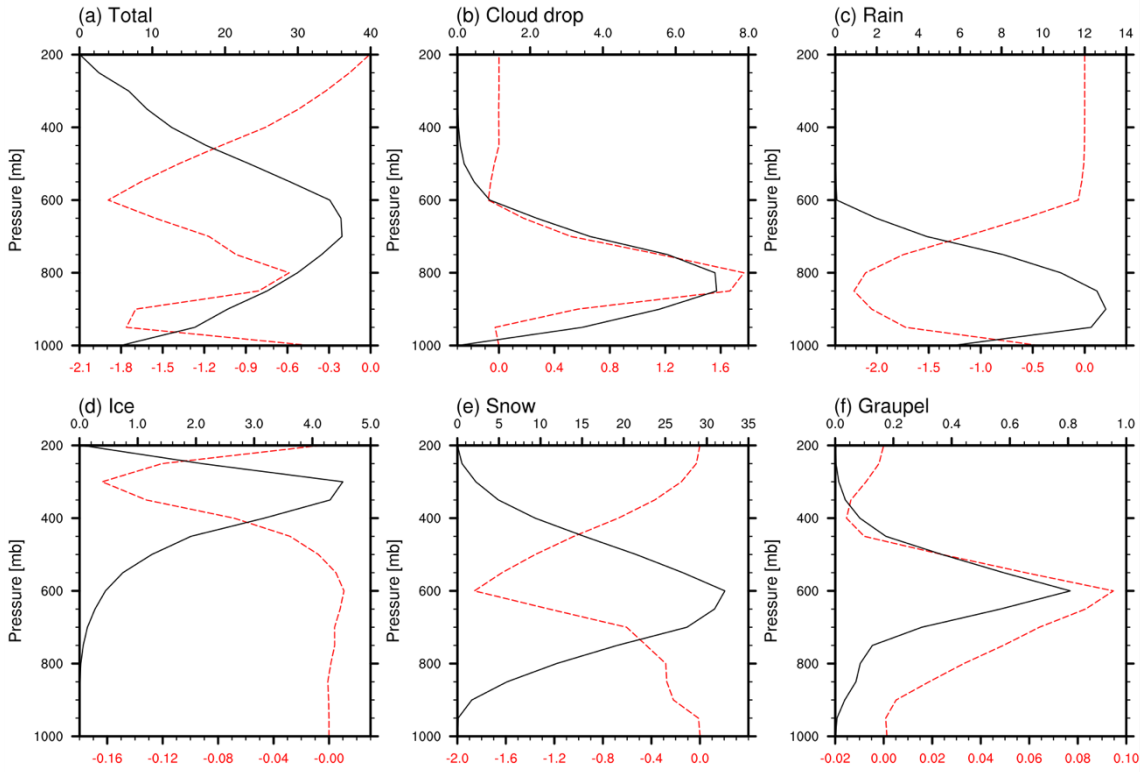

Figure 3.9 As in Figure 3.7, but for the mass mixing ratio ($10^{-2}\ g\ kg^{-1}$) for (a) total water (the sum of the following five hydrometeors), (b) cloud drops, (c) rain, (d) ice, (e) snow, and (f) graupel.

Figure 3.9 shows the corresponding vertical profiles of various hydrometeors. The mass mixing ratio of total cloud water, including all five hydrometeors, has a maximum value at 700 mb (Figure 3.9a) and is largely contributed by snow (Figure 3.9e). The liquid water (cloud drops and rain) is concentrated at about 850 mb (Figures 3.9b and 3.9c) and ice crystals peak at about 300 mb (Figure 3.9d). The drop of ice crystals in 5X-EXP explains the aerosol indirect effect in longwave radiation (Figure 3.8h) where radiative cooling at this level decreases about 5%. At the lower levels, the amount of cloud drops increases while the amount of rain decreases, indicating that the increased aerosols hinder the formation of precipitation and reduce precipitation efficiency. Graupel shows a slight

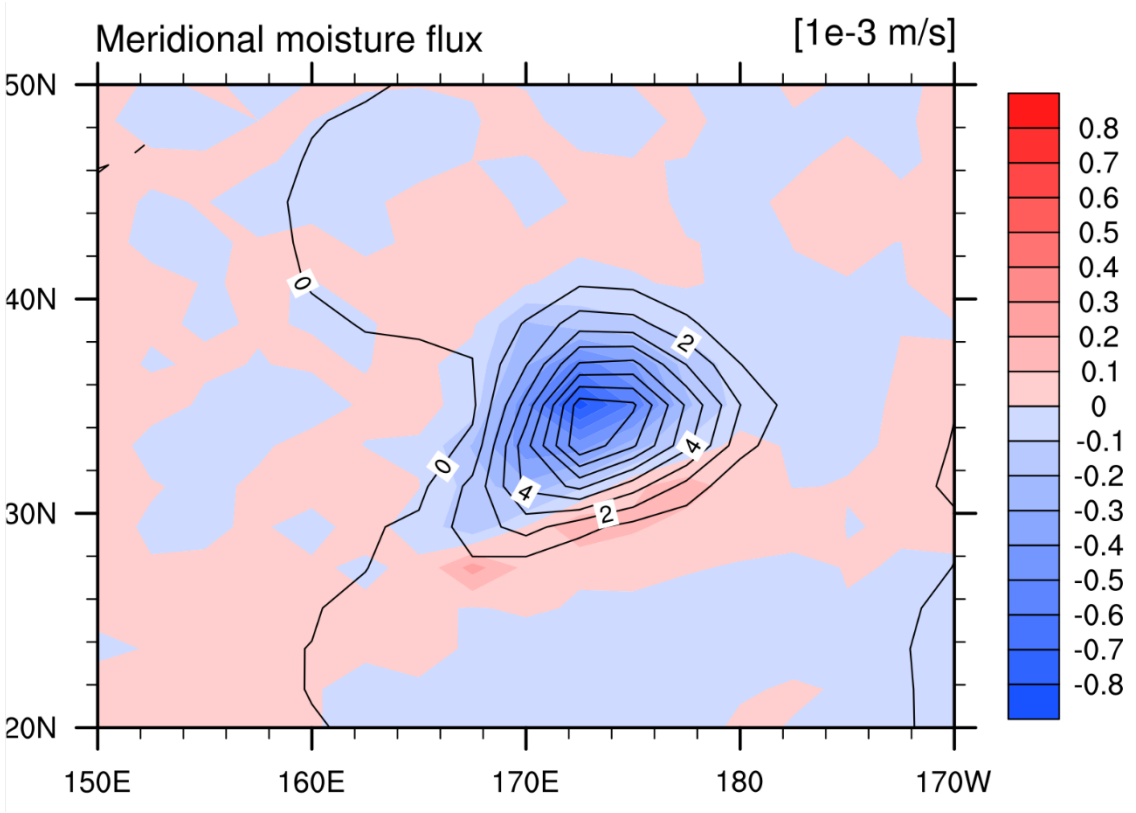

Figure 3.10 Meridional flux of total water for 1X-EXP (black contours) and differences (shading). The meridional moisture flux is defined as the product of meridional wind ($m\ s^{-1}$) and total water mixing ratio ($g\ g^{-1}$).

increase around the 600-mb level. The decrease of the total cloud water of hydrometeors throughout the troposphere (Figure 3.9a; thus suppressed latent heating) is mainly contributed by a decrease of snow water around 600mb and a drop of rainwater underneath 800 mb.

To trace the origin of the decrease of total water in the stratiform cloud region, we compute the meridional transport of moisture and plot both the 1X-EXP results (black contours) and differences between 5X-EXP and 1X-EXP (color shading) in Figure 3.10. As a result of increased aerosol concentrations, the northward transport of moisture ahead

of the warm front is significantly reduced in 5X-EXP. This reduction, together with the anomalously strengthened transport south of the stratiform cloud region, leads to the anomalous convergence of moisture in the southwest–northeast–oriented convective band ahead of the surface cold front, which is consistent with the enhanced convection found previously (Figure 3.3b). In other words, increased aerosol loading in the atmosphere invigorates deep convection ahead of the cold front, and the intensified convection consumes more moisture and reduces moisture supply for hydrometeor formation ahead of the warm front, ultimately causing the suppressed latent heating seen in Figure 3.5c. This aerosol-induced latent heating change modifies relevant dynamical processes directly tied to the growth rate of the cyclone, which will be discussed next.

3.4.2 Heating Anomaly Associated Dynamical Processes

To delineate the processes responsible for the positive heating anomaly (i.e., positive temperature tendency anomaly) found underneath the trough (Figure 3.5a), we show in Figure 3.11 various components of the three-dimensional advection of potential temperature averaged from 1000 to 500mb. Figures 3.11a–c display the zonal, meridional, and vertical wind, and Figures 3.11d–f show the temperature advection associated with each wind component. Figures 3.11g–i show the potential temperature and the horizontal (2D) and total (3D) advection of potential temperature.

The first thing to note is that in 1X-EXP, the cold horizontal advection to the west of the cyclone center (Figure 3.11h) is contributed by both its zonal (Figure 3.11d) and meridional component (Figure 3.11e), while the warm horizontal advection to the east of the cyclone center (Figure 3.11h) is largely caused by the southerly driven advection

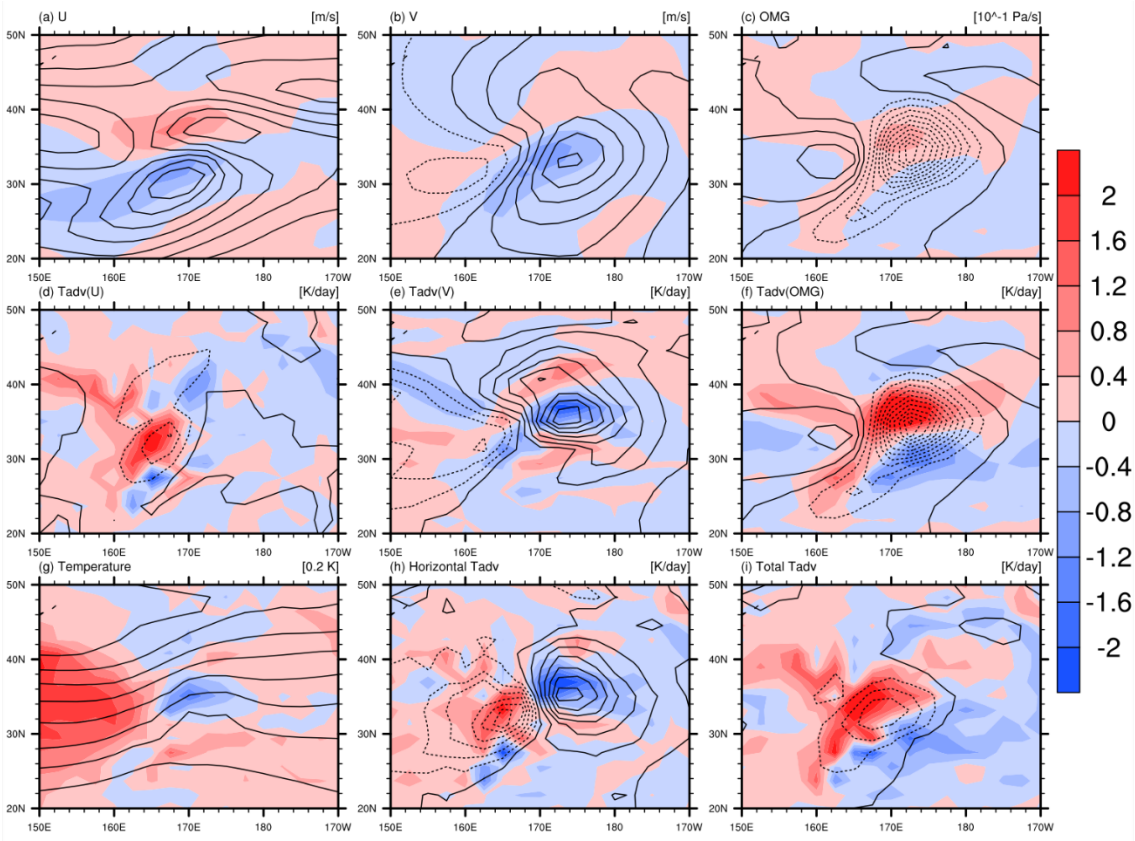

Figure 3.11 Analysis of temperature advection averaged from 1000 to 500 mb. The black contours show the 1X-EXP, and the color shading shows the differences. The wind components are shown for (a) U, (b) V, and (c)ω. The advections of potential temperature are shown in the (d) x, (e) y, and (f) z directions. Also shown are the (g) potential temperature, (h) horizontal (2D) advection, and (i) total (3D) advection of potential temperature. The contour intervals for each panel are (a) $4\,m\,s^{-1}$, (b) $4\,m\,s^{-1}$, (c) $0.1\,Pa\,s^{-1}$, (d) $10\,K\,day^{-1}$, (e) $4\,K\,day^{-1}$, (f) $5\,K\,day^{-1}$, (g) $4\,K$, (h) $5\,K\,day^{-1}$, and (i) $10\,K\,day^{-1}$.

(Figure 3.11e). As aerosol concentrations increase, the decrease of latent heating ahead of the warm front discussed in the previous section creates an anomalous cold spot in the temperature field centered about $35^oN, 170^oE$ (Figure 3.11g). The presence of this cold spot decreases the zonal temperature gradient to its west and meridional temperature gradient to its north. Together with weakened westerlies (Figure 3.11a), the reduced zonal temperature gradient weakens zonal cold advection to the west of the cold spot, leading to

a positive, dynamically driven temperature tendency anomaly there. In a similar way, the weakened meridional temperature gradient and southerlies (Figure 3.11b) reduce warm advection north of the cold spot leading to a negative, dynamically driven temperature tendency anomaly there. The creation of this dipole pattern anomaly of temperature tendency (color shading in Figure 3.11h) reduces the rate of growth of the cyclone mainly because the weakening of the cold advection underneath the 500-mb trough effectively slows down the deepening of the trough. As the cyclone growth rate is hindered, large-scale ascent ahead of the trough weakens (positive ω anomaly in Figure 3.11c), and this causes less low-potential-temperature air to be advected upward creating a positive anomaly in the vertical advection. The negative temperature tendency associated with the meridional advection is largely canceled out by the positive anomaly as a result of the vertical advection, leaving a distinct, dynamically driven positive temperature tendency anomaly to the west and northwest of the cyclone center (Figure 3.11i). The 3D advection difference between 5X-EXP and 1X-EXP shown in Figure 3.11i effectively recovers the total temperature tendency anomaly driven by dynamical processes given in Figure 3.5a.

3.5 **Section Summary**

The impacts of environmental aerosols on the growth of an extratropical cyclone in a realistic winter flow setting are investigated using a superparameterized global model (SP-CAM) where cloud-scale dynamics and thermodynamics are explicitly resolved. An examination of the results from 13 ensemble pairs suggests that the growth of the cyclone is temporarily suppressed as a result of increased aerosol concentrations in the model. A *convection–advection–moisture self-adjustment (CAMS) mechanism* of aerosol–cyclone

interaction emerges as we focus our analysis on this transient period of suppressed growth. Specifically, an increase of environmental aerosols invigorates deep convection ahead of the surface cold front in the southeast quadrant of a developing extratropical cyclone. The enhanced convection consumes more moisture and suppresses northward moisture transport into the stratiform cloud region ahead of the cyclone (northeast quadrant) and effectively reduces mass mixing ratio of hydrometeors and latent heating in that region. The reduced latent heating creates a cold spot that weakens zonal temperature to its west and meridional temperature gradient to its north and leads to suppressed horizontal cold advection underneath the mid-tropospheric trough. The suppressed cold advection reduces the rate of trough deepening and thus the rate of cyclone intensification. The weakened growth of the cyclone naturally causes reduced southerly wind speed in the southeast quadrant and subsequently the transport of moisture northward that feeds both convection bands ahead of the cold front and stratiform precipitation ahead of the warm front. With decreasing moisture supply, the invigoration effect of aerosols on deep convection eventually diminishes as does the resultant weakening of cold advection and suppression of cyclone growth. This CAMS mechanism thus explains why the aerosol effect on the cyclone development is negative while being "transient" despite the sustained high level of aerosol concentrations in the model.

It is interesting to note that in Chapter 2, an idealized baroclinic wave (cyclone) in the WRF Model experiences a transient period of intensified (instead of weakened) growth when cloud droplet number concentrations were raised as a simplified way of representing aerosol microphysical effects. This discrepancy largely stems from the different level of aerosol–circulation coupling in the standard WRF Model and in the SP-CAM. In the WRF

Model used in Chapter 2, the aerosol microphysical effect is not considered for the development of deep convection because of the use of cumulus parameterization. This effectively eliminates the "convection invigoration" component of the CAMS mechanism, and the aerosol effect on latent heating directly applies to the large-scale ascent ahead of the warm front in a way similar to the convection invigoration discussed in this paper, thus creating a result seemingly opposite to what is reported here. Other possible contributions to the differences between findings from this chapter and Chapter 2 include the facts that 1) cyclones evolve and interact with surrounding disturbances in a realistic flow in the current model setting compared to a zonally periodic domain in the WRF Model and 2) a homogenous lower boundary condition is used, which has a tendency to speed up the growth of the cyclone.

The CAMS mechanism proposed here clearly suggests the importance of incorporating aerosol microphysical effect into convection development in any studies that attempt to evaluate aerosol effects on the growth of extratropical disturbances such as cyclones. Despite the suppression effect of aerosols detected here being transient, we anticipate that such effects will be accumulated over regions with a high level of cyclone activity during winter seasons (e.g., over the oceanic storm tracks) and leave a distinct footprint in the general circulation and surrounding regional climate, particularly downstream of these stormy regions given the major role played by these disturbances in momentum, energy, and moisture transport. Next chapter with the SP-CAM has been targeting this direction.

The work presented in this chapter is published in Journal of Climate (Lu and Deng 2016).

CHAPTER 4

IMPACT OF AEROSOLS ON NORTHERN EXTRATROPICAL ATMOSPHERIC CIRCULATION IN BOREAL WINTER

4.1 Motivation

Chapter 2 and 3 of this dissertation investigate the dynamic and thermodynamical processes of the aerosol effects in a weather-scale disturbance. The coupling between aerosol effects and deep convections is shown to be critical to a developing cyclone. It is known that these extratropical disturbances not only influence day-to-day weather variability but also modulate regional climates through their transports of momentum, heat and moisture, dictating the winter-mean atmospheric circulation. Therefore, it is crucial to understand the collective effects of aerosols on the large-scale extratropical circulation given the fact that East Asia (North Pacific storm track) is occupied by high concentrations of atmospheric aerosols of both natural and anthropogenic origins in wintertime. Zhang et al. (2011) use the National Center for Atmospheric Research (NCAR) Community Climate System Model, version 3 (CCSM3) to study the impacts of Asian aerosol emissions, that finds cooling and a reduction of precipitation over China as well as warming over the United States in the wintertime. By using the Community Earth System Model, Version 1.0.2 (CESM1.0.2), Zhou and Deng (2013) demonstrate that the presence of Asian aerosol emissions has a strong modulation on the Pacific storm track, and affect the precipitation along the west coast of the United States in wintertime. Due to the limitation of cumulus parameterizations used in these two models, coupling between aerosol effects and deep convections cannot be simulated. Wang et al. (2014) is the first study to take into account

the aerosol effects in deep convections in a GCM framework to address the impacts of anthropogenic aerosols on storm tracks. The so-called multiscale modeling framework (MMF) is to embed a cloud resolving model in each grid column to simulate the sub-grid scale cloud processes. Focusing on the Pacific storm track, their analysis indicates the change of cloud properties due to the aerosol invigoration effect, thus leading to the change of radiative forcing and increase of precipitation. However, due to the complex interactions across different scales, the CAMS mechanism, discussed in Chapter 3, shows that the invigorated convection is not always tied to the intensity variation of cyclones.

In this chapter, how the collective effects by aerosols (e.g., aerosol induced diabatic heating change and the consequence of dynamic and thermodynamical pathways) dictate the midlatitude circulations will be discussed. In Section 4.2, the experiment design is presented. The response in eddy activities is discussed in Section 4.3, and the feedback to the mean flow in Section 4.4. Section 4.5 provides some concluding remarks and the directions for future studies.

4.2 **Data and Methods**

4.2.1 Experiment Design and Model Setup

The Superparameterized Community Atmosphere Model (SP-CAM) is chosen for this study because of its ability to simulate the coupling between aerosol effects and deep convections, as well as to reproduce a realistic Northern Hemisphere wintertime circulation. SP-CAM is a multiscale modeling framework (MMF) model that combines the Community Atmosphere Model, version 5.2 (CAM5) with a cloud resolving model named the System for Atmospheric Modeling (SAM; Khairoutdinov and Randall 2003). By

replacing the conventional cumulus parameterization with SAM, SP-CAM allows a more physical treatment of aerosol-cloud interactions. A detailed description of the SP-CAM can be found in Section 3.2.1, as well as Wang et al. (2011a).

To obtain a robust dynamic footprint left by aerosols in the extratropics, the "perpetual winter" runs are adopted to efficiently and effectively conduct long-term simulations of winter circulation in a clean and controllable manner. The model resolution is 1.9^{o} x 2.5^{o} with 30 vertical levels. The model is first spin-up for 365 days with the boundary forcings (e.g., sea surface temperature, sea ice and land surface parameters) fixed to the climatological values in January. The solar radiative forcing is set to the value on January 1^{st} with diurnal cycle. Then a pair of 2000-day simulations is conducted with the same fixed boundary conditions except for different aerosol emission scenarios. Two aerosol emission scenarios are chosen from IPCC AR5 (Lamarque et al. 2010; van Vuuren et al. 2010) with the values in January 1850 and January 2010 and referred to as the preindustrial (PI) and present-day (PD) experiments. The only change of the model setting between PI and PD is the prescribed aerosol emissions, so the differences in the sample of 2000 days (about 67 winter months or 22 winter seasons) are treated as the results from the extra aerosol forcing.

4.2.2 Aerosol Emissions and its Distribution

The SP-CAM uses MAM3 scheme (Liu et al. 2012) to treat aerosols in three lognormal modes: Aitken, accumulation and coarse modes. The scheme can predict aerosol mass and number mixing ratio with predetermined widths of each distribution, while also covering the aerosol processes including chemistry, nucleation, condensation, coagulation,

transport, activation and deposition. The aerosol species include sulfate, black carbon, dust, sea salt, primary organic matters (POM) and secondary organic aerosols (SOA). The explicit cloud-parameterized-pollutant (ECPP) approach (Gustafson et al. 2008) uses the statistics of cloud properties to drive the cloud-related aerosols and trace gas process, which is in a more physical manner than the conventional treatment in CAM5. Comparing to the conventional GCMs, the SP-CAM, which uses the MMF, can better resolve the aerosol direct and indirect effects, especially the coupling between aerosols and deep convections, which is proved to be crucial in regard to the cyclone activities (Lu and Deng 2016).

Because the PI and PD experiments are different in the prescribed aerosol emissions, all the model chemical and microphysical processes, as well as the interactions with clouds and circulations will contribute to the variation of aerosol distributions. The time-mean of

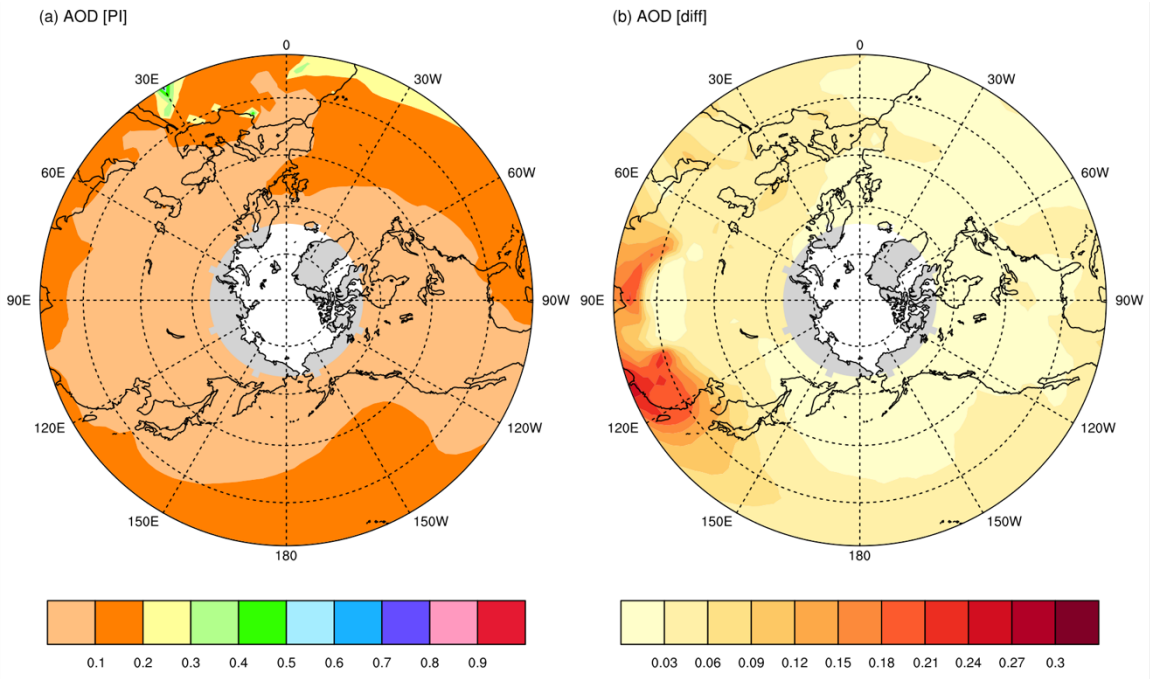

Figure 4.1 Time-mean aerosol optical depth at 400 nm wavelength for the (a) PI and (b) anomaly (PD minus PI).

aerosol revolution serves a better way than the distribution of aerosol emissions to understand the geographical effects of aerosol forcing. Figure 4.1 shows the aerosol optical depth (AOD) averaged over the entire simulation period (2000 days). The figure focuses on the Northern Hemisphere, cropped starting from $20\,°N$. The extratropics will be the major area discussed in this study. The blank data over the polar region results from the lack of solar radiation due to the solar zenith angle being fixed to the values in the wintertime. Figure 4.1a reveals an overall clean environment ($AOD < 0.2$) in the PI emission scenario, where the AOD over central Africa, near the equator, reaches 0.8 due to the present of atmospheric dust (not shown for brevity). Figure 4.1b shows the general increase of AOD in the PD emission scenario over the entire Northern Hemisphere. The significant increase of aerosol loading can be found extending from South Asia to East Asia, following the circulation transporting toward the east over the western Pacific. The area with the marked increase of AOD (defined as between $60\,°\text{E} - 150\,°\text{E}$ and $20\,°\text{N} - 45\,°\text{N}$) is selected to examine the vertical distribution of aerosol concentrations as shown in Figure 4.2.

The black curves are for the PI run, and the red for PD run. The total mass mixing ratio of aerosols (Figure 4.2a) increases about 30 to 40 unit ($1\ unit = 10^{-4}\ ug\ kg^{-1}$) in the lower troposphere in the PD experiment, which is equivalent to about 20% to 40% change comparing to the "clean" environment in the PI experiment. The biggest contributor to the increase is sulfate (Figure 4.2b), resulting from the blooming of human activities and industrial emissions. An increase of sulfate has the potential impacts on the warm rain processes and precipitation by acting as CCN through the microphysical processes (Wang et al. 2014). Although the increase in mass mixing ratio for black carbon in Figure 4.2c is

not as much as that of sulfate, the change in percentage is about the same. The change of black carbon in the lower troposphere can be up to eightfold in the PD run compared to the PI run. The decrease of dust (from natural sources) below 750 hPa and slightly increase in the higher level reveal a more intense vertical transportation by the circulations (Figure 4.2d). Sea salt (Figure 4.2e) is relatively unchanged between PI and PD experiments. The concentrations of POM and SOA (Figures 4.2f, g) are also generally rising across South and East Asia.

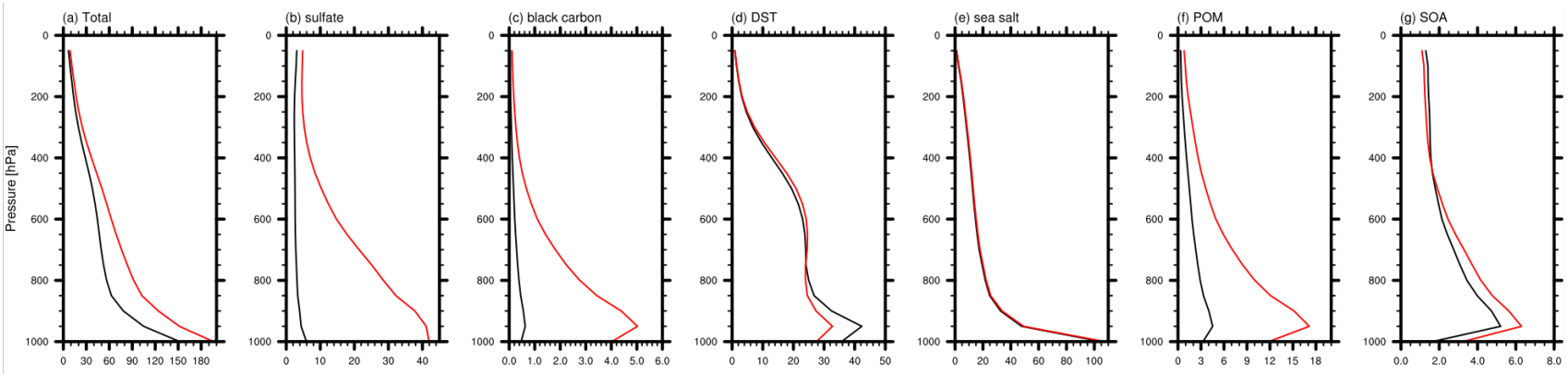

Figure 4.2 Vertical distribution of aerosol concentrations for (a) total aerosols, (b) sulfate, (c) black carbon, (d) dust, (e) sea salt, (f) primary organic matter and (g) secondary organic aerosol. Black color is PI, and red color is PD. The unit is $10^{-10}\ kg/kg$.

4.3 Change in the Local Energetics of Extratropical Disturbances

To examine the change of transient eddies (disturbances) in response to the aerosol forcing, the local energetics for high-frequency (HF) and low-frequency (LF) eddies are calculated, which are defined as the periods less than 10 days and 10 to 30 days, separately. Although Plumb (1983) pointed out the non-uniqueness of the flux and conversion terms in the local energy budget may sometimes cause misleading, the analyses of the budget terms with keeping the limitations in minds can still provide useful information to the eddy activities and background flows in a certain extent (Chang et al. 2002). Following the previous studies (Orlanski and Katzfey 1991; Jiang et al. 2013), the filtered local energetics equations are derived for HF and LF eddy kinetic energy (EKE), eddy available potential energy (EAPE) and total eddy energy (the sum of EKE and EAPE). The detail derivation is shown in Appendices A, B and C, and the results for the total HF and LF eddy energetics equations are repeated here for convenience of reference.

$$\frac{\partial E_H}{\partial t} = [-V_{3m}\cdot\nabla_3 K_H - \nabla\cdot(\Phi_H V_H) - \mathbf{V}_{3m}\cdot\nabla_3 A_H] - V_H\cdot(V_{3H}\cdot\nabla_3)V_m + \frac{\alpha_m}{\theta_m}\frac{\theta_H \mathbf{V}_H}{d\Theta/dp}\cdot\nabla\theta_m$$
$$+\left[-V_H\cdot\langle V_3'\cdot\nabla_3 V'\rangle^H + \left(\frac{\alpha_m}{\theta_m}\frac{\theta_H}{d\Theta/dp}\right)\langle \mathbf{V}_3'\cdot\nabla_3\theta'\rangle^H\right] - \frac{\alpha_m}{c_p\theta_m}\frac{\theta_H Q_H}{d\Theta/dp}\left(\frac{p_0}{p}\right)^\kappa + diss_H \quad (4\text{-}1)$$

$$\frac{\partial E_L}{\partial t} = [-V_{3m}\cdot\nabla_3 K_L - \nabla\cdot(\Phi_L V_L) - \mathbf{V}_{3m}\cdot\nabla_3 A_L] - V_L\cdot(V_{3L}\cdot\nabla_3)V_m + \frac{\alpha_m}{\theta_m}\frac{\theta_L \mathbf{V}_L}{d\Theta/dp}\cdot\nabla\theta_m$$
$$+\left[-V_L\cdot\langle V_3'\cdot\nabla_3 V'\rangle^L + \left(\frac{\alpha_m}{\theta_m}\frac{\theta_L}{d\Theta/dp}\right)\langle \mathbf{V}_3'\cdot\nabla_3\theta'\rangle^L\right] - \frac{\alpha_m}{c_p\theta_m}\frac{\theta_L Q_L}{d\Theta/dp}\left(\frac{p_0}{p}\right)^\kappa + diss_L \quad (4\text{-}2)$$

where the subscripts "H", "L" and "m" stand for HF, LF and time-mean, separately. The *E* is total eddy energy, *K* the EKE and *A* the EAPE. All the other notations are defined in the Appendices A, B and C. The first three terms in the square bracket on the right-hand side (RHS) are the advections of energy (ADV). The fourth term is the conversion of

kinetic energy between mean-flow and eddies (barotropic conversion; BT). The fifth term is the conversion of available potential energy between mean-flow and eddies (baroclinic conversion; BC). The next two terms in the second square brackets are named the cross-frequency eddy-eddy interactions (CFEI), which only exist in the filtered energy budgets indicating the conversion of eddy energy across different frequencies. The last two terms are contributions from diabatic processes and dissipation (DISS). It is worth noting that the BT and DISS terms come from the EKE equation, where the latter is obtained as the residual assuming the steady state (i.e., $\frac{\partial \mathrm{K}}{\partial \mathrm{t}} = 0$). The BC and diabatic terms come from the EAPE equation, and the ADV and CFEI terms are mixed from both (EKE and EAPE).

First we show the column-integrated, time-averaged total energy for HF and LF eddies in Figures 4.3. The HF total eddy energy in the PI experiment (Figure 4.3a) is characterized by active weather disturbances along the midlatitudes forming the Pacific and Atlantic storm tracks. The Pacific storm track extends from the east to the Japan, maximizes at the central Pacific $(180\,°W - 150\,°W)$ and reaches the west coast of the United States. The Atlantic storm track appears to be stronger and narrower (more zonally oriented), starting from Central America across the entire Atlantic basin. It appears a linkage between two major storm tracks (around $120\,°W$) may result from the energy dispersion and downstream development east to the exit region of Pacific storm track. For the LF eddies shown in Figure 4.3c, the maximum locates at the Gulf of Alaska with a second maximum south of Iceland, associated with the blockings or persistent anomalies (Dole and Black 1990). The right two panels (Figures 4.3b, d) show the change of total eddy energy in response to the aerosol forcing (PD minus PI) with the dots highlighting the statistically significant level of 95%. Both the Pacific and Atlantic storm tracks are

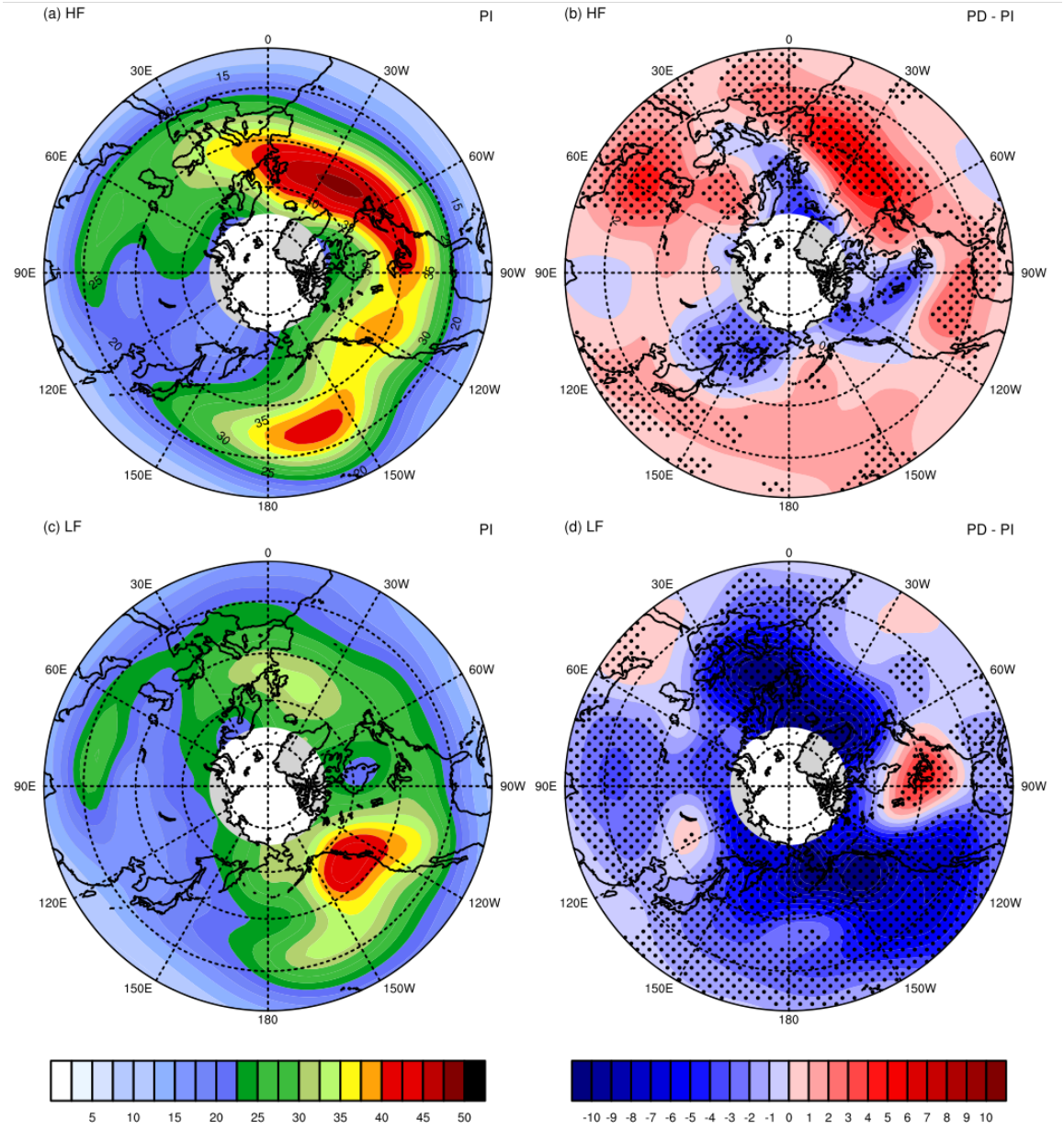

Figure 4.3 Vertically integrated, time-mean total eddy energy with the unit in $m^2\ s^{-2}$ for (a) HF eddies in PI, (b) HF anomaly (PD minus PI), (c) LF eddies in PI and (d) LF anomaly. The dots indicate the 95% level of statistical significance based on Student's t-test (without same population variance assumption, or so-called Welsh's t-test).

enhanced in terms of HF eddy activities while the activities of the LF eddies decrease markedly. Specifically for the Pacific storm track, the increase of HF eddy activities over

the entrance region is statistically significant, and the reduction to the north further limits the meridional spread of the movements of eddies. The change of HF eddy activities appears a more consistent enhancement over the United States and Atlantic storm track, accompanied with a slightly shift equatorward of the maximum. The region of increased LF eddy activities over the central United States is surrounded by marked reduction, collocating at the downstream of the reduction in HF eddy activities.

It appears that the responses of HF and LF eddy activities to the aerosol forcing are generally opposite, though attributing directly to the energy conversion from LF to HF is difficult due to the nonlinear interactions between the eddies in different frequencies as well as the mean flow. The analysis of local energetics breaks down different processes and helps to gain more insight on the aerosol impacts through the dynamic and/or thermodynamical pathway. Table 4.1 summarizes the HF and LF total energy budgets averaged over the zonal band from $20\ °N - 70\ °N$. The unit for the total energy is $m^2\ s^{-2}$,

Table 4.1 HF and LF energy budgets averaged horizontally between 20 to 70 ^{o}N and vertically through the atmosphere. The unit for the total energy is $m^2\ s^{-2}$, and for the other budget terms is $m^2\ s^{-2}\ day^{-1}$.

		Total Energy	Budgets					
			ADV	BC	BT	CFEI	DIABATIC	DISS
HF	PI	47.38	-4.03	12.18	-1.84	0.34	3.94	-9.33
	PD – PI	0.79	-0.28	0.65	-0.20	-0.49	0.16	0.05
	Change in %	1.7	6.9	5.3	11.1	-144.3	4.1	-0.5
LF	PI	43.76	-2.14	6.98	1.05	0.60	-0.34	-5.48
	PD – PI	-3.51	0.24	-0.82	-0.26	0.15	0.07	0.53
	Change in %	-8.0	-11.0	-11.7	-24.4	25.6	-20.5	-9.7

and for the other budget terms is $m^2\ s^{-2}\ day^{-1}$. The total eddy energy increases by 1.7 % in HF while decreases by 8 % in LF, revealed the same opposite feedbacks as shown in Figure 4.3.

It is difficult to directly compare the total energy anomalies to the change of budget terms since the time-mean on the left-hand side of (4-1) and (4-2) is negligible in the steady state, and the sum of RHS tends to vanish. However, the budget analysis can still provide useful information to explore the reasons behind the scenes. Among all the HF budget terms in PI experiment (first row in Table 4.1), the BC is the largest energy source followed by the contribution from diabatic processes. The CFEI is small yet positive, and the three other terms are energy sinks (negative). Although the ADV only redistributes energy, it can still play as an energy source or sink in a non-closure domain, indicating the energy fluxes in or out on the boundaries (i.e., $20\ °N$ or $70\ °N$ in this case). In the PD experiment (second row; PD minus PI), the BC has the largest increase in magnitude (about 5.3 % in ratio), and the diabatic term is the second with a comparable amount of increase in ratio (4.1 %). The dramatic change in ratio for the CFEI (conversion of energy across frequencies) as well as the BT (conversion of kinetic energy between eddies and mean flow) implies the existence of highly nonlinear scale-interactions in response to the aerosol forcing. For the LF eddies, while the BC still has the largest contribution in the PI experiment $(+6.98)$, the diabatic processes do not play as an energy source like that in HF budgets. The BT also changes the sign (from -1.84 in HF to $+1.05$), meaning the LF eddies gain energy from the barotropic conversion. The decrease of LF total eddy energy is linked to the negative changes of BC (-0.82) and BT (-0.26), which are both negative feedbacks (i.e., change in ratio is negative) to cut down the energy source for LF eddies.

The positive ($+25.6\ \%$) and negative ($-20.5\ \%$) feedbacks in CFEI and diabatic terms are both opposite to the feedbacks (opposite sign in ratio) found in HF eddies, despite the magnitudes of these two terms are smallest among the budgets in PI experiment as well as in anomalies. To sum up, Table 4.1 suggests that the BC and diabatic terms are mostly related to the enhancement of HF eddy activities, and the reduction in LF is associated with the BC and BT terms. In the following sections, we will get a closer look at the geographical distributions of each term in the energetics equation.

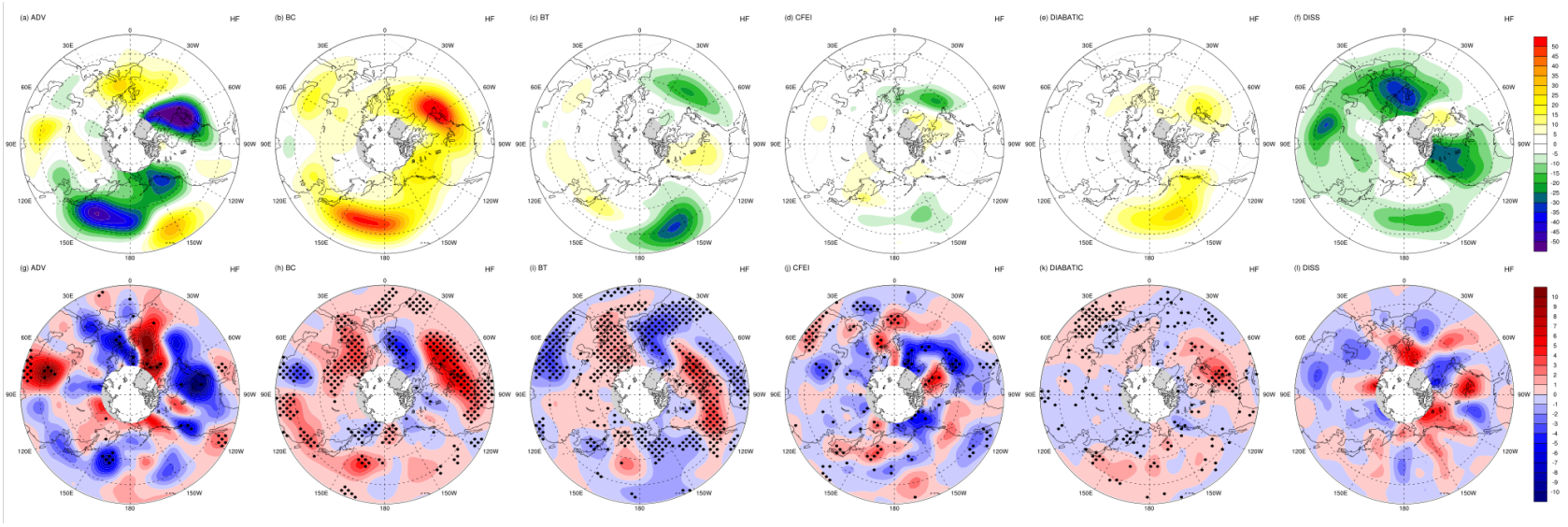

Figure 4.4 Vertically integrated, time-mean total HF eddy energy budgets in PI for (a) advection, (b) baroclinic conversion, (c) barotropic conversion, (d) cross-frequency eddy-eddy interaction, (e) diabatic processes and (f) dissipation terms. The anomalies (PD minus PI) for each term are shown below in (g), (h), (i), (j), (k), (l), respectively. The unit is $m^2\ s^{-2}\ day^{-1}$ with the dots indicating the 95% level of statistical significance.

4.3.1 Response in the High-Frequency Disturbances

Figure 4.4 demonstrates the horizontal distributions of column-averaged, time-mean total eddy energy budgets for HF eddies. The upper panels are the six budget terms using the same color scale ($\pm 50\ m^2\ s^{-2}$) for the PI experiment. The BC (Figure 4.4b) clearly illustrates the two major storm tracks and serves as the main energy source for the HF disturbances that extracting available potential energy from the background flow. The BT (Figure 4.4c), on the other hand, represents the exchange of kinetic energy between the HF eddies and mean flow, and therefore appears from the central of the two storm tracks toward the exit regions with negative values (energy sink for HF eddies). The positive BT in the between of two storm tracks (i.e., over the US) indicates a net conversion of kinetic energy from the mean flow to HF eddies, implying the importance of the barotropic processes dictating the HF disturbances in this region, such as the downstream development (Namias and Clapp 1944; Cressman 1948; Yeh 1949; Simmons and Hoskins 1979). The diabatic processes (Figure 4.4e) have positive contributions to the HF eddy activities, and the distributions collocate well with the precipitation patterns (see Figure 4.10 in the later discussion). The CFEI (Figure 4.4d) is smaller than other budget terms with negative contributions mainly occurring over the exit regions of storm track. The loss of HF eddy energy through the interactions across frequencies cannot be found in Table 4.1, where the net CFEI is positive ($+0.34\ m^s\ s^{-2}$) averaged over the extratropics. The ADV (Figure 4.4a) redistributes the total eddy energy resulting in the compensation against the energy increase by BC over the two storm tracks and the frictional dissipation by DISS over the Northern Europe and Central Asia, where the latter is beyond the discussion in this study.

The lower panels in Figure 4.4 show the changes of HF total eddy energy budgets (PD minus PI) with the dots emphasizing the 95 % level of statistical significance. It reveals the marked enhancement in BC and diabatic processes (Figures 4.4h, k) over the Pacific and Atlantic storm tracks, linked to the increase of HF total eddy energy (specifically, the increase of HF EAPE). The increase of BC further extends upstream into the continent (Southeast Asia and Southeast US, separately), indicating the intensified development of HF transient eddies in the PD experiment with increased aerosol loading. The pronounced increase of BT can be found over the United States in Figure 4.4i, and extents to the east Pacific where the cyclones exiting the Pacific storm track. It demonstrates a larger net conversion of kinetic energy from mean flow to support the HF eddies connecting the Pacific and Atlantic storm tracks. The negative effect for CFEI is also enhanced (Figure 4.4j), further dissipating the energy across frequencies. The change of ADV shows an overall agreement to the BC pattern in opposite sign (compensation effect), and the variation of DISS is smaller without statistical significance.

Due to the direct connections between the change of HF total eddy energy (Figure 4.3b) as well as BC and diabatic terms (Figure 4.4h, k), we examine the thermodynamic fields in Figure 4.5 to depict the processes dictating the variations in response to the aerosol forcing (especially the Asian emission; Figure 4.1). Figure 4.5a shows the anomalies of near surface air temperature extracted from the terrain-followed coordinate in the model at $\sigma = 0.9926$. The temperature is scaled by a factor of 0.1 in order to share the same color range with the other three panels in Figure 4.5, so the actual variation of temperature is $\pm 3\ K$. The warming maximum in Central Asia locates at $30\ °N$ (the dash circles indicate the latitudes of $30, 45, 60, 75\ °N$). Another local maximum of warming occurs at the

central United States together with the cooling at 45 °N along the east coast of the US. The dipole of cooling and warming over the Bering Sea is partially attributed to the reducing and weakening of blocking events occurred in the PD experiment, which will be discussed later in the LF eddy activities. Generally speaking, the patterns of temperature anomaly reveal the increase of low-level baroclinicity, which is determined by the horizontal

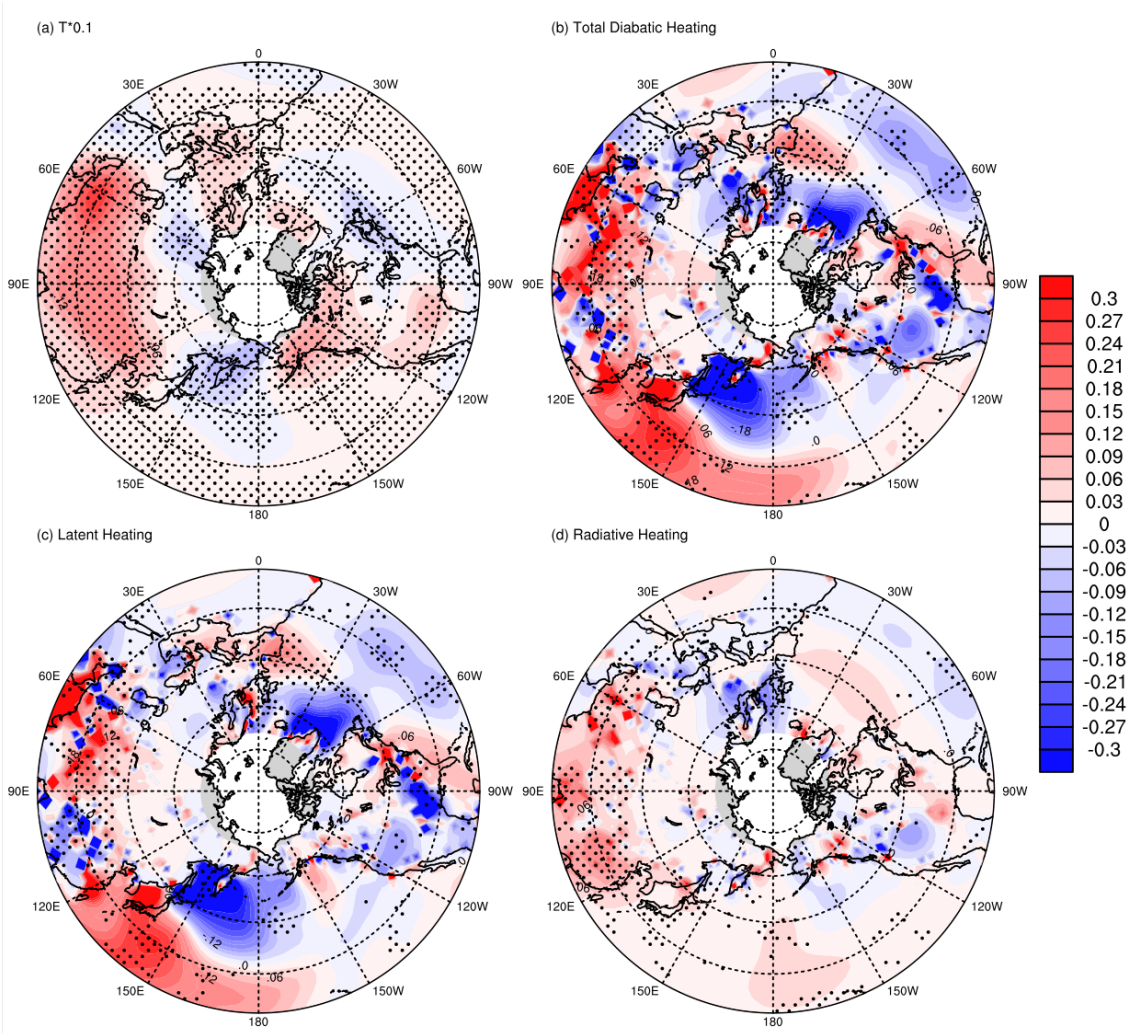

Figure 4.5 Anomalies (PD minus PI) of time-mean thermodynamic structures for (a) near surface air temperature, and averaged between 1000 and 500 hPa for (b) total diabatic heating, (c) latent heating and (d) radiative heating. The temperature in (a) is scaled by a factor of 0.1 to unify the color range (i.e., the actual temperature variations are between $\pm 3\ K$). The unit for (b), (c) and (d) is $K\ day^{-1}$. The dots indicate the 95% level of statistical significance.

gradient of temperature. Recalled that in (4-1) the magnitude of BC is proportional to the eddy perturbations ($\theta_H \mathbf{V}_H$) as well as the background baroclinicity ($\nabla\theta_m$), the temperature anomalies are able to highlight the change of BC in Figure 4.4h, although the total change of temperature results in a mixture of both physical and dynamic processes, which are including the direct diabatic forcing as well as nonlinear feedbacks through the scale-interactions (e.g., cloud radiative feedback and circulation-driven temperature advection).

The change of latent heating (Figure 4.5c), radiative forcing (Figure 4.5d) and their sum (Figure 4.5b) are averaged for the lower-troposphere between 1000 and 500 hPa. The patterns of total diabatic heating anomalies are dominated by the moisture processes, and is characterized by the marked increase from Central Asia to the central Pacific. The decrease in the southeast Asia and north to the Japan is attributed to the change of latent heat, which collocates well with the reduction of precipitation (see Figure 4.10 in the later discussion) and leads to the cooling spot north to the Japan (Figure 4.5a). The reduced precipitation over East Asia in response to the aerosol emissions (e.g., hindered warm rain processes, invigorated deep convection and extended hydrological cycle) has also been reported in many studies (Zhang et al. 2011; Zhou and Deng 2013; Wang et al. 2014). The anomalous total heating (and so does the latent heat) over the Atlantic also agrees with the precipitation change, where the increase of precipitation appears along the Atlantic storm track with the reduction found north to $75\ °N$ and south to $30\ °N$. Recalled that the diabatic term in (4-1) is proportional to the product of temperature and diabatic heating perturbation ($\theta_H Q_H$). Therefore, it can be inferred that the positive contribution of diabatic processes in the HF total eddy energy budgets found in Figure 4.4k stems from the increase of diabatic heating, and mostly attributes to the moist processes.

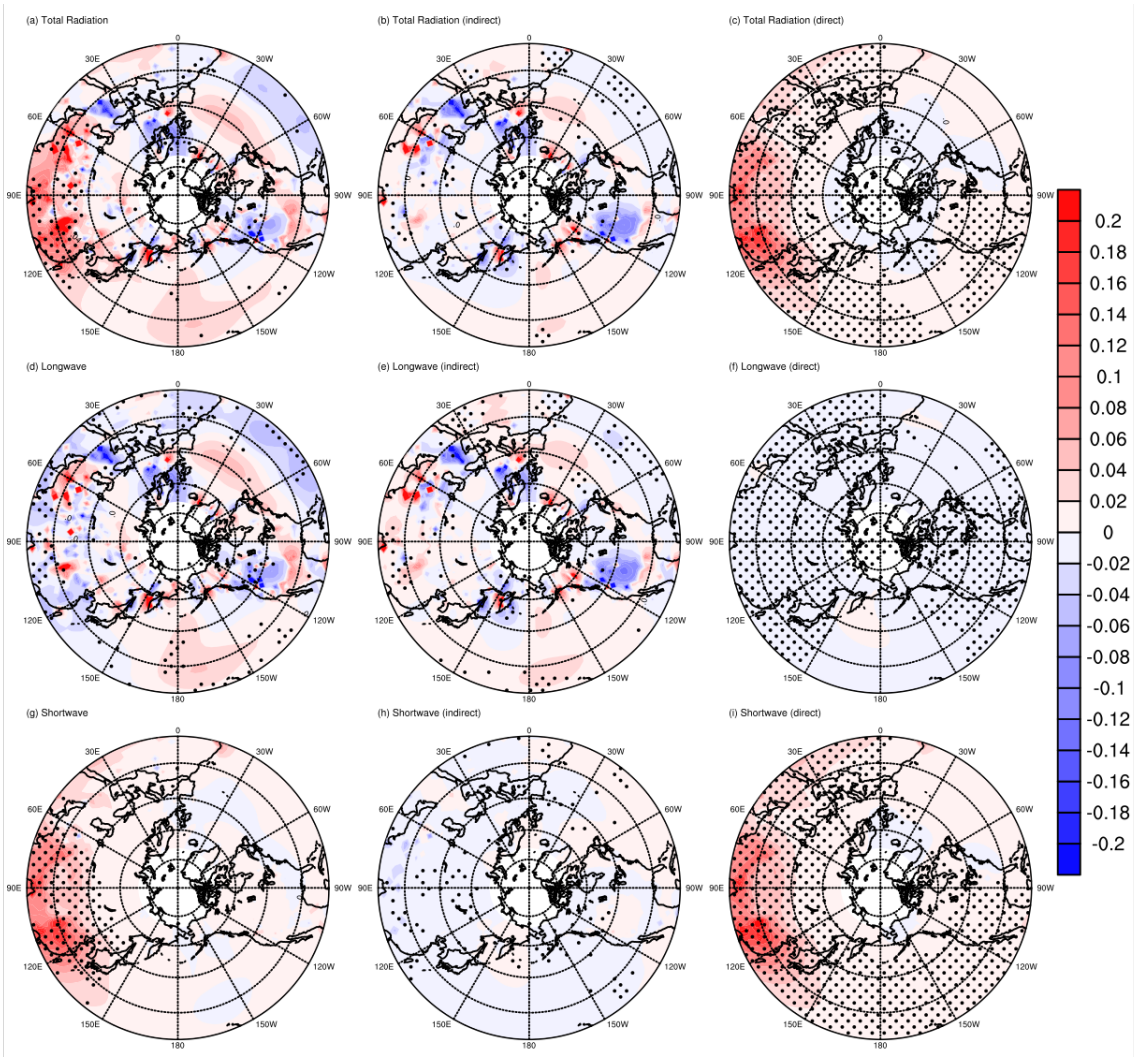

Figure 4.6 Anomalies (PD minus PI) of time-mean radiative forcing averaged between 1000 and 500 hPa in the unit of $K\ day^{-1}$. The first raw (a, b, c) is for total radiation, the second (d, e, f) for longwave and the last (g, h, i) for shortwave radiation. The changes are further attributed to the aerosol indirect effects (second column; b, e, h) and aerosol direct effects (last column; c, f, i). The dots indicate the 95% level of statistical significance.

Albite the generally smaller magnitude compared to the latent heat, the radiation (Figure 4.5d) plays an important role in warming the southeast Asia where the region is occupied by the large amount of aerosols shown in Figure 4.1. In order to depict the aerosol induced diabatic forcing in the radiative processes, the total radiation change is separated,

followed by Lu and Deng (2016), from the aerosol direct effect and aerosol indirect effect (through effecting cloud drops). The separation is done by as follow. The optical depth for the radiation scheme in the model is composed of three parts: air optical depth, cloud optical depth and AOD. The clear-sky (CS) radiation is obtained by neglecting the cloud optical depth, and the pristine-clear-sky (PCS) radiation is calculated by further removing the AOD. Therefore, the difference between PCS and CS is treated as the direct aerosol forcing, and the difference between CS and total radiation is the cloud effect. We approximate the aerosol direct effect as the difference of radiation due to aerosols between PI and PD experiments, and the aerosol (first) indirect effect as the difference of radiation due to clouds. In other words, the aerosol direct effect is defined as the change of aerosol absorption/scattering, and the aerosol indirect effect is defined as the change of cloud radiative heating in response to different emission scenarios.

The change of radiative heating (Figure 4.5d) is reproduced in Figure 4.6a with a smaller color scale, and divided into longwave (Figure 4.6d) and shortwave (Figure 4.6g) radiations. The second (third) column in Figure 4.6 shows the corresponding radiative forcing due to aerosol indirect (direct) effects. In the first column, it is clear that the total warming over the Asia results in the increase of shortwave heating, while the longwave radiation dictates the warming over the two central ocean basins as well as the dipole over the US. Specifically, the significant warming extending from Central Asia to the western Pacific is caused by the aerosol direct effects (Figure 4.6c) with the similar pattern of AOD found in Figure 4.1b, and can be attributed to the increase of absorption and scattering in shortwaves (Figure 4.6i) by high concentration of aerosols (e.g., black carbon; Figure 4.2c). For the aerosol indirect effects (via altering the cloud properties), the warming over the

ocean basins with maximum at the central Pacific and Atlantic (Figure 4.6b) is dominated by the longwave radiation (Figure 4.6e), resulted from the increase of cloud coverage (clouds live longer in the present of aerosols, or simply more HF disturbances occur in Figure 4.3b). The cooling spot on the west portion of the United States is, in the contrast, associated with the reduced cloud coverage shown in the decrease of HF (weather) disturbances in this area.

Back to the change of BC in HF total eddy energy budgets (Figure 4.4h), although the entrance regions of both storm tracks are characterized by positive anomalies linked to the increase of HF eddy activities (Figure 4.3b), they stem from very different mechanisms. In the East Asia, the large amount of aerosols absorbs shortwave radiation (aerosol direct effects), alters lower level baroclinicity, enhances BC energy conversion and leads to the increase of HF eddy activities in the Pacific storm track. On the other hand, due to the absence of dramatic change in aerosol concentrations over the Atlantic storm track, it is interesting why the response of HF eddies seems more significant and intense compared to the Pacific storm track. Albeit the "aerosol indirect effects" have small yet positive contribution in the longwave radiation to support the background baroclinicity (Figure 4.6e), the increase of BC more likely results from the strengthening of eddy activities. In other words, the increase of HF eddies is less likely driven by the increase of BC, but instead collectively contributes to the increase of total BC energy conversion. It is worth noting that BT (Figure 4.4i) over the United States can support the eddy kinetic energy by extracting energy from the kinetic energy of mean-flow. Studies suggest that the BT energy conversion in on eddy's dissipation stage can excite the development of neighbor downstream (Orlanski and Katzfey 1991; Chang 1993; Orlanski and Chang 1993).

Therefore, the increase of HF eddy activities in the Atlantic storm track may result from the enhanced downstream development, led by the strengthening of the Pacific storm track.

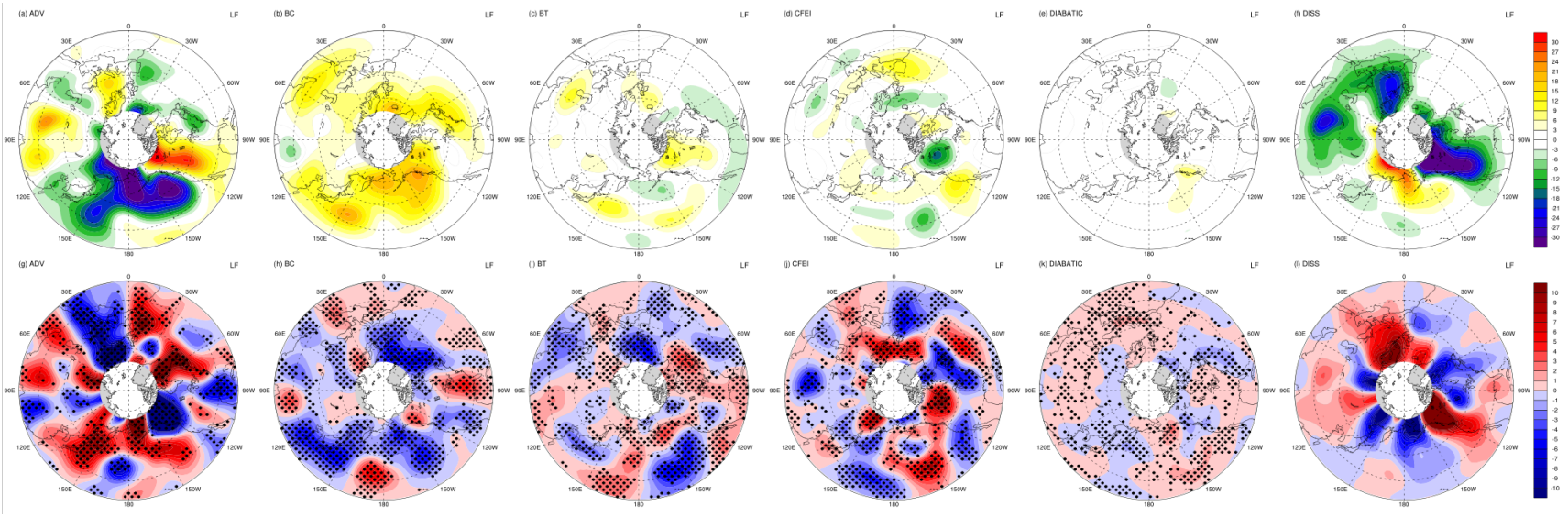

Figure 4.7 The same as Figure 4.4 but for LF eddies.

4.3.2 Response in the Low-Frequency Disturbances

Figure 4.7 is the counter part of Figure 4.4 for the LF eddies. In the upper panels, the BC (Figure 4.7b) has the major positive contributions in the LF energy budgets, and the patterns generally reveal the mean state of LF total eddy energy shown in Figure 4.3c. It suggests that the BC energy conversion from mean-flow available potential energy is also the main energy source for the LF disturbances (e.g., blockings and persistent lows). The eastward transport of energy by ADV (Figure 4.7a) can be found around $150\ °W$ and $0\ °W$, collocated with the downstream to the local maximum of LF eddy activities (Figure 4.3c). Then the energy ultimately dissipates through the mechanical frictions shown in the DISS (Figure 4.7f). In BT (Figure 4.7c), the loss of energy over the Gulf of Alaska and gain in the North America pass the LF eddy activities in the same direction as ADV, while the effects are compensated through the CFEI (Figure 4.7d). There is no surprise the diabatic processes have only minimal effects in LF (Figure 4.7e), where the moist and radiative processes are mostly tied to the weather disturbances, leading to the small heating term by the low-pass filtering.

The lower panels in Figure 4.7 show the response of the LF budgets to the increase of aerosols. The structures of significant decrease overall with some increase over the east part of United States for the LF activities (Figure 4.3d) can be revealed in the change of BC (Figure 4.7h). The energy redistribution processes (Figure 4.7g) are, again, compensating the change in BC. The regions with the marked decrease around the Gulf of Alaska and around the south of Greenland are characterized by consecutive blocking events in wintertime. The blocking index (Lejenas and Okland 1983; Tibaldi and Molteni 1990) is therefore examined on 500 hPa geopotential height (not shown), indicating a reduction

of blockings in the Pacific. The associated weakening of northerlies (cold advection) explain the discrepancy between the change of temperature (Figure 4.5a) and diabatic heating (Figure 4.5b) along the west coast of the United States where the warming is found with reduced diabatic heating. While the reduction in Atlantic is not evident by the blocking index, the negative feedbacks (the change of sign opposite to the PI) of the CFEI in Figure 4.7j imply the weakening of the LF eddy activities in the North Atlantic. In the discussion of Table 4.1, the BT $(-0.26\, m^2\, s^{-2})$ is simply the second large term attributed to the decrease of LF total eddy energy budgets. However, the change of spatial distribution (Figure 4.7i) reveals a lot more complexity in the region of two maximum LF eddy activities occurs. While the decrease over the east Pacific expended in a large area, the positive anomaly in the Gulf of Alaska (and therefore the peak activities in LF) is statistically significant. On the other hand, the decrease of BT is discovered at the peak LF activities in the Atlantic.

In the discussion of the BC change in HF by the direct aerosol effects over East Asia, the increase of HF EAPE is led by the modulation of background baroclinicity, where the same region in LF BC (Figure 4.7h) showing a strong negative feedback extended eastward to the Bering Sea and Gulf of Alaska, linked to the reduction of blocking events. Since the differences between HF BC and LF BC are $\theta_H \mathbf{V}_H$ verses $\theta_L \mathbf{V}_L$ multiplying the same $\nabla\theta_m$ (referred to (4-1) and (4-2)), it suggests that the increase of HF disturbances by the aerosol direct effects inhibits the BC energy conversion for LF eddies over East Asia and west Pacific.

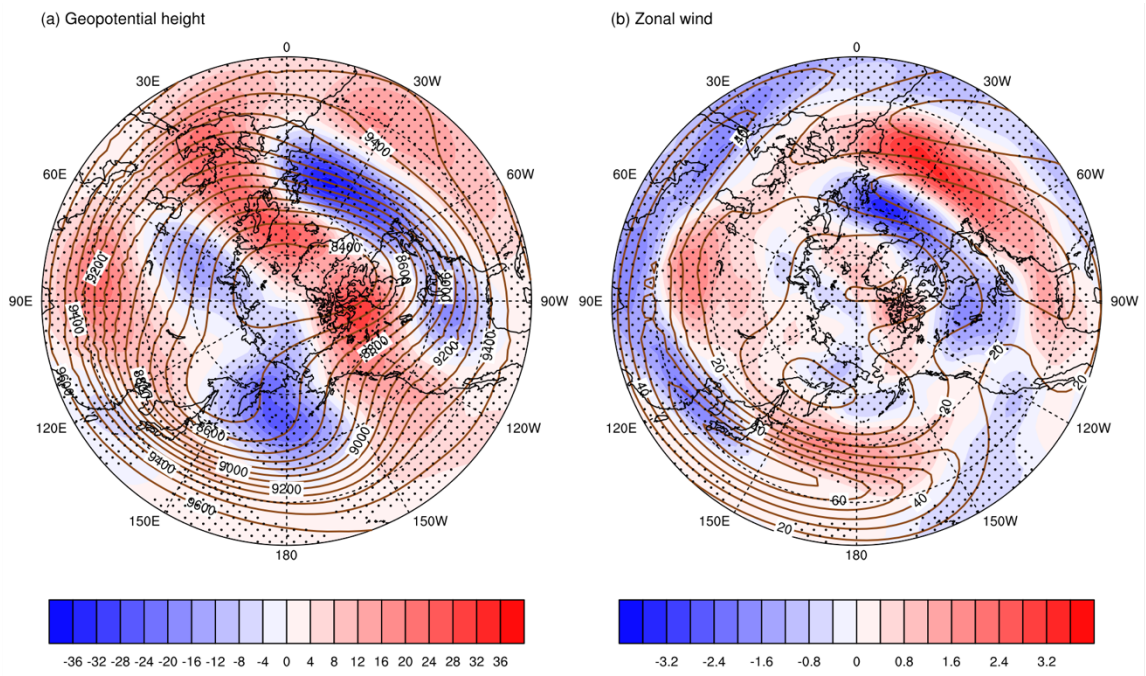

Figure 4.8 Time-mean circulations on 300 hPa for (a) geopotential height in m and (b) zonal wind in $m\ s^{-1}$. The contours are for PI experiment, and the shading is the anomaly (PD minus PI).

4.4 **Change in the Time-Mean Flow and Eddy Feedback**

The time-mean structures of geopotential height and zonal wind at 300 hPa in the PI experiment are shown as contours in Figure 4.8 with the color shading indicating the changes in the PD experiment. Figure 4.8a demonstrates the strengthened patterns in planetary waves, reflecting in the depended trough over the Bering Sea, the southward-extended ridge along the west coast of the United States and the other intensified trough over the North America. The westerly jet over the Pacific (Figure 4.8b) weakens in the entrance region and strengthens in the exist region. In the contrast to the zonal displacement of the Pacific jet, the Atlantic westerlies have marked meridional displacement toward the equator. Due to the thermal wind relationship, the intensity of upper-level westerlies (more

precisely, the vertical wind shear) in the extratropics often links to the meridional temperature gradient (baroclinicity). Therefore, we examine the maximum Eady Growth Rate (EGR; Eady 1949; Hoskins and Valdes,1990), a measure of vertical wind shear, at the lower-level (below 600 hPa, not shown). The change of lower-level EGR is generally in agreement with the anomalous westerlies at 300 hPa shown in Figure 4.8b, except for the region over East Asia where the westerlies weakened but the EGR increased north to the 30 $°N$ due to the radiative forcing by increased aerosols (Figure 4.6i). In other words, the presence of aerosols over East Asia concentrated in the lower level induces a baroclinic response to circulations while in other regions the responses are more coherent troughout the levels. The positive anomalies of zonal wind as well as the lower-level EGR from the south United States to the Atlantic can also be referred in the change of HF total eddy energy (Figure 4.3b).

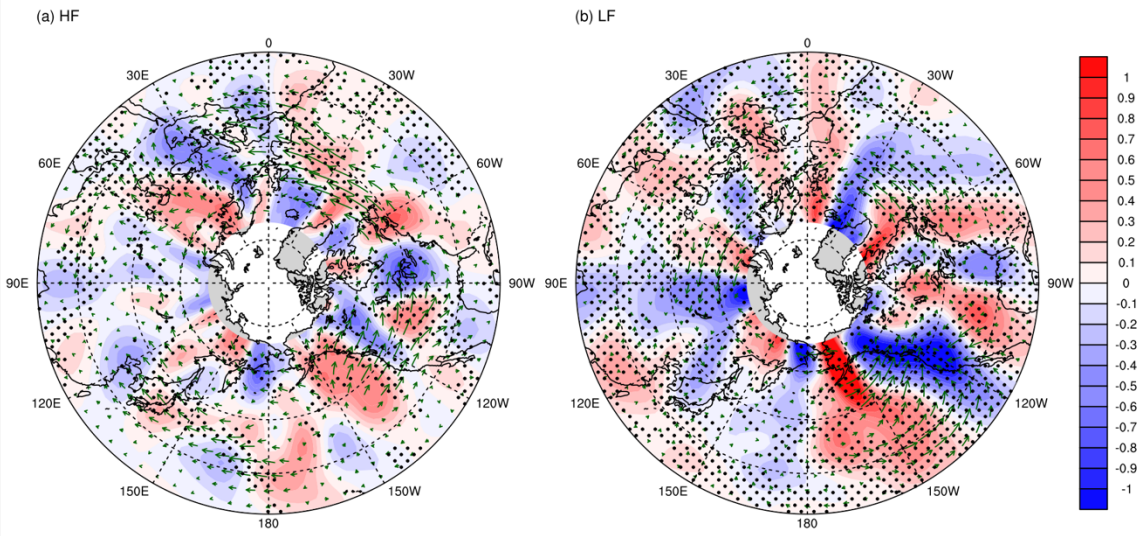

Figure 4.9 Anomalous (PD minus PI) **E**-vectors (vectors) and their divergence (shading, positive for divergence) for (a) HF and (b) LF eddies on 300 hPa. The unit for the shading is $10^{-5}\ m\ s^{-2}$. The dots indicate the 95% level of statistical significance.

To better understand the feedbacks of HF and LF eddy activities to the mean circulation, Figure 4.9 shows the differences (PD minus PI) of **E**-vectors and their divergence (color shading, positive for divergence) on 300 hPa for HF and LF eddies in the panels (a) and (b), separately. The **E**-vectors can be described as (Hoskins et al. 1983)

$$\mathbf{E} = (\overline{v'v' - u'u'}, -\overline{u'v'}) \tag{4-3}$$

where u' and v' are the perturbations of meridional and zonal winds. In this study, the filtered wind fields ($\boldsymbol{V}_H$ and $\boldsymbol{V}_L$) are adopted to compute the corresponding HF and LF **E**-vectors. Because the direction of **E**-vectors points to the energy propagation of transient eddies, the divergence (convergence) of **E**-vectors implies the acceleration (deceleration) of westerly mean flow that gain (loss) energy from eddies. Since Figure 4.9 only demonstrates the anomalies (PD minus PI), it is worth to note that, in the PI experiment, the extratropical HF eddies propagate energy downstream (eastward) while LF eddies propagate energy upstream (westward) in the manner of time-mean state (not shown). In Figure 4.9, the Student's t-test is applied on the X- and Y-components of **E**-vectors instead of the divergence field. Highlighted with the dots is where either one of X- or Y-components has 95% level of statistical significance on the change of **E**-vectors. The anomalous HF **E**-vectors (Figure 4.9a) point to the west over the west Pacific against the direction of mean state in the PI run, which may attribute to the deceleration of westerlies in this region. The anomalies show the propagation to the east starting from the Gulf of Alaska through the North America into the North Atlantic. On the other hand, the anomalous **E**-vectors in LF consistently propagate to the east, against their basic state (in the PI run) in general. What is more important are the spatial variations of these **E**-vectors

anomalies, which infers to the feedbacks to the mean flow, reflecting in divergence and convergence fields (color shading). The deceleration of westerlies over East Asia found in Figure 4.8 can be attributed to the convergence (negative values) of both HF and LF eddies. The same result is applied to the acceleration over the exit region of Pacific westerly jet, where the divergence of **E**-vectors can be found from $180\,°W$ to $160\,°W$ in both HF and LF. Over the west coast of the United States, the negative anomaly in Figure 4.8b (strengthening of easterlies) is mainly associated with the convergence of LF eddy energy (Figure 4.9b). Over the Atlantic, it appears the HF and LF both have contributions to the positive anomaly of zonal wind, while the central Atlantic (around $30\,°\mathrm{W}$) is more dominated by the HF eddies (note that not all changes between the westerlies and divergences of **E**-vectors match well due to the noise from scale-interactions). The comparison between these two fields on the same level still provides some insights in the transient eddy feedbacks in a limited extent.

Figure 4.10 shows the time-mean precipitation and the change in response to increased aerosols. The precipitation distribution in the PI experiment (contours) reveals the two major storm tracks. For the North Pacific storm track, the precipitation decreases over the continent (South and East Asia) and west Pacific even the increase of HF eddy activities is found in this region (Figure 4.3b). The result demonstrates how aerosols alter cloud properties and hinder raindrop formation. The increase of precipitation over the central Pacific north to the storm track and over the Bering Sea together with the decrease over the exit region extending to the west coast of the United States is attributed to the reduction of Pacific blocking (Figure 4.3d) that allows more trajectories of extratropical cyclones deflecting toward north. For the North Atlantic, the increase of precipitation is

statistically significant all over the storm track and consistent with the change of HF eddy activities (Figure 4.3b) as well as the mean westerly flow (Figure 4.8b).

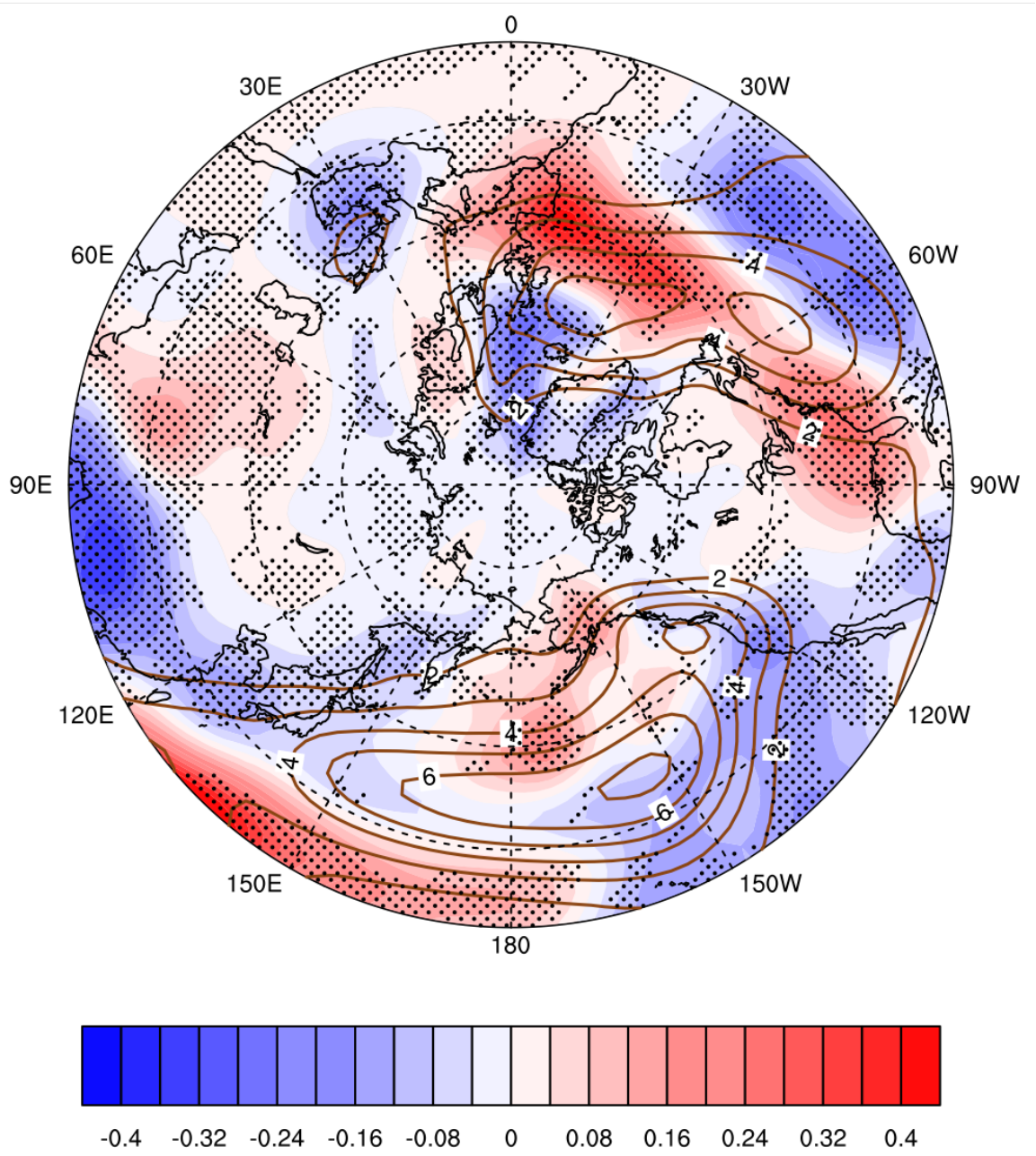

Figure 4.10 Time-mean precipitation for PI experiment (contours) and the change (shading) in the units of $mm\ day^{-1}$. The dots indicate the 95% level of statistical significance.

Figure 4.10 (precipitation) and Figure 4.5a (surface air temperature) suggest that the increase of anthropogenic aerosols interact with clouds and synoptic-scale disturbances, leading to the surface warming and precipitation reduction over East Asia. The impact propagates downstream across the North Pacific that reduces precipitation and increases the surface temperature along the west coast of the United States, while the east part of the United States experiences the opposite influences (i.e., increase of precipitation and decrease of surface temperature). Analyses of these two perpetual winter simulations reveal the potential impacts of anthropogenic aerosols on the short-term prediction of weather and long-term projection of climate in the Northern Hemisphere extratropics.

4.5 **Section Summary**

A pair of 2000-day perpetual winter simulations is conducted with preindustrial (PI) and present-day (PD) aerosol emission scenarios to investigate the impacts of aerosol effects on the wintertime extratropical circulations. The marked increase of aerosol concentrations is characterized by the Asian aerosol emissions extending from the south of Asia to the west Pacific. The first focus is the change in the activities of both HF and LF eddies (disturbances) in response to aerosol change from the pre-industrial condition to the present-day condition. In general, the total energy of the HF eddies in the North Pacific and North Atlantic storm track regions increases while the total energy of LF eddies decreases as a result of increased aerosol emission. Analyses of the eddy local energetics suggest the baroclinic (BC) energy conversion and diabatic processes are closely related to the enhanced HF eddy activity. Specifically, aerosol-induced solar heating change (i.e., aerosol direct effects) modulates the lower-level baroclinicity over East Asia, suggesting

the potential linkage to the enhanced BC energy conversion in its downstream storm track. On the other hand, the enhanced HF eddy activity over the North Atlantic is not directly driven by the aerosol forcing, but instead through the "downstream development" as the result of the increased barotropic (BT) energy conversion over the North America that is partly linked to the intensified HF eddies exiting the Pacific storm track. For the LF eddies, the decrease of total eddy energy can be traced back to the reduced BC processes. Specifically over the west Pacific, the increased HF BC conversion resulted from the direct aerosol forcing is accompanied with suppressed BC conversion for LF eddies. In association with reduced LF eddy activity over the Gulf of Alaska, the reduction of blocking events in this region leaves detectable changes in winter temperature along the west coast of the US. Results of the eddy E-vector analysis suggest that both HF and LF eddies provide feedbacks to the winter-mean flow, supporting the changes in the latter.

Chapter 3 of this dissertation reports the importance of coupling between aerosols and convective clouds in regards to the cyclone dynamics, and demonstrates how the CAMS mechanism causes the weakening of cyclones. This chapter examines the collective effects of aerosols in such frame work. The storm track response in the perpetual winter simulations does not reveal the weakening as suggested by the cyclone analysis in Chapter 3. It is noted that in the experiments of Chapter 3, the aerosol concentrations in the atmosphere are fixed (one-time vs. five-time) with the 3-dimentional distributions throughout the cyclone's lifecycle. In contract, the perpetual winter simulations in this chapter have more realistic aerosol treatments that include further details of aerosol processes (e.g., aerosol transportation, wet and dry removal processes). These processes are likely to diminish the signal seen in the cyclone analysis and the impact of CAMS

mechanism. Another issue is that the storm track response reported in this chapter has reached an equilibrium resulting from the nonlinear adjustments between transient eddies and background state. It is different from the analysis of sampled cyclone in chapter 3 with perturbed aerosol concentrations. The results suggest that the aerosol effects on a cluster of HF eddies are likely to be different compared to the effects on an individual HF eddy. The nonlinear dynamics involving eddy interaction with other eddies and mean flow tend to obscure the signals seen in an individual case, suggesting aerosol footprints in individual cyclones and in general circulation are not connected with each other in a straightforward way.

The change of HF (weather-scale) disturbances and precipitation patterns in response to the increased aerosol concentrations over East Asia and Pacific basin are largely in agreement with the previous studies. For instance, the reduction of precipitation over China and India and large warming over the United States are reported in Zhang et al. (2011) by using the Community Climate System Model version 3 (CCSM3). The intensification of Pacific storm track is also reported in Wang et al. (2014) by using the Pacific Northwest National Laboratory (PNNL) MMF model (with a subgrid cloud resolving model, same as the SP-CAM in this study). Zhou and Deng (2013) use the Community Atmosphere Model version 5 (CAM5) to conduct two long-term (11,000 days) perpetual winter simulations, and find that the Pacific is characterized by a marked decrease of LF activities over the Bering Sea and Gulf of Alaska with smaller increase of HF activities over the central Pacific in response to East Asian aerosols. The agreement between the results reported here and from previous studies indicates that the aerosol forcing dictates storm track dynamics over the Pacific mainly through the modulation of

lower-level baroclinicity by direct aerosol effects. Therefore, including the coupling between the aerosols and convections (aerosol indirect effects) does not lead to a dramatic difference in terms of extratropical eddy activities. Nonetheless, this study aims to document the dynamic and thermodynamical footprints left by aerosols in the extratropics wintertime, and demonstrate how the complex nonlinear interactions prevent from concluding a clear and clean result.

In this study, the perpetual winter setup with prescribed sea surface temperature is adopted to obtain a robust aerosol effects in a simplified controlled condition. However, the lack of air-sea coupling, in the same time, excludes the effects of seasonal cycle and longer time-scale variabilities, such as the interannual time-scale El Niño–Southern Oscillation (ENSO). Studies have reported that the storm tracks have strong variabilities in the seasonal (Nakamura 1992), interannual (Trenberth and Hurrell 1994; Zhang and Held 1999) and decadal (Nakamura and Izumi 1999; Ebisuzaki and Chelliah 1998) time-scales. It is interesting for the future studies to examine the impacts of aerosols on the storm tracks through the modulations of these variabilities.

The work presented in this chapter is submitted to the Climate Dynamics.

CHAPTER 5

CONCLUDING REMARKS

This dissertation explores the dynamic and thermodynamical footprints left by (anthropogenic) aerosols in extratropical weather disturbances and storm tracks. The hierarchy of numerical experiments is conducted from the simplest possible idealized case study to the more realistic long-term simulations to explore the modulations on cyclones and storm tracks in response to the aerosol direct and indirect effects. The main objective of this research is to gain the process-level understanding on how the aerosol forcing interacts with the dry dynamical processes, as well as the collective effects up-scaling to the mean state.

5.1 Dissertation Summary and Implications

In the first part of the study (Chapter 2), the aerosol indirect effects are examined in the idealized moist baroclinic wave simulations with WRF model. Comparing the aerosol direct effects (direct radiative forcing in shortwaves through absorption and scattering), the aerosol indirect effects (diabatic forcing through the modulations of cloud properties) are usually more important in weather disturbances due to the affecting time-scale of latent heat, which is much shorter and comparable to the weather systems than that of radiation. Therefore, to introduce the aerosol indirect effects in the first-order approach, the study in Chapter 2 doubles the DNC in the highly-idealized frame work for a development of baroclinic wave to mimic the increase of activated CCN in a polluted environment. Statistically significant differences between experiments where the DNC is

doubled and the control experiments are identified for an initial transient period before the cyclone enters the stage of rapid intensification (Figure 2.1). Doubling of the DNC increases total cloud water in the model, lowers the cloud level, and enhances latent heating to the east of the surface low, which strengthens the mid-tropospheric ridge (Figure 2.2). Subsequent changes in dry dynamical processes (e.g., advection of PV) as a result of the ridge strengthening lead to the deepening of the trough and ultimately produce a mild yet statistically significant strengthening of the baroclinic wave as a result of the DNC doubling (Figures 2.3 and 2.4). Piecewise PV inversion further confirms the critical role that latent heating change plays in strengthening the mid-tropospheric ridge (Figure 2.5).

The implications of the results reported in Chapter 2 of this dissertation highlight by the distinction in how tropical cyclones and extratropical cyclones are influenced by environmental aerosols. Aerosol effects on deep convective clouds (e.g., convection invigoration) are clearly crucial for understanding interactions between tropical cyclones and aerosols. However, convective clouds play only a secondary role in the overall life cycle of an extratropical cyclone, and the intensity of local convection does not positively correlate with the overall strength of an extratropical cyclone. As a result of the dominant role of dry dynamical processes in such a storm, the detection of aerosol effects becomes very challenging, and statistically robust signals might emerge for only a brief and transient period.

The idealized experiments by directly increasing DNC (see Chapter 2 of this dissertation) does not consider the explicit process of droplet activation. Most importantly, the idealized experiments are not capable of showing the impact of aerosols on deep convection due to the limitation of the cumulus parameterization used in the WRF model.

Moreover, the baroclinic waves originated from a zonally symmetric initial condition and evolved in a zonally periodic domain. It is intriguing what the response will be if the cyclone develops in a more realistic flow environment where interactions between the cyclone and surrounding weather systems are possible. Therefore, Chapter 3 of this dissertation investigates the impact of aerosols on an extratropical cyclone with the SP-CAM, which can explicitly resolve cloud-scale processes and aerosol-cloud interactions by embedding a subgrid CRM in the GCM frame work. By examining the results from 13 ensemble pairs of 1X-EXP (control) and 5X-EXP (5 times aerosol concentrations), it suggests that the growth rate of the cyclone is temporarily reduced (Figure 3.2). A *convection–advection–moisture self-adjustment (CAMS)* mechanism of aerosol–cyclone interaction is proposed to explain this finding. Specifically, the weakened growth is unambiguously attributed to the weakening of the cold advection underneath the mid-tropospheric trough of the cyclone (Figure 3.4, 3.5, 3.6). The weakened cold advection is in-turn driven by a decrease of the zonal temperature gradient that is tied to the reduced latent heating in the stratiform cloud region of the cyclone (Figure 3.11). Invigoration of convection ahead of the cold front by aerosols is found to be directly responsible for a suppressed moisture supply into the stratiform cloud region and thus the reduced latent heating there (Figure 3.10).

The discrepancy of the cyclone responses to the aerosol forcing between the WRF (Chapter 2) and SP-CAM (Chapter 3) simulations demonstrates the implications that incorporating aerosol microphysical effects on deep convections in any modeling effort is important to understand aerosol–circulation interactions in the extratropics. Despite the suppression effect of aerosols reported in Chapter 3 being transient, such effects may be

accumulated over regions with a high level of cyclone activity during winter seasons (e.g., over the oceanic storm tracks). The collective effects may thus leave a distinct footprint in the general circulation and surrounding regional climate, particularly downstream of these stormy regions given the major role played by these disturbances in momentum, energy, and moisture transport.

Motivated by the results described in Chapter 3, Chapter 4 of this dissertation explores the collective effects of aerosols in the extratropics from the long-term perpetual winter experiments. The first focus is the change in the activities of both HF and LF eddies (disturbances) in response to aerosol change from the pre-industrial condition to the present-day condition. As a result of increased aerosol emission, the total energy of the HF eddies in the North Pacific and North Atlantic storm track regions increases while the total energy of LF eddies decreases as a result of increased aerosol emission. Analyses of the eddy local energetics suggest the BC energy conversion and diabatic processes are closely related to the increase of HF eddy activities (Figure 4.4h, k). The aerosol-induced solar heating change modulates the lower-level baroclinicity, suggesting the potential linkage to the BC energy conversion over East Asia and its downstream storm track (Figure 4.5a, 4.6i). In contrast, the intensification of HF eddy activities over the Atlantic is attributed to the "downstream development" from the increased BT energy conversion over the North America that is partly linked to the intensified HF eddy activity exiting the Pacific storm track (Figure 4.4i). Over the Pacific, the increased HF BC conversion is accompanied with suppressed BC conversion for LF eddies (Figure 4.4h, 4.7h). In association with reduced LF eddy activity over the Gulf of Alaska, the reduction of blocking events in this region leaves detectable changes in winter temperature along the west coast of the United States

(Figure 4.3d, 4.5a). Results of the eddy E-vector analysis suggest that both HF and LF eddies provide feedbacks to the winter-mean flow, supporting the changes in the latter. Also discussed are the implications of these findings for the short-term prediction of weather and long-term projection of climate change in the northern extratropics.

The storm track response in Chapter 4 does not show the clear signal of weakening as suggested by the CAMS mechanism (Chapter 3). The result implies the aerosol footprints in individual cyclone and in general circulation are not connected with each other in a straightforward way. The results of the circulation changes (e.g., precipitation and temperature) in response to increased aerosols generally agree with previous studies albeit some of the models in those studies lack in coupling between aerosols and deep convections. In other words, the aerosol indirect effects in convective clouds for the mean circulations are not as crucial as that for the weather disturbances in the extratropics. The aerosol direct effects dictate the mean state baroclinicity, and therefore dominate the dry dynamical processes. However, it does not eliminate all the potential roles for the aerosol indirect effects played in the extratropical low-frequency variabilities since the perpetual winter simulations in Chapter 4 exclude those oscillations (e.g., seasonal and interannual variabilities).

In summary, Chapter 2 demonstrates the fundamental distinctions of aerosol impacts on extratropical disturbances from tropical cyclones (as well as deep convections), where the dry dynamical processes are not directly tied to the intensity of convections. The importance of aerosol indirect effects, especially in convective clouds, is highlighted in Chapter 3 within weather scale extratropical disturbances. Finally, the collective aerosol effects are documented in Chapter 4, indicating a potential role of aerosol direct radiative

forcing dominating the large-scale extratropical circulations. This dissertation delineates the dynamic and thermodynamical processes for the aerosol impacts on extratropical cyclones from idealized to comprehensive model simulations, from case study to large-scale circulation and from weather to climate (mean state). With the insights reported in this dissertation, these physical mechanisms and processes can be useful to understand the impacts of aerosols in short-term prediction of weather and long-term projection of climate for future studies.

5.2 **Directions for Future Studies**

It is widely known that aerosol effects are so complex with large uncertainties across a huge range of scales (i.e., from cloud to climate scales). This dissertation demonstrates whether incorporating the aerosol indirect effects in convections or not can make distinct results (Chapter 2 vs. Chapter 3) for the intensity change of cyclones. It also demonstrates how the aerosol direct effects can become more important in longer time-scales (Chapter 3 vs. Chapter 4) for the response of extratropical circulations. Future studies should verify the CAMS mechanism proposed in Chapter 3 from the long-term observations (i.e., satellite data) together with reanalysis dataset (e.g., European Centre for Medium-Range Weather Forecasts reanalysis). Furthermore, due to the nature of mixed cloud types in a cyclone reacting differently to aerosols, a higher resolution regional model with the capacity of resolving frontal structures and fully dealing with aerosol processes (i.e., WRF-Chem) may be able to provide additional insights about the aerosol impacts.

Beyond the weather scale, the perpetual winter setup in Chapter 4 inhibits the seasonal cycle and longer frequency variabilities (e.g., ENSO). To include such

variabilities, an air-sea coupled GCM is necessary, but will increase the dimension of freedom and computational cost at the same time. It also increases the challenge to separate the signal left by aerosols from the noise of cross-frequency interactions. Nevertheless, it is evident that aerosols have strong modulations on extratropical disturbances, and these transient eddies drive the regional climate and interact with low frequency oscillations. Therefore, future studies pursuing the process-level understanding of the aerosol forcing in this framework will provide the useful guideline to explain the climate change, and ultimately reduce the uncertainty of the aerosol climate impacts.

APPENDIX A

DERIVATION OF EDDY KINETIC ENERGY EQUATION

Following the previous works (i.e., Orlanski and Katzfey 1991; Jiang et al. 2013), the energy equations are derived for high-frequency (HF) and low-frequency (LF) eddies (defined as less than 10 days and 10 to 30 days, separately, in this study) to diagnose the collective responses of eddies to the aerosol forcing. The derivation of eddy kinetic energy (EKE) equation will be performed in Appendix A, and the eddy available potential energy (EAPE) equation in Appendix B. Appendix C will summarize the total energy (sum of EKE and EAPE) equation, and list the physical meaning and abbreviation for each term.

Start from a standard momentum equation in pressure coordinate

$$\frac{\mathrm{dV}}{\mathrm{dt}} + \omega\frac{\partial \mathrm{V}}{\partial \mathrm{p}} + \mathrm{f}\hat{\mathrm{k}}\times\mathrm{V} = -\nabla\Phi + \mathrm{F_r} \tag{A1.1}$$

where $\mathbf{V}$ is the two-dimensional horizontal wind velocity, $\omega = \frac{\mathrm{dp}}{\mathrm{dt}}$ the vertical velocity, f the Coriolis parameter, Φ the geopotential height, $\mathbf{F_r}$ the frictional forces, $\nabla = \left(\frac{\partial}{\partial x}, \frac{\partial}{\partial y}\right)$ the two-dimensional horizontal gradient and $\frac{d}{dt} = \frac{\partial}{\partial t} + \mathbf{V}\cdot\nabla$ the total derivative. In order to calculate the eddy activity, all fields are divided into the time-mean and deviation parts. For instance,

$$\mathrm{V} = \mathrm{V_m} + \mathrm{V}' \tag{A1.2}$$

$$\Phi = \Phi_\mathrm{m} + \Phi' \tag{A1.3}$$

where the subscript "m" denotes the time-mean and the prime indicates the departure from the mean state. Therefore, the EKE can be defined as

$$\mathrm{K_e} = \frac{1}{2}\mathrm{V}' \cdot \mathrm{V}' \tag{A1.4}$$

Expand (A1.1)

$$\left[\frac{\partial}{\partial t} + (\mathbf{V_m} + \boldsymbol{V}') \cdot \nabla_2\right](\mathbf{V_m} + \boldsymbol{V}') + (\omega_\mathrm{m} + \omega')\frac{\partial(\mathbf{V_m}+\boldsymbol{V}')}{\partial p} + f\hat{\mathbf{k}}\times(\mathbf{V_m} + \boldsymbol{V}')$$
$$= -\nabla(\Phi_\mathrm{m} + \Phi') + \mathbf{F}_{r\mathrm{m}} + \mathbf{F}'_r \tag{A1.5}$$

Taking a time average of (A1.5), we can get the momentum equation of time-mean flow

$$\frac{\partial \mathrm{V_m}}{\partial \mathrm{t}} + \mathrm{V_m} \cdot \nabla \mathrm{V_m} + \overline{\mathrm{V}' \cdot \nabla \mathrm{V}'} + \omega_\mathrm{m}\frac{\partial \mathrm{V_m}}{\partial \mathrm{p}} + \overline{\omega'\frac{\partial \mathrm{V}'}{\partial \mathrm{p}}} + \mathrm{f}\hat{\mathrm{k}}\times\mathrm{V_m}$$
$$= -\nabla\Phi_\mathrm{m} + \mathrm{F_{rm}} + \mathrm{F_0} \tag{A1.6}$$

where the overbar, $\overline{(\quad)}$, stands for the average over time. The $\mathrm{F_0}$ introduced here (followed by Orlanski and Katzfey 1991) is to represent any nonsteadiness of the mean flow to hold the generality of the equation, but it is usually small and negligible ($F_0 \approx 10^{-5}\ m\ s^{-2}$). To derive the momentum equation of transient flow, we subtract (A1.6) from (A1.5)

$$\frac{\partial \mathrm{V}'}{\partial \mathrm{t}} = -\mathrm{V_{3m}} \cdot \nabla_3 \mathrm{V}' - \mathrm{V}'_3 \cdot \nabla_3 \mathrm{V_m} - \mathrm{V}'_3 \cdot \nabla_3 \mathrm{V}' + \overline{\mathrm{V}'_3 \cdot \nabla_3 \mathrm{V}'}$$
$$-\mathrm{f}\hat{\mathrm{k}}\times\mathrm{V}' - \nabla\Phi' + \mathrm{F}'_\mathrm{r} - \mathrm{F_0} \tag{A1.7}$$

It is worth to note that the subscript "3" explicitly specifies the 3-dimentional flow where $\mathbf{V_{3m}} = (u_m, v_m, \omega_m)$, $\boldsymbol{V}'_3 = (u', v', \omega')$, and $\nabla_3 = \left(\frac{\partial}{\partial x}, \frac{\partial}{\partial y}, \frac{\partial}{\partial p}\right)$. The EKE equation is obtained by multiplying (A1.7) and $\boldsymbol{V}'$

$$\frac{\partial \mathrm{K_e}}{\partial \mathrm{t}} = -\mathrm{V_{3m}} \cdot \nabla_3 \mathrm{K_e} - \mathrm{V}' \cdot (\mathrm{V}'_3 \cdot \nabla_3)\mathrm{V_m} - \mathrm{V}'_3 \cdot \nabla_3 \mathrm{K_e} + \mathrm{V}' \cdot \overline{\mathrm{V}'_3 \cdot \nabla_3 \mathrm{V}'}$$
$$-\mathrm{V}' \cdot \nabla \Phi' + \mathrm{V}' \cdot \mathrm{F}'_\mathrm{r} - \mathrm{V}' \cdot \mathrm{F}_0 \qquad \text{(A1.8)}$$

The term $-\boldsymbol{V}' \cdot \nabla \Phi'$ can be further linked to the ageostrophic geopotential flux and vertical motion by combining the continuity and hydrostatic equations and vertically averaging through the troposphere

$$\nabla \cdot \boldsymbol{V}'_a = -\frac{\partial \omega'}{\partial \mathrm{p}} \qquad \text{(A1.9)}$$

$$\frac{\partial \Phi'}{\partial p} = -\alpha' \qquad \text{(A1.10)}$$

$$\frac{1}{\mathrm{p_2} - \mathrm{p_1}} \int_{\mathrm{p_1}}^{\mathrm{p_2}} \Phi' \frac{\partial \omega'}{\partial \mathrm{p}} \mathrm{dp} = \alpha' \omega' \qquad \text{(A1.11)}$$

$$-\mathrm{V}' \cdot \nabla \Phi' = -\nabla \cdot (\Phi' \mathrm{V}'_\mathrm{a}) - \alpha' \omega' \qquad \text{(A1.12)}$$

where α is the specific volume (and the prime, again, refers to the departure from the mean state), $\boldsymbol{V}'_a$ the ageostrophic transient flow, and the geostrophic component $\left(\boldsymbol{V}'_g\right)$ is assumed to be nondivergence in (A1.9). The final form of EKE equation can be re-ordered and summarized as

$$\frac{\partial \mathrm{K_e}}{\partial \mathrm{t}} = (-\mathrm{V_{3m}} \cdot \nabla_3 \mathrm{K_e} - \mathrm{V}'_3 \cdot \nabla_3 \mathrm{K_e}) - \nabla \cdot (\Phi' \mathrm{V}'_\mathrm{a}) - \alpha' \omega' - \mathrm{V}' \cdot (\mathrm{V}'_3 \cdot \nabla_3)\mathrm{V_m}$$
$$+\mathrm{V}' \cdot \overline{\mathrm{V}'_3 \cdot \nabla_3 \mathrm{V}'} + \mathrm{V}' \cdot \mathrm{F}'_\mathrm{r} - \mathrm{V}' \cdot \mathrm{F}_0 \qquad \text{(A1.13)}$$

In this study, we are interested in the energetics for the HF and LF eddies, so we further derive the EKE equation in a specific frequency bandwidth. By applying a high-pass (less than 10 days) and a band-pass (10 to 30 days) filters, the total circulation can be divided into three parts

$$\mathrm{V} = \mathrm{V_H} + \mathrm{V_L} + \mathrm{V_M} \tag{A1.14}$$

where the subscripts "H" and "L" stand for HF and LF, and the remaining part is denoted as "M". Because the time-average of $\mathrm{V_H}$ and $\mathrm{V_L}$ are both zero, the mean of $\mathrm{V_M}$ goes to $\mathrm{V_m}$ automatically. We can apply the same high-pass filter on (A1.7) to obtain the HF momentum equation

$$\frac{\partial \mathrm{V_H}}{\partial \mathrm{t}} = -\mathrm{V_{3m}} \cdot \nabla_3 \mathrm{V_H} - \mathrm{V_{3H}} \cdot \nabla_3 \mathrm{V_m} - \langle \mathrm{V_3'} \cdot \nabla_3 \mathrm{V'} \rangle^H$$
$$-\mathrm{f}\hat{\mathrm{k}} \times \mathrm{V_H} - \nabla \Phi_\mathrm{H} + \mathrm{F_{rH}} \tag{A1.15}$$

where the $\langle \quad \rangle^H$ stands for the high-pass filtering and the small term $\mathrm{F_0}$ is neglected for simplicity. Multiplying (A1.15) and $\mathrm{V_H}$ and going through the same procedure, we can get the final form of HF-EKE (as well as LF-EKE) equation

$$\frac{\partial \mathrm{K_H}}{\partial \mathrm{t}} = -\mathrm{V_{3m}} \cdot \nabla_3 \mathrm{K_H} - \nabla \cdot (\Phi_\mathrm{H} \mathrm{V_H}) - \mathrm{V_H} \cdot (\mathrm{V_{3H}} \cdot \nabla_3) \mathrm{V_m} - \mathrm{V_H} \cdot \langle \mathrm{V_3'} \cdot \nabla_3 \mathrm{V'} \rangle^H$$
$$-\alpha_\mathrm{H} \omega_H + \mathrm{V_H} \cdot \mathrm{F_{rH}} \tag{A1.15}$$
$$\frac{\partial \mathrm{K}_L}{\partial \mathrm{t}} = -\mathrm{V_{3m}} \cdot \nabla_3 \mathrm{K_L} - \nabla \cdot (\Phi_\mathrm{L} \mathrm{V_L}) - \mathrm{V_L} \cdot (\mathrm{V_{3L}} \cdot \nabla_3) \mathrm{V_m} - \mathrm{V_L} \cdot \langle \mathrm{V_3'} \cdot \nabla_3 \mathrm{V'} \rangle^L$$
$$-\alpha_\mathrm{L} \omega_L + \mathrm{V_L} \cdot \mathrm{F_{rL}} \tag{A1.16}$$

APPENDIX B

DERIVATION OF EDDY AVAILABLE POTENTIAL ENERGY EQUATION

To derive the EAPE equation, we start from a standard thermodynamic equation

$$\frac{\mathrm{d}\theta}{\mathrm{dt}} + \omega\frac{\partial\theta}{\partial \mathrm{p}} = \frac{\mathrm{Q}\theta}{\mathrm{c_p T}} \tag{A2.1}$$

$$\theta = T(p_0/p)^{\kappa} \tag{A2.2}$$

where c_p is the specific heat at constant pressure, $\kappa = R/c_p$, R the gas constant for dry air, p_0 a reference pressure (e.g., 1000 hPa in this study), Q the diabatic heating rate, T the air temperature, and θ the potential temperature. Other notations are the same as used in Appendix A. An eddy available potential energy per unit mass (Orlanski and Katzfey 1991) is defined as

$$\mathrm{A_e} = -\frac{\alpha_\mathrm{m}}{2\theta_\mathrm{m}}\frac{1}{\mathrm{d}\Theta/\mathrm{dp}}\theta'^2 \tag{A2.3}$$

where the potential temperature is divided into the mean state and departure ($\theta = \theta_m + \theta'$), and $\Theta = \Theta(p)$ is the Hemispheric horizontal average of potential temperature over time. First, we expand (A2.1)

$$\left[\frac{\partial}{\partial \mathrm{t}} + (\boldsymbol{V}_m + \boldsymbol{V}')\cdot\nabla\right](\theta_m + \theta') + (\omega_m + \omega')\frac{\partial(\theta_m+\theta')}{\partial \mathrm{p}} = \left(\frac{p_0}{p}\right)^{\kappa}\frac{(Q_m+Q')}{c_p} \tag{A2.4}$$

Taking a time average of (A2.4) to obtain the thermodynamic equation for the mean state

$$\frac{\partial \theta_m}{\partial t} + \mathbf{V}_m \cdot \nabla \theta_m + \overline{\overline{\mathbf{V}' \cdot \nabla \theta'}} + \omega_m \frac{\partial \theta_m}{\partial p} + \overline{\overline{\omega' \frac{\partial \theta'}{\partial p}}} = \frac{Q_m}{c_p} \left(\frac{p_0}{p}\right)^{\kappa} \quad \text{(A2.5)}$$

By subtracting (A2.5) from (A2.4), we can get the thermodynamic equation for the transient eddies

$$\frac{\partial \theta'}{\partial t} + \mathbf{V}_{3m} \cdot \nabla_3 \theta' + \mathbf{V}_3' \cdot \nabla_3 \theta' - \overline{\overline{\mathbf{V}_3' \cdot \nabla_3 \theta'}} + \mathbf{V}' \cdot \nabla \theta_m + \omega' \frac{\partial \theta_m}{\partial p} = \frac{Q'}{c_p} \left(\frac{p_0}{p}\right)^{\kappa} \quad \text{(A2.6)}$$

The final form of EAPE equation can be obtained by multiplying (A2.6) and $\left(-\frac{\alpha_m}{\theta_m} \frac{\theta'}{d\Theta/dp}\right)$

$$\frac{\partial A_e}{\partial t} = -\mathbf{V}_{3m} \cdot \nabla_3 A_e - \mathbf{V}_3' \cdot \nabla_3 A_e + \frac{\alpha_m}{\theta_m} \frac{\theta' \mathbf{V}'}{d\Theta/dp} \cdot \nabla \theta_m + \alpha' \omega'$$
$$-\theta' \left(\frac{\alpha_m}{\theta_m} \frac{\overline{\overline{\mathbf{V}_3'}}}{d\Theta/dp} \cdot \nabla_3 \theta'\right) - \frac{\alpha_m}{c_p \theta_m} \frac{\theta' Q'}{d\Theta/dp} \left(\frac{p_0}{p}\right)^{\kappa} \quad \text{(A2.7)}$$

where the fourth term on the right-hand side (RHS) results from an approximation that $d\Theta/dp \approx d\theta_m/dp$, which is generally hold for a large-scale area. The fifth term is vanished when averaging over the entire temporal domain. Next, in order to derive the HF-EAPE equation, we apply the high-pass filter to (A2.6)

$$\frac{\partial \theta_H}{\partial t} + \mathbf{V}_{3m} \cdot \nabla_3 \theta_H + \langle \mathbf{V}_3' \cdot \nabla_3 \theta' \rangle^H + \mathbf{V}_H \cdot \nabla \theta_m + \omega_H \frac{\partial \theta_m}{\partial p} = \frac{Q_H}{c_p} \left(\frac{p_0}{p}\right)^{\kappa} \quad \text{(A2.8)}$$

Multiplying (A2.8) and $\left(-\frac{\alpha_m}{\theta_m} \frac{\theta_H}{d\Theta/dp}\right)$ can give us the final form of HF-EAPE equation (the LF-EAPE equation is shown as well)

$$\frac{\partial A_H}{\partial t} = -\mathbf{V}_{3m} \cdot \nabla_3 A_H + \frac{\alpha_m}{\theta_m} \frac{\theta_H V_H}{d\Theta/dp} \cdot \nabla\theta_m + \alpha_H \omega_H + \frac{\alpha_m}{\theta_m} \frac{\theta_H}{d\Theta/dp} \langle \mathbf{V}_3' \cdot \nabla_3 \theta' \rangle^H$$

$$- \frac{\alpha_m}{c_p \theta_m} \frac{\theta_H Q_H}{d\Theta/dp} \left(\frac{p_0}{p} \right)^\kappa \qquad \text{(A2.9)}$$

$$\frac{\partial A_L}{\partial t} = -\mathbf{V}_{3m} \cdot \nabla_3 A_L + \frac{\alpha_m}{\theta_m} \frac{\theta_L V_L}{d\Theta/dp} \cdot \nabla\theta_m + \alpha_L \omega_L + \frac{\alpha_m}{\theta_m} \frac{\theta_L}{d\Theta/dp} \langle \mathbf{V}_3' \cdot \nabla_3 \theta' \rangle^L$$

$$- \frac{\alpha_m}{c_p \theta_m} \frac{\theta_L Q_L}{d\Theta/dp} \left(\frac{p_0}{p} \right)^\kappa \qquad \text{(A2.10)}$$

APPENDIX C

TOTAL EDDY ENERGY BUDGETS

The detail derivations of HF and LF EKE equations are demonstrated in Appendix A and EAPE equations in Appendix B. The final forms of the HF equations are repeated below for the convenience of referencing.

$$\frac{\partial \mathrm{K_H}}{\partial \mathrm{t}} = -\mathrm{V_{3m}} \cdot \nabla_3 \mathrm{K_H} - \nabla \cdot (\Phi_\mathrm{H} \mathrm{V_H}) - \mathrm{V_H} \cdot (\mathrm{V_{3H}} \cdot \nabla_3)\mathrm{V_m} - \mathrm{V_H} \cdot \langle \mathrm{V_3'} \cdot \nabla_3 \mathrm{V'} \rangle^H$$
$$-\alpha_\mathrm{H} \omega_H + \mathrm{diss_H} \tag{A3.1}$$

$$\frac{\partial \mathrm{A_H}}{\partial \mathrm{t}} = -\mathbf{V}_{3\mathrm{m}} \cdot \nabla_3 \mathrm{A_H} + \frac{\alpha_\mathrm{m}}{\theta_\mathrm{m}} \frac{\theta_\mathrm{H} \mathrm{V_H}}{\mathrm{d}\Theta/\mathrm{dp}} \cdot \nabla \theta_\mathrm{m} + \alpha_H \omega_H + \frac{\alpha_\mathrm{m}}{\theta_\mathrm{m}} \frac{\theta_\mathrm{H}}{\mathrm{d}\Theta/\mathrm{dp}} \langle \mathbf{V_3'} \cdot \nabla_3 \theta' \rangle^\mathrm{H}$$
$$-\frac{\alpha_\mathrm{m}}{\mathrm{c_p}\theta_\mathrm{m}} \frac{\theta_\mathrm{H} \mathrm{Q_H}}{\mathrm{d}\Theta/\mathrm{dp}} \left(\frac{\mathrm{p_0}}{\mathrm{p}}\right)^\kappa \tag{A3.2}$$

Starting from (A3.1), the first term on the RHS is the advection of eddy kinetic energy by the time-mean flow. The second term is the energy dispersion associated with ageostrophic geopotential flux. The third term is the conversion of kinetic energy between the time-mean flow and eddies, referred to as the barotropic conversion. In the fourth term, because the total transient eddies can be divided into different frequencies, this term acts as a production of kinetic energy via cross-frequency eddy-eddy interaction. The fifth term, $-\alpha_\mathrm{H} \omega_H$, is the baroclinic conversion of energy between EKE and EAPE, hence the same term with an opposite sign can also be found in (A3.2). The last term in (A3.1) is the energy dissipation due to frictional forces. The explicit form $(\mathrm{V_H} \cdot \mathrm{F_{rH}})$ in (A1.15) is replaced by $\mathrm{diss_H}$ here because we estimate this term from the residual of the EKE equation instead of direct calculation.

For the HF-EAPE equation in (A3.2), the first term on the RHS is the advection of eddy available potential energy by the mean flow. The second term corresponds to the traditional baroclinic conversion (i.e., the energy conversion from background available potential energy to EAPE). The physical meaning of the third term has been discussed in the previous paragraph. The fourth term is associated with the cross-frequency eddy-eddy interaction. The last term measures the generation of EAPE due to the diabatic processes.

The total HF eddy energy E_H is defined as the sum of EKE and EAPE

$$\mathrm{E_H} = \mathrm{K_H} + \mathrm{A_H} \tag{A3.3}$$

Therefore, the final form of total HF eddy energy budgets can be written as

$$\frac{\partial \mathrm{E_H}}{\partial \mathrm{t}} = \left[-\mathrm{V_{3m}} \cdot \nabla_3 \mathrm{K_H} - \nabla \cdot (\Phi_\mathrm{H} \mathrm{V_H}) - \mathbf{V}_{3\mathrm{m}} \cdot \nabla_3 \mathrm{A_H}\right] - \mathrm{V_H} \cdot (\mathrm{V_{3H}} \cdot \nabla_3)\mathrm{V_m} + \frac{\alpha_\mathrm{m}}{\theta_\mathrm{m}} \frac{\theta_\mathrm{H} \mathrm{V_H}}{\mathrm{d}\Theta/\mathrm{dp}} \cdot \nabla \theta_\mathrm{m}$$
$$+ \left[-\mathrm{V_H} \cdot \langle \mathrm{V_3'} \cdot \nabla_3 \mathrm{V'} \rangle^H + \left(\frac{\alpha_\mathrm{m}}{\theta_\mathrm{m}} \frac{\theta_\mathrm{H}}{\mathrm{d}\Theta/\mathrm{dp}}\right) \langle \mathbf{V_3'} \cdot \nabla_3 \theta' \rangle^\mathrm{H}\right] - \frac{\alpha_\mathrm{m}}{\mathrm{c_p}\theta_\mathrm{m}} \frac{\theta_\mathrm{H} \mathrm{Q_H}}{\mathrm{d}\Theta/\mathrm{dp}} \left(\frac{\mathrm{p_0}}{\mathrm{p}}\right)^\kappa + \mathrm{diss_H} \tag{A3.4}$$

For the convenience in discussion, we refer to (A3.4) symbolically as

$$\frac{\partial \mathrm{E_H}}{\partial \mathrm{t}} = \mathrm{ADV} + \mathrm{BT} + \mathrm{BC} + \mathrm{CFEI} + \mathrm{DIABATIC} + \mathrm{DISS} \tag{A3.5}$$

The terms are grouped based on the physical processes and given the abbreviations, i.e., ADV (advection), BT (barotropic conversion), BC (baroclinic conversion), CFEI (cross-frequency eddy-eddy interaction), DIABATIC (diabatic processes) and DISS (frictional dissipation), where

$$\mathrm{ADV} \equiv -\mathrm{V_{3m}} \cdot \nabla_3 \mathrm{K_H} - \nabla \cdot (\Phi_\mathrm{H} \mathrm{V_H}) - \mathrm{V_{3m}} \cdot \nabla_3 \mathrm{A_H} \tag{A3.6}$$

$$\mathrm{BT} \equiv -\mathrm{V_H} \cdot (\mathrm{V_{3H}} \cdot \nabla_3)\mathrm{V_m} \tag{A3.7}$$

$$\mathrm{BC} \equiv \frac{\alpha_\mathrm{m}}{\theta_\mathrm{m}} \frac{\theta_\mathrm{H} \mathbf{V_H}}{\mathrm{d}\Theta/\mathrm{dp}} \cdot \nabla\theta_\mathrm{m} \tag{A3.8}$$

$$\mathrm{CFEI} \equiv -\mathrm{V_H} \cdot \langle \mathrm{V_3'} \cdot \nabla_3 \mathrm{V'} \rangle^H + \left(\frac{\alpha_\mathrm{m}}{\theta_\mathrm{m}} \frac{\theta_\mathrm{H}}{\mathrm{d}\Theta/\mathrm{dp}}\right) \langle \mathbf{V_3'} \cdot \nabla_3 \theta' \rangle^\mathrm{H} \tag{A3.9}$$

$$\mathrm{DIABATIC} \equiv -\frac{\alpha_\mathrm{m}}{\mathrm{c_p}\theta_\mathrm{m}} \frac{\theta_\mathrm{H} \mathrm{Q_H}}{\mathrm{d}\Theta/\mathrm{dp}} \left(\frac{\mathrm{p_0}}{\mathrm{p}}\right)^\kappa \tag{A3.10}$$

$$\mathrm{DISS} \equiv \mathrm{diss_H} \tag{A3.11}$$

The counterpart for the total LF eddy energy budgets can be obtained in a similar manner, and only the result lists here for reference.

$$\frac{\partial \mathrm{E_L}}{\partial \mathrm{t}} = [-\mathrm{V_{3m}} \cdot \nabla_3 \mathrm{K_L} - \nabla \cdot (\Phi_\mathrm{L} \mathrm{V_L}) - \mathbf{V}_{3\mathrm{m}} \cdot \nabla_3 \mathrm{A_L}] - \mathrm{V_L} \cdot (\mathrm{V_{3L}} \cdot \nabla_3)\mathrm{V_m} + \frac{\alpha_\mathrm{m}}{\theta_\mathrm{m}} \frac{\theta_\mathrm{L} \mathbf{V_L}}{\mathrm{d}\Theta/\mathrm{dp}} \cdot \nabla\theta_\mathrm{m}$$

$$+ \left[-\mathrm{V_L} \cdot \langle \mathrm{V_3'} \cdot \nabla_3 \mathrm{V'} \rangle^L + \left(\frac{\alpha_\mathrm{m}}{\theta_\mathrm{m}} \frac{\theta_\mathrm{L}}{\mathrm{d}\Theta/\mathrm{dp}}\right) \langle \mathbf{V_3'} \cdot \nabla_3 \theta' \rangle^\mathrm{L}\right] - \frac{\alpha_\mathrm{m}}{\mathrm{c_p}\theta_\mathrm{m}} \frac{\theta_\mathrm{L} \mathrm{Q_L}}{\mathrm{d}\Theta/\mathrm{dp}} \left(\frac{\mathrm{p_0}}{\mathrm{p}}\right)^\kappa + \mathrm{diss_L} \tag{A3.12}$$

REFERENCES

Ackerman, A. S., O. B. Toon, D. E. Stevens, A. J. Heymsfield, V. Ramanathan, and E. J. Welton, 2000: Reduction of tropical cloudiness by soot. *Science,* **288,** 1042–1047.

Albrecht, B. A., 1989: Aerosols, cloud microphysics, and fractional cloudiness. *Science,* **245,** 1227–1230.

Andreae, M. O., D. Rosenfeld, P. Artaxo, A. A. Costa, G. P. Frank, K. M. Longo, and M. A. Silva-Dias, 2004: Smoking rain clouds over the Amazon. *Science,* **303,** 1337–1342.

Baker, M.B., Peter, T., 2008: Small-scale cloud processes and climate. *Nature,* **451 (7176),** 299–300.

Berggren, R., B. Bolin and C.-G. Rossby, 1949: An Aerological study of zonal motion, its perturbations and break-down. *Tellus,* **1,** 14-37.

Bjerknes, J., 1966: A possible response of the atmospheric Hadley circulation to equatorial anomalies of ocean temperature. *Tellus,* **18,** 820–829.

——, 1969: Atmospheric teleconnections from the equatorial Pacific. *Mon. Wea. Rev.,* **97,** 163–172.

Black, R. X., and R. M. Dole, 1993: The dynamics of large-scale cyclogenesis over the North Pacific Ocean. *J. Atmos. Sci.,* **50,** 421–442.

——, 1997: Deducing anomalous wave source regions during the life cycles of persistent flow anomalies, *J. Atmos. Sci.,* **54(7),** 895-907.

——, 1998: The maintenance of extratropical intraseasonal transient eddy activity in the GEOS-1 assimilated dataset. *J. Atmos. Sci.,* **55,** 3159–3175.

Blackmon, M. L., 1976: A climatological spectral study of the 500-mb geopotential height of the northern hemisphere, *J. Atmos. Sci.,* **33(8),** 1607–1623.

——, J. M. Wallace, N. C. Lau, and S. L. Mullen, 1977: An observational study of the northern hemisphere wintertime circulation, *J. Atmos. Sci.,* **34(7),** 1040–1053.

Bollasina, M. A., Y. Ming, and V. Ramaswamy, 2011: Anthropogenic aerosols and the weakening of the South Asian summer monsoon. *Science,* **334,** 502–505.

Bond, T. C., and Coauthors, 2013: Bounding the role of black carbon in the climate system: A scientific assessment. *J. Geophys. Res. Atmos.,* **118,** 5380–5552.

Boucher, O., and Coauthors, 2013: Clouds and aerosols. *Climate Change 2013: The Physical Science Basis,* T. F. Stocker, et al., Eds., *Cambridge University Press,* 571–658.

Branscome, L. E., W. J. Gutowski, and D. A. Stewart, 1989: Effects of surface fluxes on the nonlinear development of baroclinic waves. *J. Atmos. Sci.,* **46,** 460–475.

Branstator, G., 1995: Organization of storm track anomalies by recurring low-frequency circulation anomalies. *J. Atmos. Sci.,* **52,** 207–226.

Broccoli, A. J., and S. Manabe, 1992: The effects of orography on midlatitude Northern Hemisphere dry climates. *J. Climate,* **5,** 1181–1201.

Browning, K. A., and N. M. Roberts, 1994: Structure of a frontal cyclone. *Quart. J. Roy. Meteor. Soc.,* **120,** 1535–1557.

Cai, M., and M. Mak, 1990: Symbiotic relation between planetary and synoptic-scale waves. *J. Atmos. Sci.,* **47(24),** 2953-2968.

Chang, E. K. M., 1993: Downstream development of baroclinic waves as inferred from regression analysis. *J. Atmos. Sci.,* **50,** 2038– 2053.

——, and I. Orlanski, 1993: On the dynamics of a storm track. *J. Atmos. Sci.,* **50,** 999–1015.

——, 2001: GCM and observational diagnoses of the seasonal and interannual variations of the pacific storm track during the cool season, *J. Atmos. Sci.,* **58(13),** 1784-1800.

——, and Y. Fu, 2002: Interdecadal variations in Northern Hemisphere winter storm track intensity. *J. Climate,* **15,** 642–658.

——, S. Lee, and K. L. Swanson, 2002: Storm track dynamics. *J. Climate,* **15,** 2163–2183.

——, and S. Song, 2006: The seasonal cycles in the distribution of precipitation around cyclones in the Western North Pacific and Atlantic, *J. Atmos. Sci.,* **63(3),** 815-839.

——, and P. Zurita-Gotor, 2007: Simulating the seasonal cycle of the Northern Hemisphere storm tracks using idealized nonlinear storm-track models, *J. Atmos. Sci.,* **64(7),** 2309-2331.

Charney, J. G., 1947: The dynamics of long waves in a baroclinic westerly current. *J. Meteor.,* **4,** 135–162.

Chin, M., and Coauthors, 2004: Aerosol distribution in the Northern Hemisphere during ACE-Asia: Results from global model, satellite observations, and sun photometer measurements. *J. Geophys. Res.,* **109,** D23S90.

Connolly, P. J., T. W. Choularton, M. W. Gallagher, K. N. Bower, M. J. Flynn, and J. A. Whiteway, 2006: Cloud-resolving simulations of intense tropical Hector thunderstorms: Implications for aerosol–cloud interactions. *Quart. J. Roy. Meteor. Soc.,* **132,** 3079–3106.

Creamean, J. M., and Coauthors, 2013: Dust and biological aerosols from the Sahara and Asia influence precipitation in the western U.S. *Science,* **339,** 1572–1578.

Cressman, G. P., 1948: On the forecasting of long waves in the upper westerlies. *J. Meteor.,* **5,** 44–57.

Davis, C. A., M. T. Stoelinga, and Y.-H. Kuo, 1993: The integrated effect of condensation in numerical simulations of extratropical cyclogenesis. *Mon. Wea. Rev.,* **121,** 2309–2330.

DeMott, P. J., and Coauthors, 2010: Predicting global atmospheric ice nuclei distributions and their impacts on climate. *Proc. Natl. Acad. Sci. USA,* **107,** 11 217–11 222.

Deng, Y., and M. Mak, 2005: An idealized model study relevant to the dynamics of the midwinter minimum of the Pacific storm track, *J. Atmos. Sci.,* **62(4),** 1209-1225.

Dole, R. M., and N. D. Gordon, 1983: Persistent anomalies of the extratropical Northern Hemisphere wintertime circulation: Geographical distribution and regional persistence characteristics, *Mon. Wea. Rev.,* **111(8),** 1567-1586.

——, 1986: Persistent anomalies of the extratropical Northern Hemisphere wintertime circulation. *Mon. Wea. Rev.,* **114,** 178– 207.

——, and R. X. Black, 1990: Life cycles of persistent anomalies. Part II: The development of persistent negative height anomalies over the North Pacific Ocean, *Mon. Wea. Rev.,* **118(4),** 824-846.

O'Dowd, C. D., Lowe, J. A., Smith, M. H. & Kaye, A. D., 1999: The relative importance of non-sea-salt sulphate and sea-salt aerosol to the marine cloud condensation nuclei population: an improved multi-component aerosol-cloud droplet parameterization. *Q. J. R. Meteorol. Soc.* **125,** 1295–1313.

Durant, A. J., and R. A. Shaw, 2005: Evaporation freezing by contact nucleation inside-out. *Geophys. Res. Lett.,* L20814.

Eady, E. T., 1949: Long waves and cyclone waves. *Tellus,* **1,** 33–52.

Ebisuzaki, W., and M. Chelliah, 1998: ENSO and inter-decadal variability in storm tracks over North America and vicinity. *Proc. 23d Annual Climate Diagnostics and Prediction Workshop, Miami, FL, NOAA,* 243–246.

Ekman, A. M. L., A. Engstrom, and C. Wang, 2007: The effect of aerosol composition and concentration on the development and anvil properties of a continental deep convective cloud. *Quart. J. Roy. Meteor. Soc.,* **133,** 1439–1452.

Emanuel, K. A., M. Fantini, and A. J. Thorpe, 1987: Baroclinic instability in an environment of small stability to slantwise moist convection. Part I: Two-dimensional models. *J. Atmos. Sci.,* **44,** 1559 –1573.

Fan, J., R. Zhang, G. Li, W.-K. Tao, and X. Li, 2007: Simulation of cumulus clouds using a spectral microphysics cloud-resolving model, *J. Geophys. Res.,* **112,** D04201.

Fan, J., J. M. Comstock, and M. Ovchinnikov, S. A. McFarlane, G. McFarquhar, and G. Allen, 2010: Tropical anvil characteristics and water vapor of the tropical tropopause layer: Impact of heterogeneous and homogeneous freezing parameterizations. *J. Geophys. Res.,* **115,** D00K33.

Fan, J., L. R. Leung, D. Rosenfeld, Q. Chen, Z. Li, J. Zhang, and H. Yan, 2013: Microphysical effects determine macrophysical response for aerosol impacts on deep convective clouds. *Proc. Natl. Acad. Sci. USA,* **110,** E4581–E4590.

——, and Coauthors, 2015: Improving representation of convective transport for scale-aware parameterization: I. Convection and cloud properties simulated with spectral bin and bulk microphysics. *J. Geophys. Res. Atmos.,* **120,** 3485–3509.

Fantini, M., 1995: Moist Eady waves in a quasi-geostrophic three-dimensional model. *J. Atmos. Sci.,* **52,** 2473–2485.

Farrell, B. F., 1982: The initial growth of disturbances in a baroclinic flow. *J. Atmos. Sci.,* **39,** 1663–1686.

——, 1984: Modal and non-modal baroclinic waves. *J. Atmos. Sci.,* **41,** 668–673.

——, and P. J. Ioannou, 1995: Stochastic dynamics of the midlatitude atmospheric jet. *J. Atmos. Sci.,* **52,** 1642–1656.

Field, P. R., Hogan, R. J., Brown, P. R. A., Illingworth, A. J., Choularton, T. W., Kaye, P. H., Hirst, E., and Greenaway, R., 2004: Simultaneous radar and aircraft observations of mixed-phase cloud at the 100m scale, *Q. J. Roy. Meteor. Soc.,* **130,** 1877–1904.

Fusina, F., Spichtinger, P., Lohmann, U., 2007: Impact of ice supersaturated regions and thin cirrus on radiation in the midlatitudes. *J. Geophys. Res.,* **112,** D24S14.

Geng, Q., and M. Sugi, 2001: Variability of the North Atlantic cyclone activity in winter analyzed from NCEP–NCAR reanalysis data. *J. Climate,* **14,** 3863–3873.

Grabowski, W. W., 2014: Extracting microphysical impacts in large-eddy simulations of shallow convection. *J. Atmos. Sci.,* **71,** 4493–4499.

Graham, N. E., and H. F. Diaz, 2001: Evidence for intensification of North Pacific winter cyclones since 1948. *Bull. Amer. Meteor. Soc.,* **82,** 1869–1893.

Green, J. S. A., 1977: The Weather During July 1976: Some dynamical considerations of the drought. *Weather,* **32,** 120-128.

Gustafson, W. I., L. K. Berg, R. C. Easter, and S. J. Ghan, 2008: The explicit–cloud parameterized–pollutant hybrid approach for aerosol–cloud interactions in multiscale modeling framework models: Tracer transport results. *Environ. Res. Lett.,* **3,** 025005.

Gutowski, W. J., L. E. Branscome, and D. A. Stewart, 1992: Life cycles of moist baroclinic eddies. *J. Atmos. Sci.,* **49,** 306–319.

Hakim, G. J., 2000: Role of nonmodal growth and nonlinearity in cyclogenesis initial-value problems. *J. Atmos. Sci.,* **57,** 2951–2967.

Hall, N. M. J., and P. D. Sardeshmukh, 1998: Is the time-mean Northern Hemisphere flow baroclinically unstable? *J. Atmos. Sci.,* **55,** 41–56.

Haines, K., and J. Marshall, 1987: Eddy-forced coherent structures as a prototype of atmospheric blocking. *Quart. J. Roy. Meteor. Soc.,* **113,** 681–704.

Harnik, N., and E. K. M. Chang, 2004: The effects of variations in jet width on the growth of baroclinic waves: implications for midwinter pacific storm track variability. *J. Atmos. Sci.,* **61(1),** 23-40.

Hartmann, D.L., Doelling, D., 1991: On the net radiative effectiveness of clouds. *J. Geophys. Res.-Atmos.,* **96 (D1),** 869–891.

Hayashi, Y., 1980: Estimation of nonlinear energy transfer spectra by the cross-spectral method, *J. Atmos. Sci.,* **37(2),** 299-307.

Held, I. M., S. W. Lyons, and S. Nigam, 1989: Transients and the extratropical response to El Nino. *J. Atmos. Sci.,* **46,** 163–174.

——, 1993: Large scale dynamics and global warming. *Bull. Amer. Meteor. Soc.,* **74,** 228–241.

Hinman, R., 1888: *Eclectic Physical Geography.* Van Antwerp, Bragg and Co., 382 pp.

Holton, J. R., 2004: *An Introduction to Dynamic Meteorology.* 4th ed. Elsevier Academic Press, 535 pp.

Hoskins, B. J., I. N. James, G. H. White, 1983: The shape, propagation and mean-flow interaction of large-scale weather systems. *J. Atmos. Sci.,* **40,** 1595–1612.

——, and P. J. Valdes, 1990: On the existence of storm tracks. *J. Atmos. Sci.,* **47,** 1854–1864.

Hsu, P.-C., T. Li, and C.-H. Tsou, 2010: Interactions between boreal summer intraseasonal oscillations and synoptic-scale disturbances over the Western North Pacific. Part I: Energetics diagnosis, *J. Climate,* **24(3),** 927-941.

Huang, J., B. Lin, P. Minnis, T. Wang, X. Wang, Y. Hu, Y. Yi, and J. K. Ayers, 2006a: Satellite-based assessment of possible dust aerosols semi-direct effect on cloud water path over East Asia. *Geophys. Res. Lett.,* **33,** L19802.

——, P. Minnis, B. Lin, T. Wang, Y. Yi, Y. Hu, A. Sun-Mack, and K. Ayers, 2006b: Possible influences of Asian dust aerosols on cloud properties and radiative forcing observed from MODIS and CERES. *Geophys. Res. Lett.,* **33,** L06824.

——, ——, H. Yan, Y. Yi, B. Chen, L. Zhang, and J. Ayers, 2010: Dust aerosol effect on semi-arid climate over northwest China detected from A-Train satellite measurements. *Atmos. Chem. Phys.,* **10,** 6863–6872.

Huebert, B. J., T. Bates, P. B. Russell, G. Shi, Y. J. Kim, K. Kawamura, G. Carmichael, and T. Nakajima, 2003: An overview of ACE-Asia: Strategies for quantifying the relationships between Asian aerosols and their climatic impacts. *J. Geophys. Res.,* **108,** 8633.

Hurrell, J. W., J. J. Hack, D. Shea, J. M. Caron, and J. Rosinski, 2008: A new sea surface temperature and sea ice boundary dataset for the Community Atmosphere Model. *J. Climate,* **21,** 5145–5153.

Illari, L. and J. C. Marchall, 1983: On the interpretation of eddy fluxes during a blocking episode. *J. Atmos. Sci.,* **40,** 2232-2242.

——, 1984: A diagnostic study of the potential vorticity in a warm blocking anticyclone. *J. Atmos. Sci.,* **41,** 3518-3526.

IPCC, 2007: *Climate Change 2007: The Physical Science Basis.* Cambridge University Press, 996 pp.

——, 2013: *Climate Change 2013: The Physical Science Basis.* Cambridge University Press, 1535 pp.

James, I. N., 1987: Suppression of baroclinic instability in horizontally sheared flows. *J. Atmos. Sci.,* **44,** 3710–3720.

Jiang, T., Y. Deng, and W. Li, 2013: Local kinetic energy budget of high-frequency and intermediate-frequency eddies: winter climatology and interannual variability. *Climate Dyn.,* **41,** 961–976.

Kanitz, T., Seifert, P., Ansmann, A., Engelmann, R., Althausen, D., Casiccia, C., and Rohwer, E. G., 2011: Contrasting the impact of aerosols at northern and southern midlatitudes on heterogeneous ice formation. *Geophys. Res. Lett.,* **38,** L17802.

Khain, A., A. Pokrovsky, M. Pinsky, A. Seigert, and V. Phillips, 2004: Simulation of effects of atmospheric aerosols on deep turbulent convective clouds using a spectral microphysics mixed-phase cumulus cloud model: Part I. Model description and possible applications. *J. Atmos. Sci.,* **61,** 2983–3001.

——, and ——, 2004: Simulation of effects of atmospheric aerosols on deep turbulent convective clouds using a spectral microphysics mixed-phase cumulus cloud model: Part II. Sensitivity study. *J. Atmos. Sci.,* **61,** 2963–2982.

——, D. Roseenfeld, and A. Pokrovsky, 2005: Aerosol impact on the dynamics and microphysics of deep convective clouds. *Q. J. R. Meteorol. Soc.,* **131,** 2639–2663.

Khairoutdinov, M. F., and D. A. Randall, 2003: Cloud resolving modeling of the ARM summer 1997 IOP: Model formulation, results, uncertainties, and sensitivities. *J. Atmos. Sci.,* **60,** 607–625.

Korolev, A. V., Isaac, G. A., Cober, S. G., Strapp, J. W., and Hallett, J., 2003: Microphysical characterization of mixed-phase clouds. *Q. J. Roy. Meteor. Soc.,* **129,** 39–65.

Kulkarni, G., J. Fan, J. M. Comstock, X. Liu, and M. Ovchinnikov, 2012: Laboratory measurements and model sensitivity studies of dust deposition ice nucleation. *Atmos. Chem. Phys.,* **12,** 7295–7308.

Kung, E. C., 1977: Energy source in middle-latitude synoptic-scale disturbances. *J. Atmos. Sci.,* **34,** 1352–1365.

Kuo, H. L., 1972: On a generalized potential vorticity equation for quasi-geostrophic flow. *Pure Appl. Geophys.,* **96,** 171–175.

Lamarque, J. F., et al., 2010: Historical (1850-2000) gridded anthropogenic and biomass burning emissions of reactive gases and aerosols: Methodology and application. *Atmos. Chem. Phys.,* **10(15),** 7017–7039.

Lau, N.-C., 1978: On the three-dimensional structure of the observed transient eddy statistics of the Northern Hemisphere wintertime circulation. *J. Atmos. Sci.,* **35,** 1900–1923.

——, 1979: The structure and energetics of transient disturbances in the Northern Hemisphere wintertime circulation. *J. Atmos. Sci.,* **36,** 982–995.

——, 1988: Variability of the observed midlatitude storm tracks in relation to low-frequency changes in the circulation pattern. *J. Atmos. Sci.,* **45,** 2718–2743.

——, and M. J. Nath, 1991: Variability of the baroclinic and barotropic transient eddy forcing associated with monthly changes in the midlatitude storm tracks. *J. Atmos. Sci.,* **48,** 2589–2613.

Lau, K.-M., and K.-M. Kim, 2006: Observational relationships between aerosol and Asian monsoon rainfall, and circulation. *Geophys. Res. Lett.,* **33,** L21810.

Lee, S., and I. M. Held, 1993: Baroclinic wave packets in models and observations. *J. Atmos. Sci.,* **50,** 1413–1428.

Lee, S. S., L. J. Donner, and V. T. J. Phillips, 2009: Impacts of aerosol chemical composition on microphysics and precipitation in deep convection. *Atmos. Res.,* **94,** 220–237.

Lee, W.-J., and M. Mak, 1996: The role of orography in the dynamics of storm tracks. *J. Atmos. Sci.,* **53,** 1737–1750.

Lejenas, H., and H. Okland, 1983: Characteristics of Northern Hemisphere blocking as determined from a long time series of observational data. *Tellus,* **35A,** 350-362.

Li, G., Y. Wang, K.-H. Lee, Y. Diao, and R. Zhang, 2008a: Increased winter precipitation over the North Pacific from 1984–1994 to 1995–2005 inferred from the Global Precipitation Climatology Project. *Geophys. Res. Lett.,* **35,** L13821.

——, Y. Wang, and R. Zhang, 2008b: Implementation of a two-moment bulk microphysics scheme to the WRF model to investigate aerosol-cloud interaction. *J. Geophys. Res.,* **113,** D15211.

Li, Z., F. Niu, J. Fan, Y. Liu, D. Rosenfeld, and Y. Ding, 2011: Long-term impacts of aerosols on the vertical development of clouds and precipitation. *Nat. Geosci.,* **4,** 888–894.

Lindzen, R. S., and B. J. Farrell, 1980: A simple approximate result for the maximum growth rate of baroclinic instabilities. *J. Atmos. Sci.,* **37,** 1648–1654.

Liu, X., and Coauthors, 2012a: Toward a minimal representation of aerosols in climate models: Description and evaluation in the community atmosphere model CAM5. *Geosci. Model Dev.,* **5,** 709–739.

——, X. Shi, K. Zhang, E. J. Jensen, A. Gettelman, D. Barahona, A. Nenes, and P. Lawson, 2012b: Sensitivity studies of dust ice nuclei effect on cirrus clouds with the Community Atmosphere Model CAM5. Atmos. *Chem. Phys.,* **12,** 12 061–12 079.

Liu, Y., J. R. Sun, and B. Yang, 2009: The effects of black carbon and sulphate aerosols in China regions on East Asia monsoons. *Tellus,* **61B,** 642–656.

Lorenz, E. N., 1955: Available potential energy and the maintenance of the general circulation, *Tellus,* **7(2),** 157-167.

Lu, Y., and Y. Deng, 2015: Initial transient response of an intensifying baroclinic wave to increases in cloud droplet number concentration. *J. Climate,* **28,** 9669–9677.

——, and ——, 2016: Impact of environmental aerosols on a developing extratropical cyclone in the Superparameterized Community Atmosphere Model. *J. Climate,* **29,** 5533–5546.

MacVean, M. K., 1985: Long-wave growth by baroclinic processes. *J. Atmos. Sci.,* **42,** 1089–1101.

Mahlman, J. D., 1979: Structure and interpretation of blocking anticyclones as simulated in a GFDL general circulation model. Proc. 13th Stanstead Seminar, Dept. of Meteorology, McGill University, 70-76.

Mak, M., 1982: On moist quasi-geostrophic baroclinic instability. *J. Atmos. Sci.,* **39,** 2028–2037.

——, and M. Cai, 1989: Local barotropic instability. *J. Atmos. Sci.,* **46(21),** 3289-3311.

——, 1998: Influence of surface sensible heat flux on incipient marine cyclogenesis. *J. Atmos. Sci.,* **55,** 820–834.

Manabe, S., J. Smagorinsky, and R. Strickler, 1965: Simulated climatology of a general circulation model with a hydrologic cycle. *Mon. Wea. Rev.,* **93,** 769–798.

Martin, G. M., D. Johnson, and A. Spice, 1994: The measurement and parameterization of effective radius of droplets in warm stratocumulus clouds. *J. Atmos. Sci.,* **51,** 1823–1842.

Metz, W., 1986: Transient cyclone-scale vorticity forcing of blocking highs. *J. Atmos. Sci.,* **43,** 1467–1483.

——, 1989: Low frequency anomalies of atmospheric flow and the effects of cyclone-scale eddies: A canonical correlation analysis. *J. Atmos. Sci.,* **46,** 1027–1041.

Mlawer, E. J., S. J. Taubman, P. D. Brown, M. J. Iacono, and S. A. Clough, 1997: Radiative transfer for inhomogeneous atmospheres: RRTM, a validated correlated-k model for the longwave. *J. Geophys. Res.,* **102,** 16 663–16 682.

Morrison, H., J. A. Curry, and V. I. Khvorostyanov, 2005: A new double-moment microphysics parameterization for application in cloud and climate models. Part I: Description. *J. Atmos. Sci.,* **62,** 1665–1677.

Mullen, S. L., 1986: The local balances of vorticity and heat for blocking anticyclones in a spectral general circulation model. *J. Atmos. Sci.,* **43,** 1406–1419.

——, 1987: Transient eddy forcing of blocking flows. *J. Atmos. Sci.,* **44,** 3–22.

Murray, B. J., D. O'Sullivan, J. D. Atkinson, and M. E. Webb, 2012: Ice nucleation by particles immersed in supercooled cloud droplets. *Chem. Soc. Rev.,* **41,** 6519–6554.

Nabat, P., S. Somot, M. Mallet, F. Sevault, M. Chiacchio, and M. Wild, 2015: Direct and semi-direct aerosol radiative effect on the Mediterranean climate variability using a coupled regional climate system model. *Climate Dyn.,* **44,** 1127–1155.

Nakamura, H., 1992: Midwinter suppression of baroclinic wave activity in the Pacific. *J. Atmos. Sci.,* **49,** 1629–1642.

——, and T. Izumi, 1999: Out-of-phase relationship between the interannual fluctuations in poleward heat transport by the east Asian winter monsoon and Pacific stormtrack. Preprints, 12th Conf. on Atmospheric and Oceanic Fluid Dynamics, New York, NY, *Amer. Meteor. Soc.,* 139–142.

——, and T. Sampe, 2002: Trapping of synoptic-scale disturbances into the North-Pacific subtropical jet core in midwinter. *Geophys. Res. Lett.,* **29(16),** 8-1-8-4.

Namias, J., and P. F. Clapp, 1944: Studies of the motion and development of long waves in the westerlies. *J. Meteor.,* **1,** 57–77.

Orlanski, I., and J. Katzfey, 1991: The life cycle of a cyclone wave in the Southern Hemisphere. Part I: Eddy energy budget. *J. Atmos. Sci.,* **48,** 1972–1998.

——, and E. K. M. Chang, 1993: Ageostrophic geopotential fluxes in downstream and upstream development of baroclinic waves. *J. Atmos. Sci.,* **50,** 212–225.

Peixoto, J. P., and A. H. Oort, 1992: *Physics of Climate.* American Institute of Physics, 520 pp.

Penny, S., G. H. Roe, and D. S. Battisti, 2010: The source of the midwinter suppression in storminess over the North Pacific, *J. Climate,* **23(3),** 634-648.

——, ——, and ——, 2011: Reply. *Journal of Climate,* **24(19),** 5192-5194.

Petterssen, S., 1956: *Weather analysis and forecasting,* 2nd ed., McGraw-Hill, 505 pp.

Phillips, V. T. J., T. W. Choularton, A. M. Blyth, and J. Latham, 2002: The influence of aerosol concentrations on the glaciation and precipitation of a cumulus cloud. *Q. J. R. Meteorol. Soc.,* **128(581),** 951–971.

Plougonven, R., and C. Snyder, 2007: Inertia–gravity waves spontaneously generated by jets and fronts. Part I: Different baroclinic life cycles. *J. Atmos. Sci.,* **64,** 2502–2520.

Plumb, R. A., 1983: A new look at the energy cycle. *J. Atmos. Sci.,* **40(7),** 1669-1688.

Pruppacher, H. R. and J. D. Klett, 1997: *Microphysics of clouds and precipitation.* Atmos. and Ocean. Sci. Lib., Kluwer Academic Publishers, Dordrecht, The Netherlands.

Quaas, J., and Coauthors, 2009: Aerosol indirect effects—General circulation model intercomparison and evaluation with satellite data. *Atmos. Chem. Phys.,* **9,** 8697–8717.

Ramanathan, V., P. Crutzen, J. Kiehl, and D. Rosenfeld, 2001: Aerosols, climate and the hydrological cycle. *Science,* **294,** 2119–2124.

Reed, R. J., M. T. Stoelinga, and Y.-W. Kuo, 1992: A model aided study of the origin and evolution of the anomalously high PV in the inner region of a rapidly deepening marine cyclone. *Mon. Wea. Rev.,* **120,** 893–913.

Rex, D. F., 1950a: Blocking action in the middle troposphere and its effect upon regional climate I: An aerological study of blocking action. *Tellus,* **2,** 196-211.

——, 1950b: Blocking action in the middle troposphere and its effect upon regional climate II: The climatology of blocking action. *Tellus,* **2,** 275-301.

Robinson, W. A., 1991: The dynamics of low-frequency variability in a simple model of the global atmosphere. *J. Atmos. Sci.,* **48,** 429 – 441.

Robinson, D. P., R. X. Black, and B. A. McDaniel, 2006: A Siberian precursor to midwinter intraseasonal variability in the North Pacific storm track. *Geophys. Res. Lett.,* **33(15),** L15811.

Rosenfeld, D., 1999: TRMM observed first direct evidence of smoke from forest fires inhibiting rainfall. *Geophys. Res. Lett.,* **26,** 3105–3108.

——, U. Lohmann, G. B. Raga, C. D. O'Dowd, M. Kulmala, S. Fuzzi, A. Reissell, and M. O. Andreae, 2008: Flood or drought: How do aerosols affect precipitation? *Science,* **321,** 1309–1313.

Saltsman, B., 1957: Equations governing the energetics of the larger scales of atmospheric turbulence in the domain of wave number, *J. Meteor.,* **14(6),** 513-523.

Schneider, T., K. L. Smith, P. A. O'Gorman, and C. C. Walker, 2006: A climatology of tropospheric zonal-mean water vapor fields and fluxes in isentropic coordinates. *J. Climate,* **19,** 5918– 5933.

Sheng, J., and Y. Hayashi, 1990a: Observed and simulated energy cycles in the frequency domain, *J. Atmos. Sci.,* **47(10),** 1243-1254.

——, and ——, 1990b: Estimation of atmospheric energetics in the frequency domain during the FGGE Year, *J. Atmos. Sci.,* **47(10),** 1255-1268.

——, and J. Derome, 1991: An observational study of the energy transfer between the seasonal mean flow and transient eddies. *Tellus A,* **43(2),** 128-144.

Shutts, G. J., 1983: The propagation of eddies in diffluent jet streams: Eddy vorticity forcing of blocking flow fields. *Quart. J. Roy. Meteor. Soc.,* **109,** 737–761.

Simmons, A. J., and B. J. Hoskins, 1979: The downstream and upstream development of unstable baroclinic waves. *J. Atmos. Sci.,* **36,** 1239–1254.

Smith, P. J., 1969: On the contribution of a limited region to the global energy budget. *Tellus,* **21,** 202–207.

Squires, P., and S. Twomey, 1966: A comparison of cloud nucleus measurements over central North America and Caribbean Sea. *J. Atmos. Sci.,* **23,** 401–404.

Stephens, G.L., Webster, P.J., 1981: Clouds and climate—sensitivity of simple systems. *J. Atmos. Sci.,* **38(2),** 235–247.

Stevens, B., and G. Feingold, 2009: Untangling aerosol effects on clouds and precipitation in a buffered system. *Nature,* **461,** 607–613.

Straus, D. M., and J. Shukla, 1997: Variations of midlatitude transient dynamics associated with ENSO. *J. Atmos. Sci.,* **54,** 777–790.

Swanson, K. L., and R. T. Pierrehumbert, 1997: Lower-tropospheric heat transport in the Pacific storm track. *J. Atmos. Sci.,* **54,** 1533–1543.

Tao, W.-K., J.-P. Chen, Z. Li, C. Wang, and C. Zhang, 2012: Impact of aerosols on convective clouds and precipitation. *Rev. Geophys.,* **50,** RG2001.

Teller, A., and Z. Levin, 2006: The effects of aerosols on precipitation and dimensions of subtropical clouds: A sensitivity study using a numerical cloud model, *Atmos. Chem. Phys.,* **6,** 67–80.

Thompson, D. J., and J. M. Wallace, 1998: The Arctic Oscillation signature in the wintertime geopotential height and temperature fields. *Geophys. Res. Lett.,* **25,** 1297–1300.

——, and ——, 2000: Annular modes in the extratropical circulation. Part I: Month-to-month variability. *J. Climate,* **13,** 1000–1016.

——, ——, and G. C. Hegerl, 2000: Annular modes in the extra-tropical circulation. Part II: Trends. *J. Climate,* **13,** 1018–1036.

Thompson, G., and T. Eidhammer, 2014: A study of aerosol impacts on clouds and precipitation development in a large winter cyclone. *J. Atmos. Sci.,* **71,** 3636–3658.

Tibaldi, S., and F. Molteni, 1990: On the operational predictability of blocking. *Tellus,* **42A,** 343-365.

Trenberth, K. E., 1986: An assessment of the impact of transient eddies on the zonal flow during a blocking episode using localized Eliassen-Palm flux diagnostics, *J. Atmos. Sci.,* **43(19),** 2070-2087.

——, and J. W. Hurrell, 1994: Decadal atmosphere–ocean variations in the Pacific. *Climate Dyn.,* **9,** 303–319.

——, and D. P. Stepaniak, 2003: Covariability of components of poleward atmospheric energy transports on seasonal and interannual timescales. *J. Climate,* **16,** 3691–3705.

——, Fasullo, J.T., Kiehl, J., 2009: Earth's global energy budget. *Bull. Am. Meteorol. Soc.,* **90(3),** 311–323.

Twomey, S., 1977: Influence of pollution on shortwave albedo of clouds. *J. Atmos. Sci.,* **34,** 1149–1152.

van den Heever, S. C., G. G. Carrio, W. R. Cotton, P. J. DeMott, and A. J. Prenni, 2006: Impacts of nucleating aerosol on Florida storms. Part I: Mesoscale simulations. *J. Atmos. Sci.,* **63,** 1752–1775.

van Vuuren, D.P., J. Edmonds, M. Kainuma, et al., 2011: The representative concentration pathways: an overview. *Climatic Change,* **109,** 5–31.

Vautard, R., and B. Legras, 1988: On the source of mid-latitude low-frequency variability. Part II: Nonlinear equilibration of weather regimes. *J. Atmos. Sci.,* **45,** 2845–2867.

——, ——, and M. Deque, 1988: On the source of mid-latitude low-frequency variability. Part I: A statistical approach to persistence. *J. Atmos. Sci.,* **45,** 2811–2843.

Wallace, J. M., and D. S. Gutzler, 1981: Teleconnections in the geopotential height field during the Northern Hemisphere winter. *Mon. Wea. Rev.,* **109,** 785–812.

Wang, C., 2005: A model study of the response of tropical deep convection to the increase of CCN concentration: I. Dynamics and microphysics. *J. Geophys. Res.,* **110,** D21211.

Wang, M., and Coauthors, 2011a: The multi-scale aerosol-climate model PNNL-MMF: Model description and evaluation. *Geosci. Model Dev.,* **4,** 137–168.

——, S. Ghan, M. Ovchinnikov, X. Liu, R. Easter, E. Kassianov, Y. Qian, and H. Morrison, 2011b: Aerosol indirect effects in a multi-scale aerosol-climate model PNNL-MMF. *Atmos. Chem. Phys.,* **11,** 5431–5455.

——, and Coauthors, 2014: Assessing the effects of anthropogenic aerosols on Pacific storm track using a multiscale global climate model. *Proc. Natl. Acad. Sci. USA,* **111,** 6894–6899.

Warner, J., and S. Twomey, 1967: The production of cloud nuclei by cane fires and the effects on cloud droplet concentration. *J. Atmos. Sci.,* **24,** 704–706.

——, 1968: A reduction in rainfall associated with smoke from sugar-cane fires: An inadvertent weather modification? *J. Appl. Meteorol.,* **7,** 247–251.

Whitaker, J. S., and R. M. Dole, 1995: Organization of storm tracks in zonally varying flows. *J. Atmos. Sci.,* **52,** 1178–1191.

——, and P. D. Sardeshmukh, 1998: A linear theory of synoptic eddy statistics. *J. Atmos. Sci.,* **55,** 237–258.

Wood, R., 2012: Stratocumulus clouds. *Mon. Weather Rev.,* **140(8),** 2373–2423.

Yang, G.-Y., and B. J. Hoskins, 1996: Propagation of rossby waves of nonzero frequency. *J. Atmos. Sci.,* **53(16),** 2365-2378.

Yang, Y., J. Fan, R. L. Leung, C. Zhao, Z. Li, and D. Rosenfeld, 2016: Mechanisms contributing to suppressed precipitation in Mt. Hua of central China. Part I: Mountain valley circulation. *J. Atmos. Sci.,* **73,** 1351–1366.

Yang, X., M. Ferrat, and Z. Li, 2013a: New evidence of orographic precipitation suppression by aerosols in central China. *Meteor. Atmos. Phys.,* **119,** 17–29.

——, Z. Yao, Z. Li, and T. Fan, 2013b: Heavy air pollution suppresses summer thunderstorms in central China. *J. Atmos. Sol.-Terr. Phys.,* 95–96, 28–40.

Yeh, T.-C., 1949: On energy dispersion in the atmosphere. *J. Meteor.,* **6,** 1–16.

Zhang, D. M., Z. Wang, A. Heymsfield, J. Fan, D. Liu, and M. Zhao, 2012: Quantifying the impact of dust on heterogeneous ice generation in midlevel supercooled stratiform clouds. *Geophys. Res. Lett.,* **39,** L18805.

Zhang, H., G. M. McFarquhar, S. M. Saleeby, and W. R. Cotton, 2007: Impacts of Saharan dust as CCN on the evolution of an idealized tropical cyclone. *Geophys. Res. Lett.,* **34,** L14812.

——, G. M. McFarquhar, W. R. Cotton, and Y. Deng, 2009: Direct and indirect impacts of Saharan dust acting as cloud condensation nuclei on tropical cyclone eyewall development. *Geophys. Res. Lett.,* **36,** L06802.

Zhang, R., G. Li, J. Fan, D. L. Wu, and M. J. Molina, 2007: Intensification of Pacific storm track linked to Asian pollution. *Proc. Natl. Acad. Sci. USA,* **104,** 5295–5299.

Zhang, Yon., Sun, S., Olsen, S. C., Dubey, M. K. and He, J., 2011: CCSM3 simulated regional effects of anthropogenic aerosols for two contrasting scenarios: rising Asian emissions and global reduction of aerosols. *Int. J. Climatol.,* **31,** 95–114.

Zhang, Yua., J. M. Wallace, and D. S. Battisti, 1997: ENSO-like interdecadal variability: 1900–93. *J. Climate,* **10,** 1004–1020.

Zhang, Yun., and I. M. Held, 1999: A linear stochastic model of a GCM's midlatitude storm tracks. *J. Atmos. Sci.,* **56,** 3416–3435.

Zhou, R., and Y. Deng, 2013: A model analysis of the interactions between East Asian anthropogenic aerosols and North Pacific atmospheric transients in boreal winter. *J. Geophys. Res. Atmos.,* **118,** 306–316.